AHEAD Work package 9 : JRA4 – Assessment of gamma-ray experiments draft for a final report - 31 Oct 2018

Objectives

The European Gamma-Ray community has a long and successful record in designing, realizing and observing with space observatories. Will there be a follow-up mission for the space observatories INTEGRAL, AGILE and FERMI, and what objectives and performances will it have ? At present, a large number of laboratories prepare the future through ambitious R&D programs on the key technologies required for the next step in space. Given the limited number of flight opportunities, and the fierce competition to get selected by a space agency, it is important to present mature proposals in response to the rare calls of opportunity.

Work method

A Science Advisory Group (SAG) of WP9 has been working during the initial phase of AHEAD, producing a white paper of prioritized science objectives for gamma-ray astronomy. The group has attempted to identify the most relevant, fundamental astrophysical problems only gamma-ray astronomy would be able solve. The white paper has been presented at the common SAG/IWG meeting in 2016 (milestone 1 / deliverable 1 of WP9) and served as input for the "Instrument Working Group" (IWG). The two top-priorities that the SAG has identified through a series of skype meetings and a physical meeting (being *Gamma-Ray Bursts* and *Nuclear Science* (including Stellar Explosions, Low Energy Cosmic-Rays, Positrons).

The next step towards the design of mission concepts for medium energy gamma-rays was to translate the white books science priorities into a set of "mission requirements" - these were delivered by the IWG in June 2016 (milestone 2 / deliverable 2 of WP9).

Following a call for instrument concepts issued by the IWG, five proposal were received. The call was open to the high-energy astrophysics community at large (AHEAD, ASTROMEV, ASTROGAM mailing lists), however four of the five proposals came from WP9 institutes. The proposals were evaluated by the Instrument Working Group, and while none of the proposals alone satisfied all the requirements, it was realized that each of the five proposals covered a more or less broad subset of the requirements. Starting in late fall 2016, three teams started working towards the proposed instrument concepts within the Simulation Working Group (SWG). The selection of the teams to work within the SWG were milestone 3 / deliverable 3 of WP9.

The work of the groups is not terminated at this point (Oct 2018). The present document is a first draft for the final report (deliverable 4 of WP9) summarizing the work provided by the teams of the Simulation Working Group towards new mission concepts for gamma-ray astronomy. The work for the final report and publication in the Journal "Experimental Astronomy" will continue until mid-February 2019, when an international conference (milestone 4) will conclude and valorize the activities of AHEAD/WP9 : the 12th INTEGRAL conference and first AHEAD workshop has the theme "INTEGRAL looks AHEAD to Multimessenger astronomy" and will take place in Geneva (Switzerland) from 11 to 15 February 2019 (see https://www.astro.unige.ch/integral2019).

Principal steps

The principal steps/exchanges and the sub-groups involved for the reporting period are listed in the table below (physical meetings are in bold letters).

14 Sept. 2015	**AHEAD kick-off meeting, IAPS Rome**
8 Oct. 2015	**SAG lunch, Rome (INTEGRAL meeting)**
26 Oct. 2015	SAG skype, Kick-off : plan activities and adopt work method
2 Dec. 2015	**SAG meeting at IAP Paris : presentation of science topics I**
22 Dec. 2015	SAG skype: presentation of science topics II / SAG survey
22 Jan. 2016	SAG skype: interpretation of the results of SAG survey
5 Feb. 2016	SAG skype: conclude on priorities, prepare white paper
26 Feb. 2016	SAG skype: iterating on the white paper
15/16 March 2016	**SAG/IWG "handshake" meeting Toulouse : present white paper**
19 May 2016	IWG skype: iterate on mission requirements
1 June 2016	IWG meeting in Rome, prepare call for mission concepts
15 June 2016	Call for mission concepts issued
20 July 2016	Deadline (extended) for the reception of mission concepts
22 July 2016	IWG skype : evaluation / selection of mission concepts
12 Sept. 2016	SWG skype : kick-off / organisation of work
22 Sept. 2016	SWG skype : job announcements for the post-doc to be hired
12 Jan. 2017	SWG skype : presentation of the selected post-docs
25 April 2017	**SWG meeting Barcelona**
26-28 April 2017	**SWG "MEGALIB SCHOOL" IEEC Barcelona**
14/15 Nov 2017	**1st SWG progress meeting, U. Tor Vergata, Rome**
18/19 April 2018	**2nd SWG progress meeting, U. Coimbra**
5 June 2018	SWG skype : outcome of the ESA M5 mission selection
18/19 Oct 2018	**3rd SWG progress meeting, IAP Paris**
11-15 Feb. 2019	**12th INTEGRAL conference and first AHEAD workshop "INTEGRAL looks AHEAD to Multimessenger astronomy", Geneva**

Sub-groups AHEAD/WP9

Science Advisory Group (SAG)
Lorenzo Amati, INAF Bologna; Lorraine Hanlon, UC Dublin; Jordi Isern, CSIC-IEEC Barcelona
Aldo Morselli, INFN Rome; Uwe Oberlack, Uni Mainz; Nicolas Prantzos, IAP Paris
Constancia Providencia, ILL Coimbra; Piero Rosati, INFN Ferrara; Regis Terrier, APC Paris; Peter von Ballmoos, IRAP Toulouse

Instrument Working Group (IWG) of WP9
Ezio Caroli, INAF/IASF-Bologna; Filippo Frontera, INFN Ferrara; Gerry Skinner; Margarida Hernanz, CSIC-IEEC Barcelona; Gottfried Kanbach, MPE Garching; Vincent Tatischeff, CSNSM Orsay; Peter von Ballmoos, IRAP Toulouse

Simulation Working Group (SWG)
Laboratories involved in the modeling the selected instrument concepts include:
IRAP Toulouse, CSNSM Orsay, APC Paris, CEA Saclay, UCD Dublin, CSIC-IEEC Barcelona, INFN Roma Tor Vergata, LIP Coimbra, University of Ferrara

Milestones and deliverables

The accomplished milestones and associated deliverables are listed below:
(*achieved/delivered*, *to be achieved/delivered*)

	WP9 tasks, subgroup in charge	M milestones, date , D deliverables
1	Prioritize gamma-ray science objectives	M1 - SAG/IWG handshake meeting, 16.3.2016
	Science Advisory Group	D1 - Science White Paper
2	Define mission requirements	M2 - Mission requirement
	Instrument Working Group	D2 - Mission requirement doc., 1.6.2016
3	Design of instrument concepts	
	Instrument Working Group	
4	Select instrument concepts	M3 : Instrument concept selection, 22.7.2016
	Instrument Working Group	D3 : Instrument concept selection document
5	Simulate selected instrument concepts	April 2017 (for some Dec16) – Feb 2019 presently still ongoing !
	Simulation Working Group	
6	Discuss and valorize results	M4 conference, Feb 2019
		D4 final report, EXPA papers

Summary of the activities of WP9

Task 1: Prioritization of gamma-ray science objectives

During the initial phases of AHEAD/WP9, a Science Advisory Group (SAG) considered the prime scientific questions that might be addressed by a future space mission operating in the energy domain 100 keV – 100 MeV. The group has attempted to identify the most relevant, fundamental astrophysical problems only gamma-ray astronomy would be able solve.
The two top-priorities that the SAG has identified through a series of skype meetings and a physical meeting (being *Gamma-Ray Bursts* and *Nuclear Science* (including Stellar Explosions, Low Energy Cosmic-Rays, Positrons).

Top-priority : Gamma-Ray Bursts

Since their serendipitous discovery more than four decades ago, most gamma-ray bursts (GRBs) have been shown to originate at cosmological distances, in the catastrophic death of massive stars. The collapse of a massive star into a black hole releases a huge amount of gravitational energy and surrounding material is accelerated to near the speed of light in a narrow jet, producing the luminous flash of gamma-rays that allows us to see these cosmic lighthouses across much of the observable universe. The nearest GRBs from such 'collapsars' are excellent electromagnetic counterpart candidates to gravitational wave (GW) events. In addition, coalescing binaries, thought to be the progenitors of the 'short' subset of GRBs, are widely viewed as the most promising sources of gravitational waves. The detection and localization of these events is therefore a priority in the new era of gravitational wave astronomy and in the future era of space-based GW measurements.

More in general, because of their huge luminosities (up to > 10^{53} erg radiated in few tens of seconds) emitted by the most relativistic jets known (Lorentz factor $\Gamma > 100$) and their redshift distribution extending up to at least z ~9, GRBs offer enormous potential as powerful probes of the early Universe (evolution of stars, galaxies and the inter-galactic medium up to the epoch of re-ionization, population III stars), as test-beds for fundamental physics (e.g., constraining limits on violations of Lorentz invariance), and as laboratories for matter and radiation under extreme conditions.

Sensitive measurements by next generation gamma-ray experiments, especially if complemented by lower-energy instrumentation, will allow a substantial step forward in these GRB-related research areas, which are of extreme interest for several fields of astrophysics, cosmology and fundamental physics, and will provide an ideal synergy with the large multi-wavelength and multi-messenger facilities that will be operative in the next decade (e.g., eLISA, E-ELT, SKA, CTA, ATHENA, neutrino observatories).

Top-priority : *Nuclear Sciences* (Stellar Explosions, Low Energy Cosmic-Rays, Positrons)

Gamma-ray line emission in the MeV domain is obtained through the decay/de-excitation of radioactive/stable nuclei, which have been produced/excited by high-energy astrophysical phenomena, like supernova explosions or cosmic rays. They provide unique information on the isotopic identity of the emitters, on the underlying physical processes (e.g. nucleosynthesis, spallation etc.) and on the physical conditions of the - otherwise inaccessible – emitting region. Progress in the field has been slow, being hampered by poor angular resolution (by astronomy standards) and sensitivity limitations, due to large instrumental backgrounds. Despite these drawbacks, the field offers great potential for the study of various high-energy astrophysical processes, concerning a large fraction of the astrophysical community. Three topics of high priority have been identified: the physics of thermonuclear supernovae, the puzzling origin of Galactic positrons and the yet unexplored field of low energy cosmic rays.

Legacy Science topics include

-       Pulsars physics (high B fields, testing Lorentz invariance …)
-       Extragalactic compact objects: jets, the disk/jet transition, testing Lorentz invariance
-       Galactic compact obj / binaries : jets, the disk/jet transition, testing Lorentz invariance
-       Nuclear lines from compact objects (neutron capture)
-       Dark Matter signatures
-       Galactic Centre Physics (central black hole, interaction with surrounding medium)
-       High-z AGNs
-       Origin of the "Fermi Bubbles"
-       MeV extragalactic background / Baryon asymmetry at cosmological distances
-       Solar flare physics
-       Terrestrial Gamma-Ray Flashes

Task 2: Definition of mission requirements

Based on the conclusions of the science white paper (see task 1, above), the Instrument Working Group (IWG) continued the work of WP9 by defining mission requirements for a future mission. The bottom line of this work, which lasted from March 2016 (the SAG/IWG handshake meeting) until June 2016 (task 3, see below) is summarized in the two tables below.

	E [MeV]	dE @ [MeV]	FOV [sr]	Angular Resolution	Timing [microsec]	Sensitivity	Realtime alert	polarimetry
GRB need	0.05-3000	<10% at 0.3 MeV	> 2-3 sr (~250 GRBs/yr)	Localization accuracy < 40' (120 GRBs/yr) to < 5' (~20 brightest GRBs/yr)*	< 10	0.05 ph cm^{-2} s^{-1} (peak, 0.2 – 2 MeV, 1s)	yes	MDP ~ 5-10 % (in ~100 GRBs)
GRB extended **GRB afterglow** Good to have	0.05 – 2 0.05 - 1	<10% at 0.3 MeV <10% at 0.3 MeV	> 2-3 sr <5 arcmin	Localization accuracy < 40' to < 5' Angular resolution <1'	< 10 -	5x10^{-4} ph cm^{-2} s^{-1} (1000s from onset, 1000 s duration, 0.2-2MeV) (Assumptions: brightest 15% GRBs, 12 hrs after events, 10 ks duration, ph cm^{-2} s^{-1}keV^{-1}) 1.8x10^{-7} (0.1-0.3 MeV)	Yes Yes	MDP ~ 5-10 % (in ~100 GRBs) MDP ~ 5-10 % (in ~100 GRBs)

Table 2 : instrument requirements for Gamma-Ray Bursts

	E [MeV]	dE @ [MeV]	FOV [sr]	Angular Resolution	Timing [µsec]	Sensitivity	Realtime alert
NS SN1a need	0.1 - 2	3%-5%	N/A	N/A	-	3.10^{-7} ph cm^{-2} s^{-1} keV^{-1} (1Ms/ 847 keV, 3 σ cont. sensitivity, line width 35 keV)	N/A
NS SN1a good to have	0.05 - 2	0.3%			-	10^{-7} ph cm^{-2} s^{-1} keV^{-1} (1 Ms / 847 keV) 3 σ cont sensitivity, line width 35 keV) 10^{-7} ph cm^{-2} s^{-1} keV^{-1} (1 Ms / 158 keV, 3 σ cont sensitivity, line width 20 keV)	158 keV line from ^{56}Ni should be observed around the maximum
NS e$^+$ need	0.3 – 0.8	5%		< 1°		5.10^{-6} ph cm^{-2} s^{-1} point source everywhere (all-sky mapping)	
NS e+ good to have	0.1 - 2	0.2%		< 5 '(in GC) diffuse emission at Gal. anti-center		10^{-6} ph cm^{-2} s^{-1} point source 1.6x10^{-4} ph cm^{-2} s^{-1} sr^{-1}	
NS LECR need	0.1 - 10	2% at 5 MeV	>1 sr	1°	-	10^{-4} ph cm^{-2} s^{-1} sr^{-1} @ 3-8 MeV (inner Galaxy)	-
NS LECR good to have	0.1 - 10	1% at 5 MeV		< 1°	-	5 10^{-7} ph cm^{-2} s^{-1} in ~10^{-2} sr @ 3–8 MeV band (Orion A)	-

Table 3 : instrument requirements for Nuclear Sciences

Task 3: Design of instrument concepts

In order to draw on the widest possible expertise and to make sure that all possible developments and innovations are considered in the follow-up studies of instrumentation, a call for instrument concepts, open to the high-energy astrophysics community at large (AHEAD, ASTROMEV, ASTROGAM mailing lists), was issued by the IWG. The public announcement was made on June 15, 2016; proposals were due by July 14, 2016.

Five proposal were received (table 3) – and although the call was open to the entire high-energy astrophysics community, four of the five proposals came from WP9 institutes.

Proposal name	proposers	labs	Instrument concept
ASCI	von Ballmoos et al.	IRAP, UCD UCB	All-Sky Compton Imager – study of a "homogeneous" array of cross-strip Ge detectors using COSI balloon data.
ASTENA	Rosati et al.	UNIFE, DTU Space, INAF Bologna & Brera U. Coimbra	Advanced Surveyor of Transient Events and Nuclear Astrophysics - composed of a wide field monitor/spectrometer and a narrow field telescope
Baseline e-ASTROGAM	Morselli et al.	INFN Roma Tor Vergata	Optimization the baseline design of the e-Astrogam concept
HE gamma-ray polarization	Cattaneo	INFN-Pavia	Measuring gamma-ray polarization in the ~100 MeV range with Si detectors
PACT	Tatischeff et al.	CSNSM, IAPS GSFC, INFN Padova, INAF Bologna APC, ICE, CLPU	Pair And Compton Telescope – consisting of a silicon tracker for Compton scattering / pair conversion and a position-sensitive Calorimeter

Table 3 : proposals received following the call for instrument concepts by the IWG

Task 4: Selection of instrument concepts to be assessed

The five proposals (see above, task 3) have been evaluated by the Instrument Working Group and a discussion took place via skype on July 22, 2016. While none of the proposals alone satisfied all the requirements formulated in the AO, it was realized that each of the five proposals covers a more or less broad subset of the requirements. Having complementary strengths, the proposed concepts would cover essentially all the requirements together.
The IWG recognized that all of the five proposals can be realized when appropriately grouped in three teams. As the PACT and e-ASTROGAM proposals effectively concerns identical instrument concepts (proposed in M4 and M5. The following scheme was discussed and accepted :

> team 1 : Si-based Compton Telescopes (PACT / e-ASTROGAM / HE $\gamma-$ray polarization)
> team 2 : Ge-Based Compton Telescopes (ASCI)
> team 3 : Laue Lens & wide field monitor and spectrometer (ASTENA)

Task 5 : Simulation of the selected instrument concepts

team 1 : Si-based Compton Telescopes (PACT / e-ASTROGAM / HE $\gamma-$ray polarization)

 CSNSM (Orsay, France): V. Tatischeff, C. Hamadache, J. Kiener
 INAF-IAPS (Roma, Italy): M. Tavani, A. Argan, I. Donnarumma
 NASA/GSFC (Greenbelt MD, USA): J. McEnery, E. Hays, A.A. Moiseev, J.S. Perkins, J.
 Racusin, D.J. Thompson
 INFN (Padova, Italy): A. De Angelis
 INAF-IASF (Bologna, Italy): A. Bulgarelli, V. Fioretti
 APC (Paris, France): P. Laurent, R. Terrier
 ICE/CSIC-IEEC (Barcelona, Spain): M. Hernanz, J. Isern
 IFAE (Barcelona, Spain): M.
 Martinez CLPU (Salamanca, Spain):
 J. M. Alvarez INFN (Roma Tor
 Vergata) : A. Morselli
 University of Coimbra, Portugal: Rui Curado da Silva

End of project report

Chapter 1

Reconstruction

The Kalman filter is an iterative method which uses a combination of prediction, filtering and smoothing to reconstruct the original direction of the incoming particle. The technique was firstly proposed by Frühwirth [1]
The impinging gamma ray, interacting with the material in the tracker, creates an electron-positron pair. The Kalman filter algorithm reconstructs the track of the two created particles and then infers the direction of the original photon. The multiple scattering as well as the distance of the planes and the uncertainty of the measurements, are taken in consideration in order to have a better reconstruction. The core of the distribution of the multiple scattering is approximately Gaussian with a projected width of [2]

$$\theta_{MS} = \frac{13.6\text{MeV}}{E/\text{MeV}} \sqrt{z/X_0}[1 + 0.038\ln(z/X_0)] \tag{1.1}$$

where E is the energy of the particle (in MeV) and z is the thickness of the crossed material (in radiation length).
The important parameters for the measurement error are: the strip pitch, the readout method and the noise in the strips. The readout model greatly affects the error associated to the measure.
If the readout is analog the accuracy can be substantially improved if the signal charge is collected on more than one strip (due to charge diffusion) and the coordinate is determined by means of an interpolation method (e.g. center of gravity of the signal). The error depends on the noise in the strips through the equation [3]

$$\sigma = \frac{a_{cf} \cdot ENC \cdot p_a}{Q_s} \tag{1.2}$$

where a_{cf} is the so-called centroid finding constant, ENC is the Equivalent Noise Charge (amount of input charge that makes the signal-to-noise ratio equal to one), p_a is the amplifier pitch and Q_s is the signal charge. With a strip pitch of 120 μm,

2

readout pitch of 240 μm, the error on the measure can be as little as 40 μm. The analog readout is presently used on the AGILE mission.

In the case of a digital readout, such as the one used in the tracker of Fermi-LAT, no information are collected on the energy released in the Si and the error is always equal to $pitch/\sqrt{12}$ [3]. For Fermi-LAT the error on each measure is 228 μm/$\sqrt{12} \simeq 66$ μm.

At low energy the main contribution to the error in the reconstruction is related to the multiple scattering. As visible by eq. 1.1 the multiple scattering angle is large at low energy and the error is proportional to the radiation length of the material crossed. At high energies the multiple scattering becomes negligible and the measurement error starts to be dominant.

e-ASTROGAM will not present a magnet and consequently the tracker will not provide a momentum measurement. The equations used by the Kalman filter are therefore simplified.

In the following, the Kalman filter as implemented in detectors with single-sided Silicon layers (e.g. AGILE and Fermi) and a new proposed version of the Kalman filter for a double-sided Silicon detector (i.e. e-ASTROGAM) will be presented.

1.1   Kalman2D: Single-sided Silicon

Having a single-sided Silicon tracker, the two projections, in x and y, are fitted separately. The formalism described in the following and in sec. 1.1.1 and 1.1.2, is based on the work by Frühwirth [1].

Information on the track at each layer are stored in a state vector. In this case the state vector for the i-th plane, $\boldsymbol{x}_i$ has two components: the position of the hit and the tangent of the angle of the track to the next layer. For each layer this system of equation is set:

$$\boldsymbol{x}_i = \boldsymbol{F}_{i-1}\boldsymbol{x}_{i-i} + \boldsymbol{w}_{i-1} \tag{1.3}$$

where $\boldsymbol{F}_{i-1}$ is the propagator from the plane i-1 to the plane i and $\boldsymbol{w}_{i-1}$ is a variable related to the multiple scattering. The propagator combines directional and position information to compute the position on the next level. Without a magnetic field it takes the form:

$$\boldsymbol{F}_{i-1} = \begin{pmatrix} 1 & d_{i-1,i} \\ 0 & 1 \end{pmatrix} \tag{1.4}$$

where $d_{i-1,i}$ is the distance between the plane i and the plane i-1.

The measures performed on the i-th plane can be written as:

$$\boldsymbol{m}_i = \boldsymbol{H}_i\boldsymbol{x}_i + \delta_i \tag{1.5}$$

3
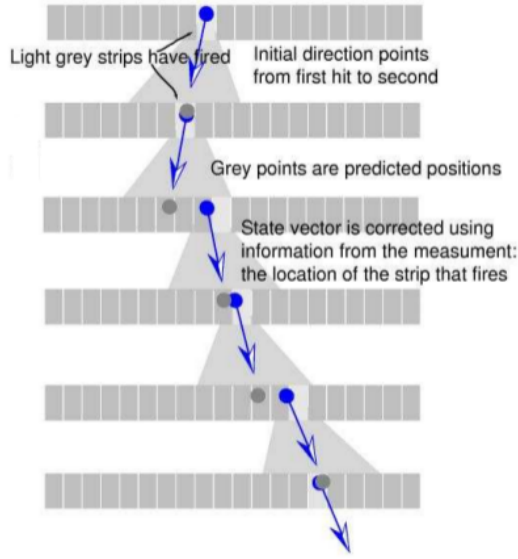
Figure 1.1: Filtering process of the Kalman filter [4].

where $\boldsymbol{H}_i$ is the measurement matrix, in this case $\boldsymbol{H} = \begin{pmatrix} 1 & 0 \end{pmatrix}$ and δ_i is the measurement error.

The two uncertainties, multiple scattering and measurement error, are described by as many covariance matrices. The covariance matrix related to the multiple scattering is:

$$\boldsymbol{Q} = cov(\boldsymbol{w}) = \begin{pmatrix} z^2 \frac{\theta_{MS}^2}{3} & z \frac{\theta_{MS}^2}{2} \\ z \frac{\theta_{MS}^2}{2} & \theta_{MS}^2 \end{pmatrix} \tag{1.6}$$

where z is the thickness of the plane traversed and θ_{MS} is the multiple scattering angle, defined in 1.1. The measurement error is described by the matrix: $\boldsymbol{V} = \boldsymbol{G}^{-1} = cov(\delta_i) = (\sigma^2)$ where σ^2 is described, in the case of analog readout, by 1.2. A third covariance matrix is used to describe the uncertainty of the state vector: $\boldsymbol{C}_i = cov(\boldsymbol{x}_i - \boldsymbol{x}_i^{true})$.

1.1.1 Filtering Equations

The Kalman filter technique starts by predicting the position on the i-th plane based on the information of the previous plane. The predicted state vector is

$$\boldsymbol{x}_{i,proj} = \boldsymbol{F}_{i-1} \boldsymbol{x}_{i-i}, \tag{1.7}$$

4

to which an uncertainty, given by the sum of the predicted covariance and the effects of the multiple scattering, is associated in the form

$$\boldsymbol{C}_{i,proj} = \boldsymbol{F}\boldsymbol{C}_{i-1}\boldsymbol{F}^T + \boldsymbol{Q}_{i-1}. \tag{1.8}$$

In the limit in which the multiple scattering is 0, $\boldsymbol{C}_{i,proj}$ is simply the propagation of $\boldsymbol{C}_{i-1}$ to the next plane.

Equation 1.7 and 1.8 describe an estimation of the state of the system at the plane i. If a measurement is present on the same plane, being it independent by the prediction, it can be used to refine the prediction. The filtered state vector will be

$$\boldsymbol{x}_i = \frac{(\boldsymbol{C}_{i,proj})^{-1}\boldsymbol{x}_{i,proj} + \boldsymbol{H}^T\boldsymbol{G}_i\boldsymbol{m}_i}{(\boldsymbol{C}_{i,proj})^{-1} + \boldsymbol{H}^T\boldsymbol{G}_i\boldsymbol{H}} = \boldsymbol{C}_i[(\boldsymbol{C}_{i,proj})^{-1}\boldsymbol{x}_{i,proj} + \boldsymbol{H}^T\boldsymbol{G}_i\boldsymbol{m}_i], \tag{1.9}$$

where the filtered covariance matrix for the i-th plane was defined as

$$\boldsymbol{C}_i = [(\boldsymbol{C}_{i,proj})^{-1} + \boldsymbol{H}^T\boldsymbol{G}_i\boldsymbol{H}]^{-1}. \tag{1.10}$$

The smaller the error on our measure (σ^2), the greater the contribution of the measure in the filtering step. In the limit case in which there is no error in our measurement ($\sigma^2 = 0$), the filtered state vector would became the measure itself. A weight for each measurement is defined as the distance between the measured hit and the predicted position. In the case of more than one hit on the same plane, the hit with the lowest weight value is chosen as the one belonging to the track. As it can be seen by these equations, the extent to which a new measure adds more information to the reconstruction is weighted by the inverse of the measurement error. The subsequent use of prediction and filtering can be used on all the consecutive planes. The state vector related to the last plane will inherit all the information from the previous planes. A schematic view of the process is presented in fig. 1.1.

1.1.2 Smoothing Equations

The smoothing phase brings the information from the last plane to the first, further refining it, thus reconstructing the direction of the impinging particle. First a gaining matrix is defined as

$$\boldsymbol{A}_i = \boldsymbol{C}_i\boldsymbol{F}_i^T(\boldsymbol{C}_{i+1,proj})^{-1} \tag{1.11}$$

The smoothed state vector for the plane i will be

$$\boldsymbol{x}_{i,smooth} = \boldsymbol{x}_i + \boldsymbol{A}_i(\boldsymbol{x}_{i+i,smooth} - \boldsymbol{x}_{i+i,proj}) \tag{1.12}$$
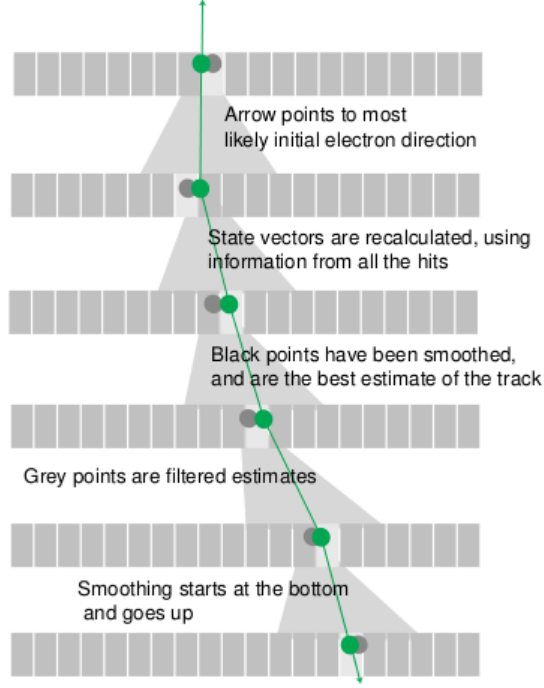
Figure 1.2: Smoothing process of the Kalman filter [4].

and its covariance matrix

$$\boldsymbol{C}_{i,smooth} = \boldsymbol{C}_i + \boldsymbol{A}_i(\boldsymbol{C}_{i+1,smooth} - \boldsymbol{C}_{i+1,proj})\boldsymbol{A}_i^T \tag{1.13}$$

Iterating the smoothing phase to the first plane it will give the initial inclination of the track, as seen in fig.1.2.

The Kalman filter also gives a parameter which indicates the quality of the fit by defining a residual and a weight for each plane. The residual vector for the plane i is

$$\boldsymbol{r}_i = \boldsymbol{m}_i - \boldsymbol{H}\boldsymbol{x}_{i,smooth} \tag{1.14}$$

The covariance matrix of the residuals, which again depends on both the multiple scattering and the measurement error, takes the form

$$\boldsymbol{R}_i = \boldsymbol{V}_i - \boldsymbol{H}\boldsymbol{C}_i\boldsymbol{H}^T \tag{1.15}$$

The χ^2 of a single plane is then $\chi_i^2 = \boldsymbol{r}_i^T \boldsymbol{R}_i^{-1} \boldsymbol{r}_i$. The total χ^2 of the track can be obtained by summing the χ^2 of all the planes. The χ^2 value is used to reject tracks results of a bad reconstruction.

1.1.3 Implementation

The Kalman filter is implemented in the framework code in the same way it is used for the reconstruction algorithm of AGILE [5], treating separately the two views, x and y.

At first, in order to not affect the total effective area in the Compton regime, the vertex was identified by using the default algorithm of MEGAlib. A vertex needs:

- to be the only hit on its layer

- to have at least two layers below it with exactly two hits

- to have no hits above it

Once the vertex is identified, the event is labeled as a pair event and the Kalman filter is used to reconstruct a total of two, one per particle, tracks per view. The choice of the same hit for two different tracks is disfavoured by applying a weight. During this process the energy of the particle is estimated using the multiple scattering. As stated in the previous section, and visible in eq. 1.6, the goodness of the track reconstruction depends on the knowledge of the multiple scattering which in turn depends on the estimation of the particle energy. Once a first iteration, with a fixed energy, of the track reconstruction is performed, the variation of the inclination of the track is computed. This variation provides an indication of the intensity of the multiple scattering. Knowing the radiation length of a plane and reversing eq 1.1, it is possible to estimate the energy of the particle. If this estimation is a factor of 3 different, bigger or smaller, from the energy used in the iteration to reconstruct the track, a new reconstruction is performed using the energy just estimated.

The results of the aforementioned process are four tracks: one for each particle, e^- and e^+, for each view. It is necessary to combine the tracks corresponding to the same particle in different views. Geometrically an ambiguity arises in which, as seen on the left of fig. 1.3, two possible combinations, and consequently two possible three dimensional tracks, are both solution of the combination of the two views. The energy estimation described above is used to discriminate between these two cases: the most energetic track in one view is associated to the most energetic track in the other view in order to obtain the right solution [6].

Once the three-dimensional tracks of the e^- / e^+ pair are computed, the original gamma-ray direction is obtained as the bisector of the tracks, using a simple sum of the components of the two, weighted on their corresponding energy. Using for the reconstruction the bisectors of the two tracks in the separate views instead, could lead to an error for all the off-axis events, as seen on the right of fig. 1.3 [6]. The weighting on the energy is necessary, particularly at very high energy where the probability of an uneven division of the energy in the pair is not negligible.
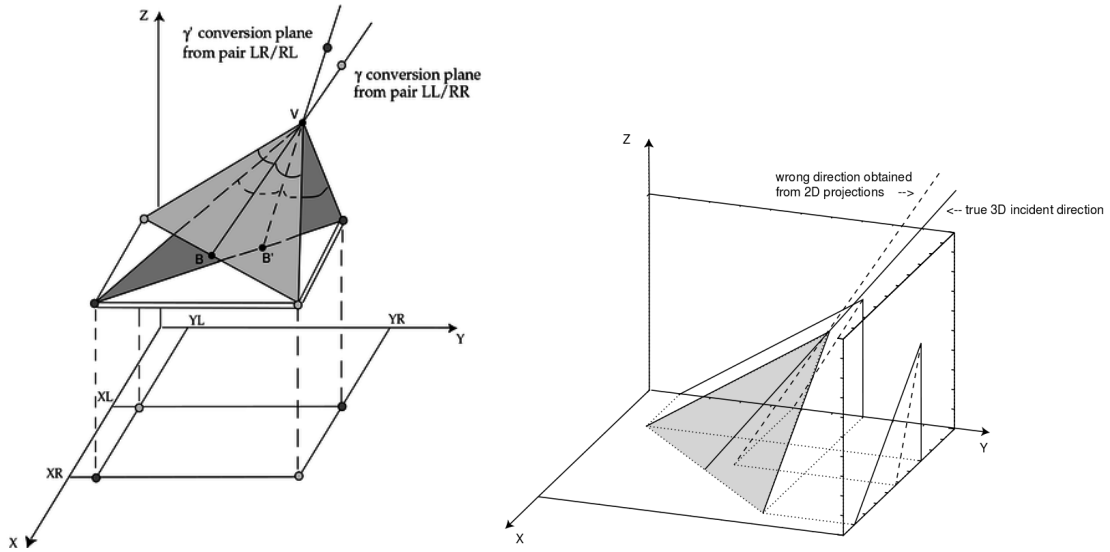
Figure 1.3: *Left*: Ambiguity related to the lack of knowledge of the corresponding track in each view [6]. *Right*: difference between the bisector of the two three dimensional tracks and the reconstructed bisector [6].

1.2   Kalman3D: Double-sided Silicon

In the case of the double-sided Silicon, each measurement provide both the x and y coordinate of the hit. While the method described above can be implemented, a different approach is also proposed. The idea for this approach comes from the realization that, treating the two views separately in the reconstruction caused some unexpected problems. For example: if on one plane we measure two points, A with coordinates (5,-10) and B (6, -9). Working with the two separates view and combining them afterwards might lead to the use of a point (5, -9) or (6, -10), through which a particle never passed. This could happen on just one or two planes out of all the planes used.

The state vector, previously defined as

$$\boldsymbol{x}_k = \begin{pmatrix} x \\ tan(\theta_x) \end{pmatrix}$$

could be redefined as:

$$\boldsymbol{x}_k = \begin{pmatrix} x \\ tan(\theta_x) \\ y \\ tan(\theta_y) \end{pmatrix}$$

8

hence calculating the three dimensional particle track in only one application of the Kalman filter instead of two. This approach would eliminate the ambiguity related to the lack of knowledge of the corresponding track in each view described above. θ_x and θ_y (the projections of the 3D angle) where chosen as angles instead of e.g. θ and ϕ in order to not introduce cross dependencies between x and y in the propagation matrix, that look like this:

$$\boldsymbol{F}_{i-1} = \begin{pmatrix} 1 & d_{i-1,i} & 0 & 0 \\ 0 & 1 & 0 & 0 \\ 0 & 0 & 1 & d_{i-1,i} \\ 0 & 0 & 0 & 1 \end{pmatrix}$$

Similarly:

$$\boldsymbol{Q} = \begin{pmatrix} z^2 \frac{\theta_{MS}^2}{3} & z\frac{\theta_{MS}^2}{2} & 0 & 0 \\ z\frac{\theta_{MS}^2}{2} & \theta_{MS}^2 & 0 & 0 \\ 0 & 0 & z^2\frac{\theta_{MS}^2}{3} & z\frac{\theta_{MS}^2}{2} \\ 0 & 0 & z\frac{\theta_{MS}^2}{2} & \theta_{MS}^2 \end{pmatrix}$$

$$\boldsymbol{H} = \begin{pmatrix} 1 & 0 & 0 & 0 \\ 0 & 0 & 0 & 0 \\ 0 & 0 & 1 & 0 \end{pmatrix}$$

$$\boldsymbol{G} = \begin{pmatrix} 1/\sigma^2 & 0 & 0 & 0 \\ 0 & 0 & 1/\sigma^2 & 0 \\ 0 & 0 & 0 & 0 \end{pmatrix}$$

$$\boldsymbol{m}_k = \begin{pmatrix} x \\ 0 \\ y \end{pmatrix}$$

So, e.g., the filtered state vector (eq. 1.9) will become:

$$\boldsymbol{x}_i = \boldsymbol{C}_i[(\boldsymbol{C}_{i,proj})^{-1}\boldsymbol{x}_{i,proj} + \boldsymbol{H}^T\boldsymbol{G}_i\boldsymbol{m}_i]$$

$$= \boldsymbol{C}_i \left[(\boldsymbol{C}_{i,proj})^{-1} \begin{pmatrix} x_{i,proj} \\ tan(\theta_x)_{i,proj} \\ y_{i,proj} \\ tan(\theta_y)_{i,proj} \end{pmatrix} + \begin{pmatrix} x/\sigma^2 \\ 0 \\ y/\sigma^2 \\ 0 \end{pmatrix} \right]$$

This method heavily relies on the assumption that, on every plane, the hits on one view are correctly paired to the corresponding hits in the other view. This clusterization process is performed automatically by MEGAlib [7] using a generalized χ^2-statistics to compare all possible combinations of hits:

$$Q_s = \frac{1}{N} \sum_{i,j=1}^{N} \frac{(E_i^n - E_j^p)^2}{(\sigma_i^n)^2 + (\sigma_j^p)^2} \quad \forall \text{ permutations} \qquad (1.16)$$

where σ_i is the error of the energy measurement E_i in the strip i. The algorithm applied to the MEGA prototype recognized roughly 90% of pair events [7].

1.3 Simulations

Gamma rays with the following characteristics were simulated:

- Physics list: LivermorePol

- Number of triggers: 10^6 (10^5 for 3000 MeV for reasons related to disk space and computing time)

- Source: far away point source ($FarFieldPointSource$) at $\theta = 30°$ and $\phi = 180°$

- Spectrum: E^{-2} power-law. The points in all the following plots will correspond to the ranges:

  - 10 MeV: 7.5 MeV - 15 MeV
  - 30 MeV: 15 MeV - 40 MeV
  - 50 MeV: 40 MeV - 60 MeV
  - 100 MeV: 80 MeV - 150 MeV
  - 300 MeV: 150 MeV - 400 MeV
  - 3000 MeV: 2000 MeV - 4000 MeV

These parameters were chosen in order to match the ones used by the Bologna group that lead to the results in Table 4 of [8].

A first analysis was performed with the default algorithm present in MEGAlib. The effective area was calculated as:

$$A_{eff} = A_{start} \cdot \frac{N_{det}}{N_{start}} = 53092.9 \cdot \frac{N_{det}}{N_{start}} \text{cm}^2$$

where A_{start} is the area of the circle from which N_{start} photons are generated, and N_{det} is the number of reconstructed events.

The radius in which 68% of all the reconstructed events falls, as given by *mimrec*, is referred to as PSF or angular resolution in the following. The containment radius is calculated by *mimrec* as follow:

- the original direction of the gamma ray is passed as an input

- the histogram of the angular distance between the original and reconstructed direction is build

- the integral of the histogram is computed

- starting from the first bin, the contents of the bins are added until the results exceed the 68% of the total

1.4 Results

A comparison of the results of the different algorithms is presented in Fig. 1.4. The two implementations of the Kalman filter do not differ significantly, except for a small different in angular resolution around 300 MeV. There is instead a significant improvement in the PSF at the lowest energies with respect to the default MEGAlib algorithm. No significant differences are visible between these three methods in the effective area calculations. Considering that the classification as a pair event, i.e. the identification of a vertex as described in Sec.1.1, is done in the same way in the three cases (to not affect the Compton effective area), the similar effective area indicates a similar efficiency of the reconstruction ($> 90\%$ of the events labeled as pair) in all three cases.

Both the PSF and the effective area obtained by using the Kalman filter are not comparable to the BoGEMMS results. In particular the BoGEMMS effective area at high energy is ~ 6 times bigger than the MEGAlib effective area. It should be noted that, although the BoGEMMS results are (well) educated guesses based on simulations of an incomplete mass model, the difference in performance is too big to be related only to this.

By applying cuts to the χ^2 of the tracks reconstructed with the Kalman filter it is possible to improve the angular resolution at the expense of a lower effective area, as showed in Fig. 1.5. The angular resolution in case of strong cuts is then comparable to BoGEMMS, but with an even bigger difference in effective area.

Being the efficiency of the reconstruction algorithm quite high and the similar results and shape of the effective area curve for the different MEGAlib algorithms (Default and the two Kalman), the cause of the difference was searched not in the
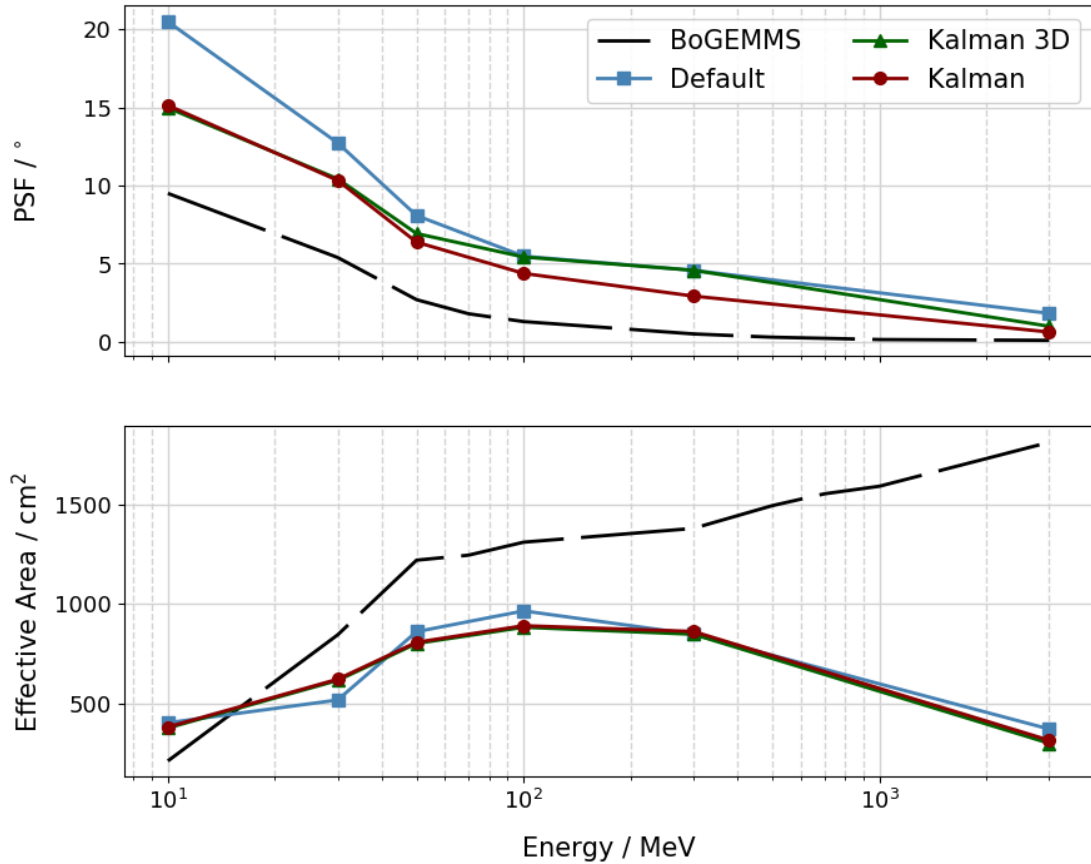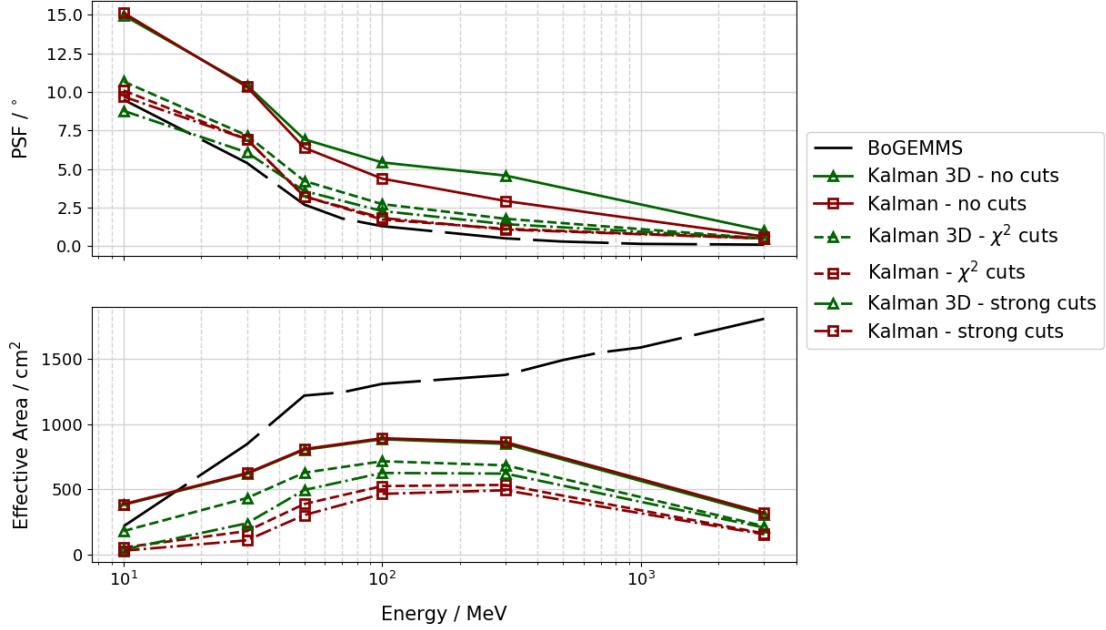
Figure 1.4: Angular resolution (*top*) and effective area (*bottom*) as calculated by BoGEMMS (as calculated in [8]), in black, the default MEGAlib pair reconstruction algorithm, in blue, and the two implementation of the Kalman filter, the classical and the 3D, respectively in red and green.

implementation of the algorithm but elsewhere. The following cross-check between MEGAlib and BoGEMMS were performed:

- Physics list: the physics list used by Geant4 in the two simulation is the same.

- Geometry: there are some differences in the geometries used in the two cases. Most notably, BoGEMMS is using a simplified single tower in the tracker. The total area of the active Silicon is the same in the two cases but, by using a single tower, the number of reconstructed events is higher. This is because, with four towers, some hits might be missing, if the particle e.g. passes through the support between the Si wafers or the space between two towers. Simulation made using MEGAlib and the BoGEMMS geometry demonstrate

12

Figure 1.5: Angular resolution (*top*) and effective area (*bottom*) as calculated by BoGEMMS (as calculated in [8]), and the two implementation of the Kalman filter, the classical and the 3D, respectively in red and green. No quality cuts are applied to the solid lines, while two increasing cuts on the χ^2 of the track are applied to the dashed and dot-dashed lines.

an increase in effective area of only 5-10%, too little to explain the whole difference. The BoGEMMS mass model was, at the time, not surrounded by any anticoincidence system.

- The characteristic of the Silicon (pitch, energy threshold, ...) are the same in the two cases.

An explanation of the difference could come from a different trigger condition used in the two cases. The conditions used for the results in Fig. 1.4 and Fig. 1.5 are:

- Tracker: one or more hits (but at least three planes are needed for successful reconstruction)

- Calorimeter: one or more hits (but without the tracker the event can not be reconstructed)

- Veto top anticoincidence (AC)
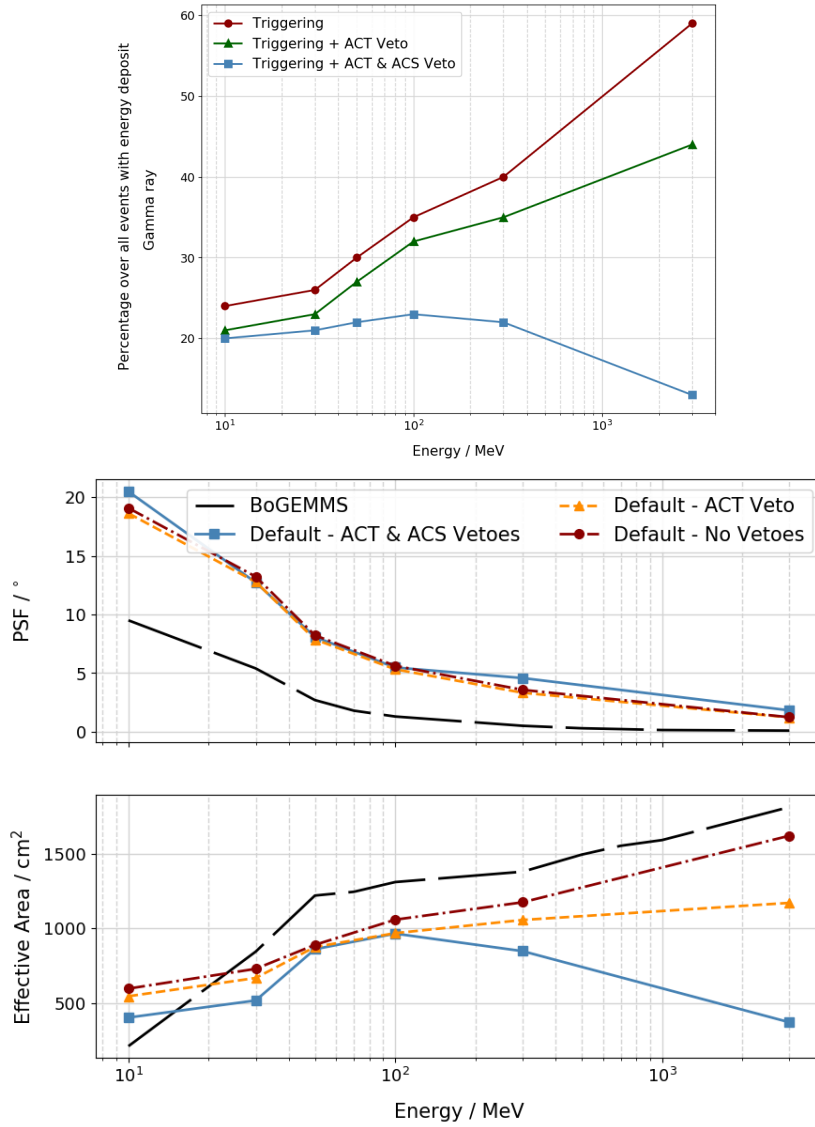
Figure 1.6: *Top*: Surviving percentage of events over the total with an energy deposit, after subsequently applying the trigger (red circles), the veto on the top AC (green triangles), and the side AC (blue squares). *Center and bottom*: Angular resolution (*center*) and effective area (*bottom*) as calculated by BoGEMMS (as calculated in [8]), in black, and the default MEGAlib pair reconstruction algorithm. In blue the results using a veto on both the top and side anticoincidence (AC), in orange using only a veto on the top AC, and in red no veto at all.
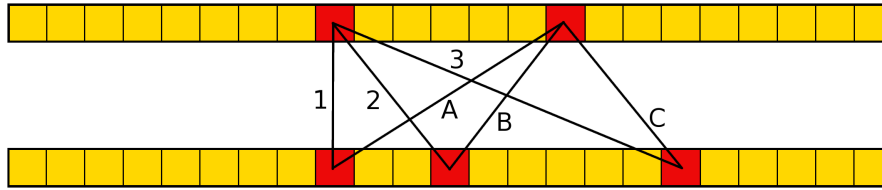
Figure 1.7: Two Si planes with hit strips (in red). The possible combination first-second plane used at the beginning of the implementation of the Kalman filter are shown. For two hits on the first plane and three for the second the combinations are six: three (1,2,3) for the first hit on the first plane and three (A,B,C) for the second hit of the first plane

- Veto side AC

The AC is monolithic and has a threshold of 100 keV.
As shown on the top of Fig. 1.6, most of the triggering high energies gamma rays are self-vetoed by the side AC, with the top AC playing a much smaller role. On the bottom of Fig. 1.6, the same study is shown but taking into consideration the reconstruction as well. While at high energies the results are the same, a difference can be noticed on the energy from which the veto on the side AC is predominant: 100 MeV before reconstruction, >300 MeV after. This difference can be explained by considering all those events which can not be reconstructed because of, e.g., not enough hits in the tracker. Even without any vetoes, the effective area calculated by MEGAlib is significantly lower than the one obtained by BoGEMMS. In the following the veto on the side AC, while important and needed, will not be taken into consideration since a simple veto is too limiting (see the end of this section for a more thorough discussion).
One of the most important, and most difficult, task of the track reconstruction is the identification of the vertex, the first hit of the electron-positron pair created by the gamma ray. In MEGAlib, as described in Sec.1.1, a Λ shape is searched in the tracker. In AGILE this task is accomplished using the very same Kalman filter later used to reconstruct the track itself. The Kalman filter is used on every possible combination of hits on the first two planes, an example of the possible combinations is shown in fig. 1.7. The couple of hits whose track has the least χ^2 is chosen as the vertex.
To try to retrieve the missing reconstructed events, the MEGAlib vertex finding process was changed to the following:

1. The default search for a Λ shape in the tracker is performed. If a vertex is found it is used, as previously, in the Kalman.

2. If the search fails, the approach used in AGILE, just described, is implemented. A condition of a minimum χ^2 on the best found track is also applied
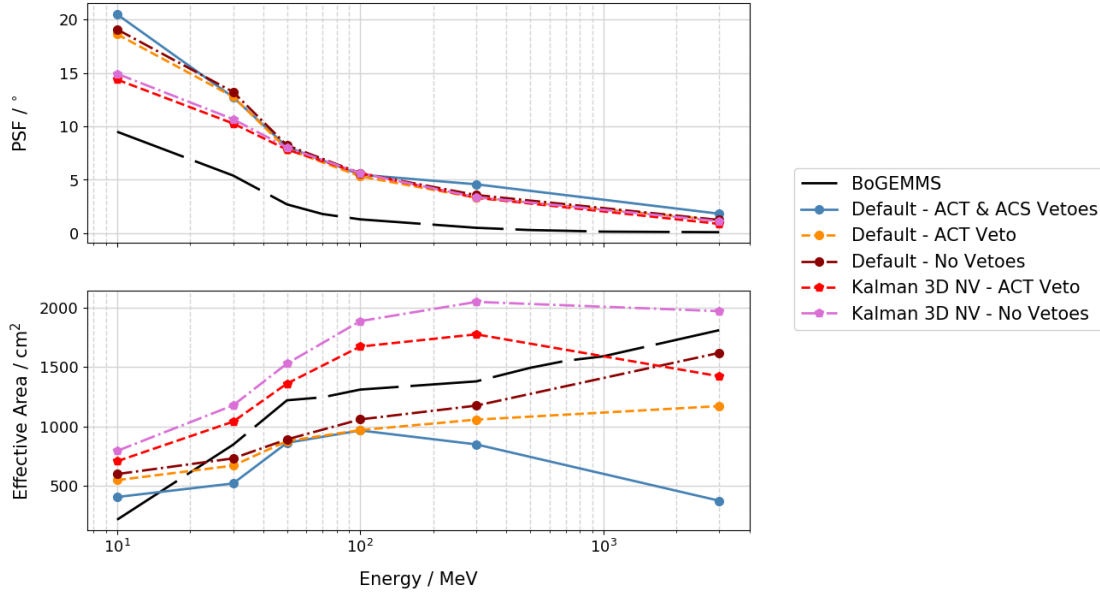
15

Figure 1.8: Angular resolution (*top*) and effective area (*bottom*) as calculated by BoGEMMS (as calculated in [8]), in black, the default MEGAlib pair reconstruction algorithm (circles) and the Kalman in its 3D implementation with the new vertex find algorithm (pentagons). The solid lines are the results using a veto on both the top and side anticoincidence (AC), dashed lines with only the veto on the top AC, and dashed-dot lines for no veto at all.

to ensure a good quality of the search and minimize the number of mislabeled events.

3. If the Kalman filter fails or succeed but with too high χ^2, the event is not considered as created by a pair.

With this approach it is possible to increase considerably the effective area of the instrument while maintaining a similar angular resolution, as shown in Fig. 1.8. The old results can be considered a sub class of the new ones since, if the vertex is found with the default search, the whole process is the same. In Fig. 1.9, the results of applying the quality cuts to the events reconstructed using the new algorithm to find the vertex. There is still a difference at the highest energies in the effective area, most likely related to the BoGEMMS results being a well educated guess, and a difference at mid energies in the angular resolution, probably related to a better refinenement of the reconstruction algorithm. The difference between the performance is not as big as before. The difference between the number of events reconstructed with the two different vertex-finding algorithm is shown in Tab. 1.1. The total number of events that can be successfully identified (as a pair,
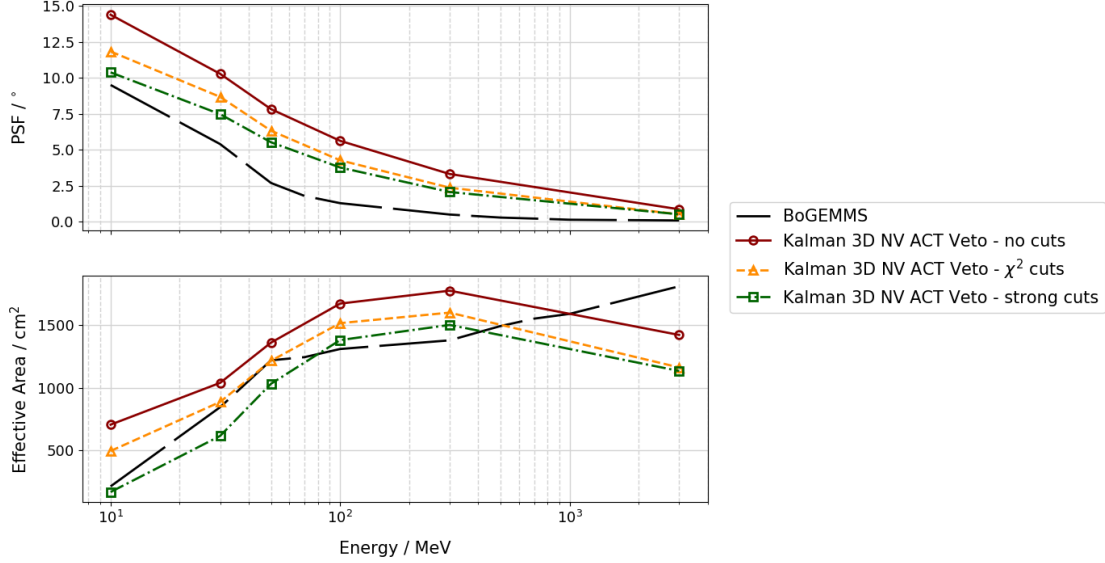
16

Figure 1.9: Angular resolution (*top*) and effective area (*bottom*) as calculated by BoGEMMS (as calculated in [8]), and the Kalman in its 3D implementation with the new vertex find algorithm and the veto on the top AC. No quality cuts are applied to the solid lines, while two increasing cuts on the χ^2 of the tracks are applied to the dashed and dot-dashed lines.

Compton, muon etc...), as well as the events reconstructed as single site, does not change significantly in the two cases. It is always $< 0.05\%$ for the identifiable events (except for a 0.33% at 10 MeV) and $< 0.1\%$ for the single site. The gain in the total number of identified pair is increasing with energy up to 300 MeV, then it decrease again at the highest energy, as already visible in Fig. 1.8. The newly reconstructed events were not previously reconstructed as Compton, for which there is a change of a 0.5% at the extreme of the energy range and $\sim 0.04\%$ in the mid-energy range. A study on the final Compton performance needs to be done in order to exclude that the new events are coming exclusively from, e.g., tracked Compton events. In any case it appears that they will remain mostly unchanged. Some of the gain comes from events that were mis-reconstructed as muons, but the largest part is due to events previously mislabeled as other types (otherwise the total number of identifiable events would have changed) and of which the reconstruction was subsequently failing.

While improving the precedent results, MEGAlib, even with the introduction of a Kalman filter, is still worse performing than BoGEMMS. One should consider also that the results in Fig. 1.9 were obtained only with the veto of the top AC. A less drastic veto on the lateral AC can be thought using its segmentation (already

| | Percentage | | | | | |
	10 MeV	30 MeV	50 MeV	100 MeV	300 MeV	3000 MeV
Identifiable	0.33	0.03	0	0.02	-0.01	0.05
Reconstructed Single site	0	0.1	0	0	-0.09	0.11
Compton	0.53	-0.3	-0.19	0.04	-0.04	0.49
Pair	32.57	61	71.54	78.08	74.36	21.66
Muon	-14.5	-34.27	-41.11	-42.39	-37.23	-25.89

Table 1.1: Change in percentage of the number of events reconstructed with the new algorithm for the finding of the vertex. Negative value denotes a loss of events

foreseen in the M5 call). Different solutions are used in both Fermi and AGILE in order to reject the least amount of gamma ray possible. As an example, in AGILE the level-1 trigger [9] uses the following conditions, subsequently applied:

1. Events with hits in at least 3 out of 4 consecutive planes in the x or y view

2. Events that pass the top AC veto

3. Events with signals in 0 or 1 lateral AC panel, and events with signal in 2 consecutive panels or 2 panels on the same side

4. Events with no signal on the lateral AC, and with signal in 1 or 2 panels and R>1.1. R is defined as the ratio between the number of TA1 chips (that read out the Si strips) fired and the total number of fired x and y views.

Applying this kind of trigger would not affect events with a Compton track (the ratio R is used only if 1 or 2 lateral AC panels are hit) but would allow to not veto a substantial number of gamma ray. For example, for the simulation at 3 GeV, supposing that the condition on R is satisfied, the percentage of surviving events allowing 0, 1 or 2 hits on the AC increases from 8% to 31% and 43% (a loss of 1% with respect to only the top AC veto). This will be particularly important for higher energies, to not limit the instrument FOV.

1.5 AMEGO

Being the mass model used to create the official AMEGO results ([10], also called AMEGO-US in the following) available online [11], a comparison has been made with the e-ASTROGAM results.
The official AMEGO results were obtained using MEGAlib for the simulations and
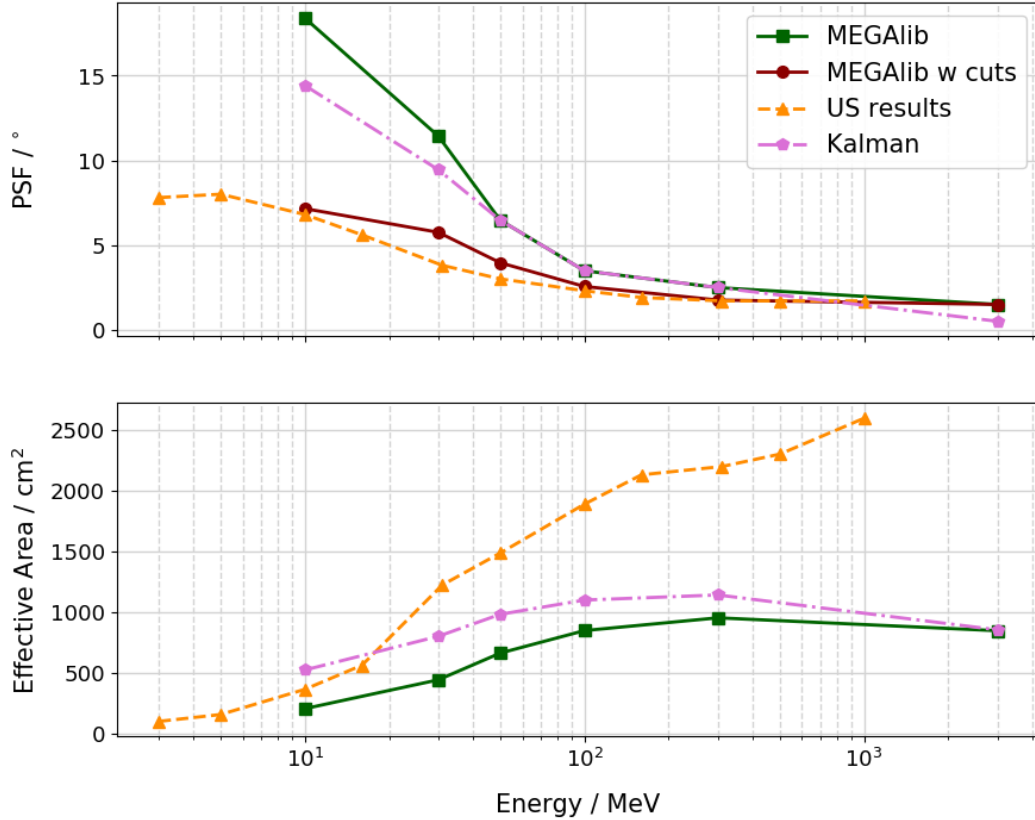
Figure 1.10: Angular resolution (*top*) and effective area (*bottom*) of AMEGO as calculated by the default MEGAlib pair reconstruction algorithm (green squares), adding the cuts presented in the text (red circles), and using the Kalman filter (pink pentagons). The official AMEGO performance at 37° are showed as yellow triangles.

reconstruction of the events [12]. A dedicated Python code [13] was then used to compute PSF and effective area.

For a direct comparison with our previous e-ASTROGAM results, simulations were made in the exact same conditions: FarFieldPointSource, with theta equal to 30 deg.

As a first step the default MEGAlib pair reconstruction algorithm was used. Since the AMEGO-US pipeline differs only for the very last step of the calculation, an equivalence in the results is expected. As Fig. 1.10 shows, the results are worse then the official one in both PSF, especially at low energy, and effective area, increasingly with energy. After looking at the Python code used to calculate the official results, the differences might come from two separates things:
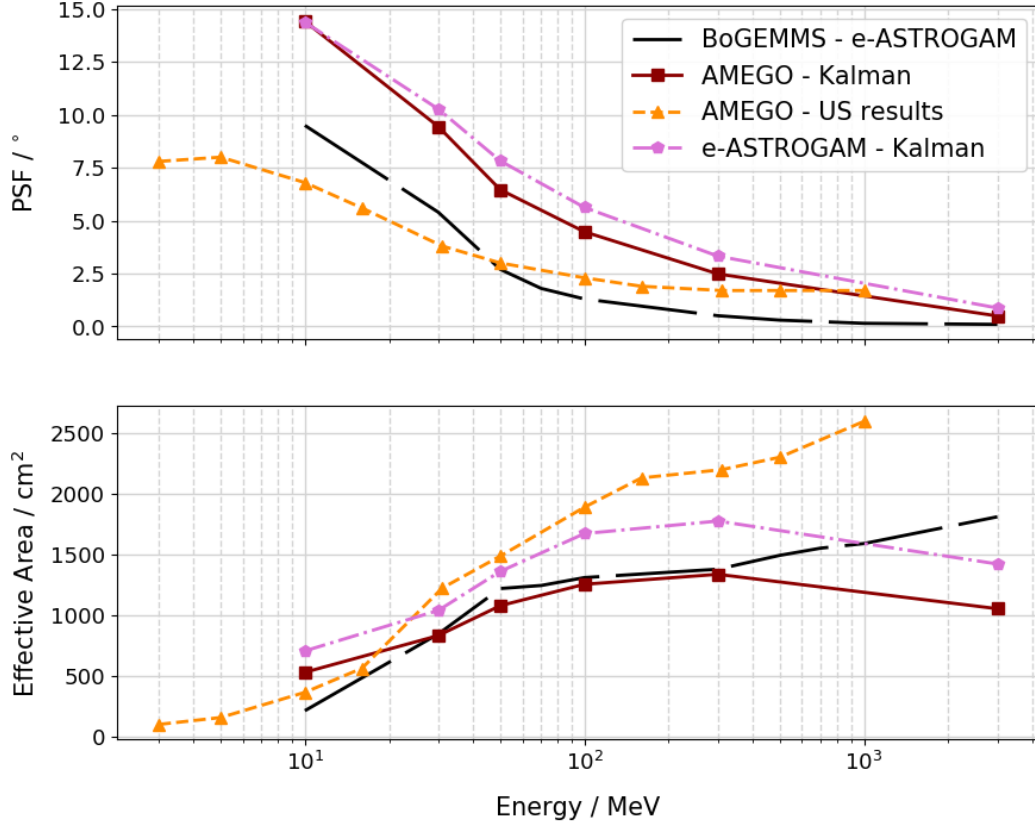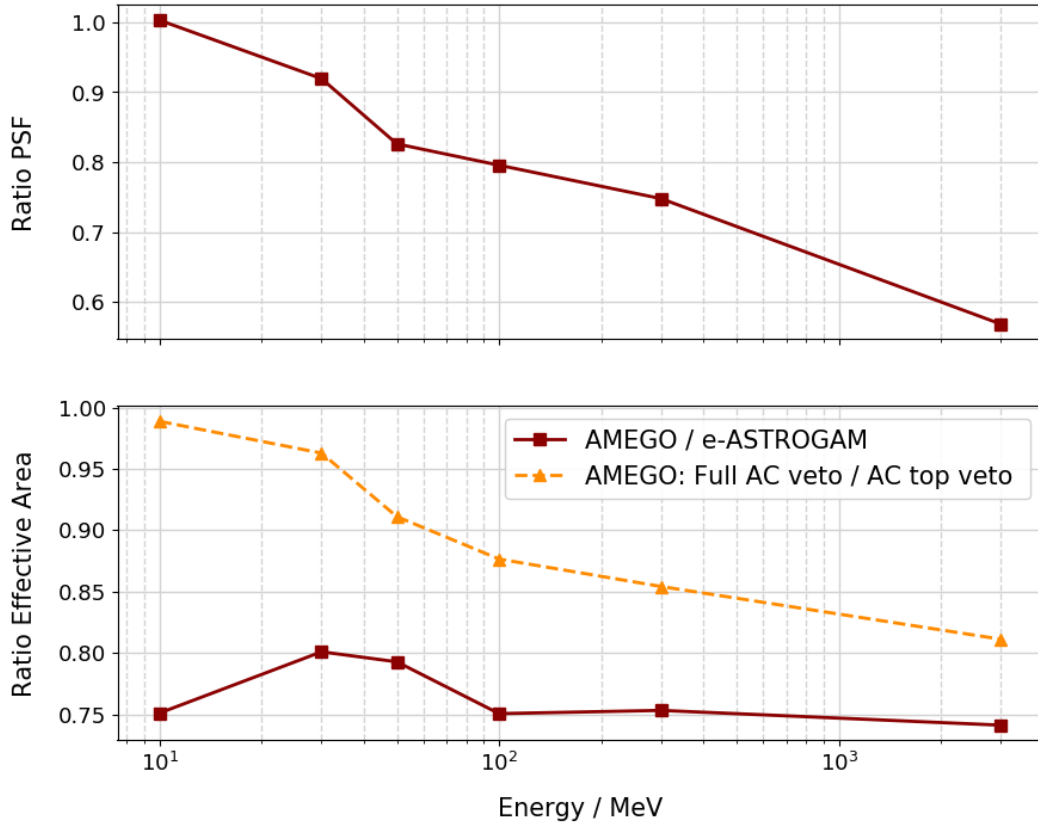
Figure 1.11: Angular resolution (*top*) and effective area (*bottom*) of AMEGO and e-ASTROGAM as calculated by the Kalman filter, together with the BoGEMMS and AMEGO official performance.

- For the effective area, instead of using the reconstructed events, it seems that the not reconstructed (or "bad" events) are used instead. Using the same events with our simulations the effective area increases from 954 to 2373 cm^2 at 300 MeV, where the official result is $\sim$2200 cm^2, and to 1135 cm^2 at 100 MeV, where the official result is $\sim$1800 cm^2. The AMEGO simulation group intended to use the number of triggered events to calculate the effective area, foreseeing an improvement on the reconstruction code that would increase efficiency. It is certainly true that the number of events reconstructed by MEGAlib underestimate the true effective area, but this is related to the correct identification of pair events rather than on the reconstruction efficiency. Considering all triggered events, being two or more hits in the tracker the trigger condition, might lead to an overestimation as well since a two hits track is not always well reconstructed. There is also no condition on the position of the hits: they could be far away from each other or

20

Figure 1.12: Angular resolution (*top*) and effective area (*bottom*) ratios between the AMEGO and e-ASTROGAM performance as calculated with the Kalman filters, in red, and the ratio between the AMEGO effective areas obtained using a veto only on the top anticoincidence or on both the top and sides.

belong to the same plane.

- The angular resolution seems to be calculated without changing a default condition on the fit range of the angle, limited to 10°, meaning that all events with a reconstructed angular distance from the source greater than 10° are not used. This cut would suppose the knowledge of the source position and it is not indicated for performance calculation. The effect of this cut is smaller at higher energies because the actual PSF is already significantly smaller than 10°. Applying this condition directly in MEGAlib to our results lead to the red curve in Fig. 1.10, comparable with the official results. The AMEGO official angular resolution is calculated by a fit to the histogram data. In order for the fit to converge at high energies the cut was introduce, and apparently forgot when analysizing the low energy simulations.

	AMEGO	e-ASTROGAM
Tracker	60 planes (4×4 wafers)	56 planes (5× 5 wafers)
Wafer guard ring	No	1.5 mm
Tracker electronics	No	Yes
Strip pitch	0.5 mm	0.239 mm
Strip noise threshold	10 keV	7 keV
Strip trigger threshold	20 keV	15 keV
AC thickness	1.5 cm	1 cm
AC trigger threshold	500 keV	100 keV

Table 1.2: Change in percentage of the number of events reconstructed with the new algorithm for the finding of the vertex. Negative value denotes a loss of events

Fig. 1.11 and 1.12 show a comparison of the e-ASTROGAM and AMEGO results obtained using the Kalman filter. It must be noted that the AMEGO mass model seems a little less detailed than the e-ASTROGAM one. The most important differences for the analysis presented here are reported in tab. 1.2. The 20-25% difference in the effective area is slightly smaller that the difference in geometrical area (27%), but compatible with, e.g., the lack of guard ring and electronics in the AMEGO tracker.
The differences in the tracker description and the Silicon characteristics (noise and trigger threshold) might be also partly responsible for the differences in the angular resolution. It is in any case interesting that the high energy AMEGO results, where the multiple scattering is negligible, are better than the ones from e-ASTROGAM, even though the pitch is twice as wide. Simulations changing only the strip pitch should be made in order to confirm or disprove the need of such a fine pitch to have better performance at high energy.
Differently from e-ASTROGAM, where an $\sim 80\%$ loss in effective area of is observed at 3 GeV when a veto on the side anticoincidence is implemented, in AMEGO only a 20% difference is observed at the same energy. This is most likely due to the higher, by a factor of 5, trigger threshold. To choose the best trigger threshold for the anticoincidence, a simulations of the full on-orbit background, and a study on the trigger, are necessary.

1.6 Conclusions

A first version of the Kalman filter has been implemented in MEGAlib leading to an improvement of the performance in the pair regime. In particular, the Kalman filter improves the PSF at low energy ($E < 50$ MeV) and the new approach to the problem of finding a vertex improves the effective area on the whole energy

range, seemingly without affecting the Compton performance. A study on the trigger, especially on how to effectively use the anticoincidence segmentation to lower the self-veto of gamma-ray events, is found to be necessary.

The implementation of the Kalman filter as presented here is a simple approach to the problem that can be surely improved. For example, the use of information from the calorimeter would help in the estimation of the energy of the pair which, as of now, is inferred only from the multiple scattering of the particles. A better knowledge of the energy is helpful for the direction reconstruction, as discussed in section 1.1, given the relation between energy and multiple scattering.

The implemented reconstruction algorithm was used to compare the AMEGO and e-ASTROGAM performance in the pair regime:

- The official AMEGO results on effective area and angular resolution seems to be affected by two separate bugs.

- The effective area difference between the two instrument is slightly smaller than difference in geometrical area, but the AMEGO tracker seems to be missing some details like electronics and guard ring around the Si wafers.

- The AMEGO angular resolution is better than the e-ASTROGAM, increasingly with energy, even though the pitch is twice as wide. Studies using the same instrument characteristic but different pitches should be made to confirm or disprove the need of such a fine pitch.

- A possible higher anticoincidence trigger threshold should be investigated, including background simulations.

Bibliography

[1] R. Frühwirth. Application of Kalman filtering to track and vertex fitting. *Nuclear Instruments and Methods in Physics Research A*, 262:444–450, December 1987. doi: 10.1016/0168-9002(87)90887-4.

[2] J. Beringer et al. (Particle Data Group). Review of particle physics. *Physical Review D*, 86:010001, 2012.

[3] R. Turchetta. Spatial resolution of silicon microstrip detectors. *Nuclear Instruments and Methods in Physics Research A*, 335:44–58, October 1993. doi: 10.1016/0168-9002(93)90255-G.

[4] B. B. Jones. A Search for Gamma-Ray Bursts and Pulsars, and the Application of Kalman Filters to Gamma-Ray Reconstruction. *ArXiv Astrophysics e-prints*, February 2002.

[5] A. Giuliani. Studio e Ottimizzazione della Risoluzione Angolare del Telescopio Spaziale per Astronomia Gamma AGILE,. Master Thesis, Università degli Studi di Pavia, 2001.

[6] C. Pittori and M. Tavani. Gamma-ray imaging by silicon detectors in space: the AREM method. *Nuclear Instruments and Methods in Physics Research A*, 488:295–306, August 2002.

[7] A. C. Zoglauer. *First light for the next generation of Compton and pair telescopes : Development of new techniques for the data analysis of combined Compton and pair telescopes and their application to the MEGA prototype.* PhD thesis, PhD Thesis, Garching: Max-Planck-Institut für Extraterrestrische Physik, 2006, MPE Report, No. 289, 2006.

[8] A. De Angelis, V. Tatischeff, M. Tavani, U. Oberlack, I. Grenier, L. Hanlon, R. Walter, A. Argan, P. von Ballmoos, A. Bulgarelli, I. Donnarumma, M. Hernanz, I. Kuvvetli, M. Pearce, A. Zdziarski, A. Aboudan, M. Ajello, G. Ambrosi, D. Bernard, E. Bernardini, V. Bonvicini, A. Brogna, M. Branchesi, C. Budtz-Jorgensen, A. Bykov, R. Campana, M. Cardillo, P. Coppi,

24

456 D. De Martino, R. Diehl, M. Doro, V. Fioretti, S. Funk, G. Ghisellini,
457 E. Grove, C. Hamadache, D. H. Hartmann, M. Hayashida, J. Isern, G. Kan-
458 bach, J. Kiener, J. Knödlseder, C. Labanti, P. Laurent, O. Limousin, F. Longo,
459 K. Mannheim, M. Marisaldi, M. Martinez, M. N. Mazziotta, J. McEnery,
460 S. Mereghetti, G. Minervini, A. Moiseev, A. Morselli, K. Nakazawa, P. Or-
461 leanski, J. M. Paredes, B. Patricelli, J. Peyré, G. Piano, M. Pohl, H. Ramar-
462 ijaona, R. Rando, I. Reichardt, M. Roncadelli, R. Silva, F. Tavecchio, D. J.
463 Thompson, R. Turolla, A. Ulyanov, A. Vacchi, X. Wu, and A. Zoglauer. The
464 e-ASTROGAM mission. Exploring the extreme Universe with gamma rays in
465 the MeV - GeV range. *Experimental Astronomy*, 44:25–82, October 2017. doi:
466 10.1007/s10686-017-9533-6.

467 [9] F. Longo, V. Cocco, and M. Tavani. Simulation of the AGILE gamma-ray
468 imaging detector performance: part I. *Nuclear Instruments and Methods in*
469 *Physics Research A*, 486:610–622, July 2002. doi: 10.1016/S0168-9002(01)
470 02159-3.

471 [10] AMEGO official results: `https://asd.gsfc.nasa.gov/amego/technical.`
472 `html`, .

473 [11] AMEGO mass model: `https://github.com/ComPair/Geometry/tree/`
474 `CZTAngerCamera/AMEGO_4x4TowerModel`, .

475 [12] Simulation, Reconstruction and Data Analysis Summary:
476 `https://docs.google.com/document/d/166RIKOEHLwOIQNMr_`
477 `m5gxpLsoIOPjKXU6FInDtkm4Lk/edit`.

478 [13] Python code for AMEGO analysis: `https://github.com/ComPair/python/`,
479 .

eASTROGAM
Instruments optimizations for low energy Gamma-ray detection

Gonzalo Rodriguez, Aldo Morselli
Sezione INFN di Tor Vergata, Roma

Abstract

There is an experimental gap in the study of the non-thermal universe in the photon energy range from 300 kev to 3 GeV. We have analysed the performance of a detector with unprecedented sensitivity, angular and energy resolution and combined with polarimetric capability to study of the most powerful Galactic and extragalactic sources and with a line sensitivity in the MeV energy range two orders of magnitude better than previous generation of instruments that can determine the origin of key isotopes fundamental for the understanding of supernova explosion and the chemical evolution of our Galaxy.

Introduction

e-ASTROGAM is a gamma-ray space mission that have been proposed as the M5 Medium-size mission of the European Space Agency. It is a gamma-ray instrument that inherits from predecessors such as AGILE and Fermi, as well as from the MEGA prototype, but it takes full advantages of recent progresses in silicon detectors and readout microelectronics to achieve measurement of the energy and 3D position of each interaction within the detectors with an excellent spectral and spatial resolution. The main innovative feature of the e-ASTROGAM mission is the capability of joint detection in the Compton (0.2 – 30 MeV) and pair (> 10 MeV) energy ranges in a single integrated instrument. The mission aims at improving the sensitivity in the medium-energy gamma-ray domain by one to two orders of magnitude compared to previous missions, and it can provide a groundbreaking capability for measuring gamma-ray polarization giving access to a new observable that can provide valuable information on the geometry and emission processes of various high-energy sources.

The e-ASTROGAM telescope

The e-ASTROGAM telescope is made up of three detection system: a silicon Tracker in which the cosmic gamma rays undergo a Compton scattering or a pair conversion, a Calorimeter to absorb and measure the energy of the secondary particles, and an anticoincidence (AC) system to veto the prompt-reaction background induced by charged particles. The telescope has a size of 110x110x80 cm^3 and a mass of 820 kg.
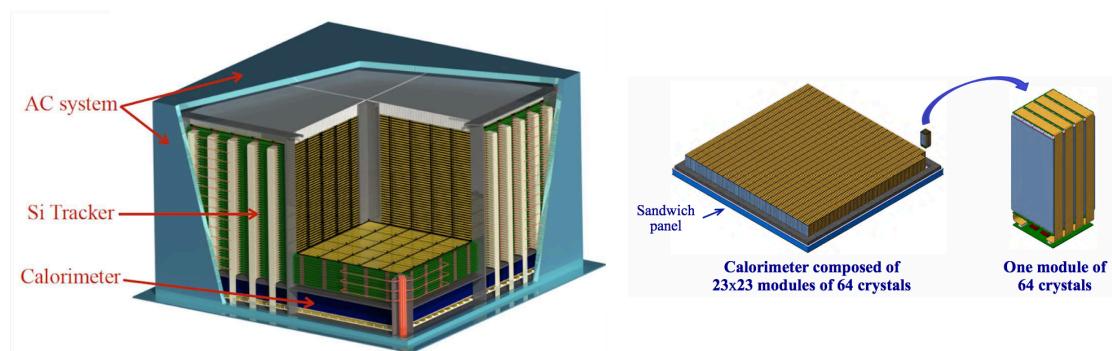
Silicon Tracker

The e-ASTROGAM Tracker is a double-sided strip detectors (DSSD) that comprises 5600 DSSDs arranged in 56 layers. It is divided in four units of 5x5 DSSDs, the detectors being wire bonded strip to strip to form 2-D ladders. The interlayer distance is 10 mm. Each DSSD has a geometric area of 9.5x9.5 cm^2, a thickness of 500 μm, and a strip pitch of 240 μm. The total detection area amounts to 9025 cm^2 and the total Si thickness to 2.8 cm, which corresponds to 0.3 radiation length on axis.

Calorimeter

The e-ASTROGAM Calorimeter is a pixelated detector made of a high-Z scintillation material – Thallium activated Cesium Iodide. It consists of an array of 33,856 parallelepiped bars of CsI(Tl) of 8 cm length and 5x5 mm^2 cross section, read out by silicon drift detectors (SDDs) at both ends, arranged in an array of 529 (= 23x23) elementary modules comprising each 64 crystals. The Calorimeter thickness – 8 cm of CsI(Tl) – makes it a 4.3 radiation length detector having an absorption probability of a 1-MeV photon on axis of 88%.

Anticoincidence system

The third main detector of the e-ASTROGAM payload consists of an Anticoincidence (AC) system made of segmented panels of plastic scintillators covering the top and four lateral sides of the instrument, requiring a total active area of about 4.7 m^2. The AC detector is segmented in 33 plastic tiles (6 tiles per lateral side and 9 tiles for the top). All scintillator tiles are coupled to silicon photomultipliers (SiPM) by optical fibers.

Silicon Tracker: Geometry optimization

We have focus our optimization studies on the silicon tracker geometry. We have perform the simulations, the reconstruction and analysis of the events using the MEGAlib framework. MEGAlib was develop to simulate tracker detectors in the Compton regime, and recently was update to include also the pair production regime. The detector is simulated using a wrapped of the well know Geant4 framework. The output of the simulations is reconstructed using the tools revan and mimrec.

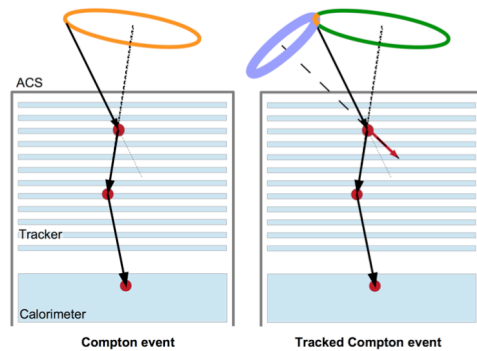We have perform two sets of simulations:
Compton regime:
> - Energy: [300, 5000] keV
>   - Zenith angle: [0, 90] degrees
> - Thickness: [100, 550] μm
> - Number of Layers: 56, 70, 112
> - Distance between Layers: 0.5, 0.75, 1.0 cm

Pair Production regime:
> - Energy: [300, 5000] keV
>   - Zenith angle: 0 degrees
> - Thickness: [250, 550] μm
> - Number of Layers: 56, 70, 112
> - Distance between Layers: 0.5, 0.75, 1.0 cm

Compton regime

In the energy range from 0.3 to 5 MeV we measured the proprieties of the incident photon using the Compton effect. From the interaction we have two products, a photon and an electron. If the electron have enough energy will escape the silicon layer and will be detect as it hits other layers. Otherwise we will only have the hits from the photon. We have to distinguish between events with electron tracking and without electron tracking. This will have implications in the angular resolution.

Energy Resolution – Photopeak events
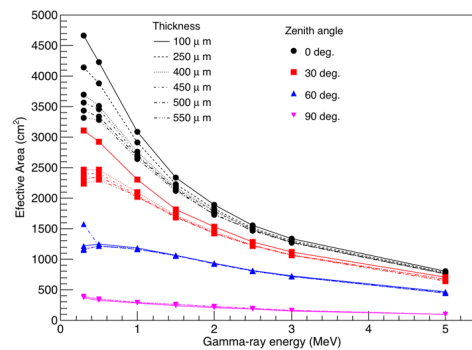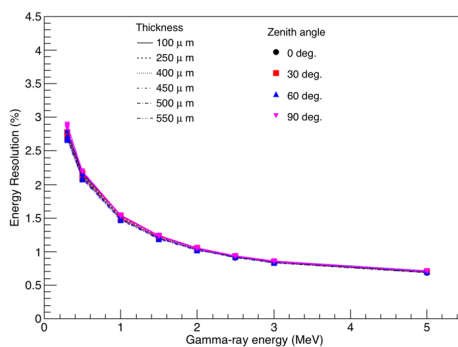
We have to use the photopeak events to calculate the energy resolution in the Compton regime. In the above figure we show the results, in the left panel we see that the energy resolution does not depends on any geometrical parameters use in the simulation. We have observe an energy resolution of 3% at low energies that decrease to about ~1% at 5 MeV. In the right panel we show the dependence of the effective area for the different thickness and zenith angles.
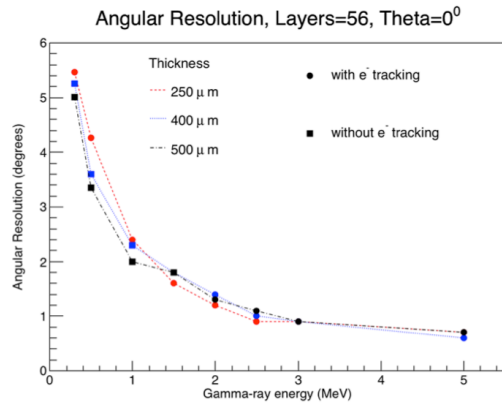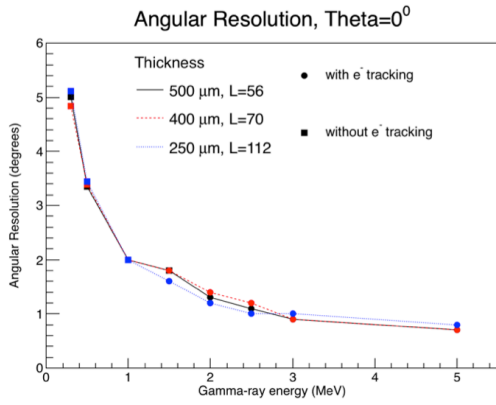
Angular Resolution – Compton events
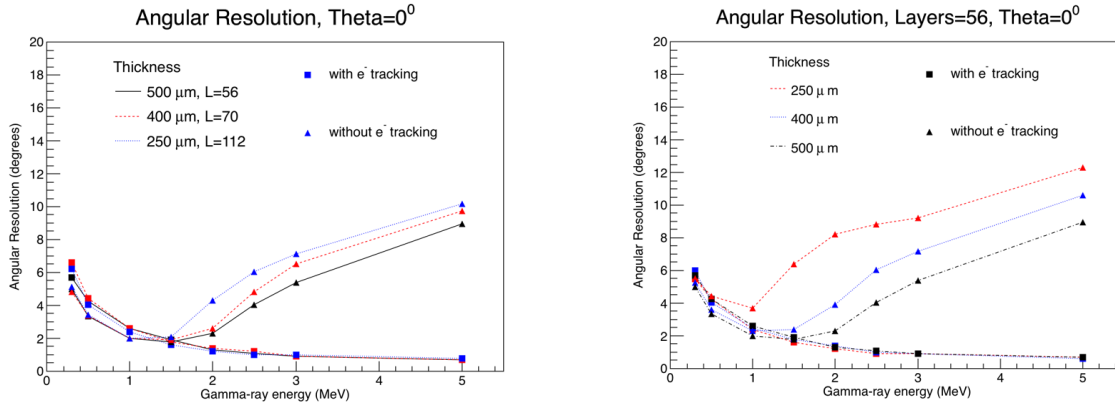
For the angular resolution we have to take into account the events reconstructed w/o electron tracking. For simplicity we show the results for events simulated with zenith angle at 0 degrees.

In the above figure we show, on the left panel, the results for 3 different thickness when we have fixed the number of total radiation lengths to $0.3X_0$. For events without electron tracking, triangles points, we observe that at approximately ~1.5 MeV the resolutions start to get worst for all thickness. This is not the case for the reconstructed events with electron tracking, square points, the angular resolutions gets better as the energy increase, going from ~6° at 0.3 MeV to ~1° at 5 MeV. For energies below ~1.5 MeV both reconstruction give approximately the same angular reconstruction.

In the right panel, we show the results for geometries with different thickness but the same number of layer, in this case 56. For events with electron tracking we observe the same results when the total radiation length was fixed. We have found a different situation when we have reconstructed events with no electron tracking. In this case depending on the thickness the angular resolutions start getting worst at different energies. We can see that for 250 microns at energies less than 1 MeV the angular resolutions start decreasing, but for 400 and 500 microns this behaviour start at 1.5 MeV or above.

It is clear that we have to make an event selection to obtain the best angular resolution as a function of the energy and for each simulated geometry.

For each energy we just have keep the reconstruction that minimize the angular resolution.

5

Angular Resolution, Theta=0° | Angular Resolution, Layers=56, Theta=0°

In the Figure above we show the results of the angular resolution after the event selection. As we can observe regardless of the geometry we have obtain the same angular resolution within the uncertainties. The angular resolution goes from ~5° at 0.3 MeV to ~1° at 5 MeV.

ARM Effective Area, Theta=0° | ARM Effective Area, Layers=56, Theta=0°
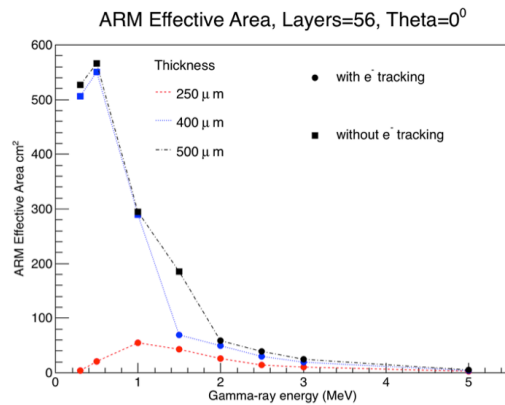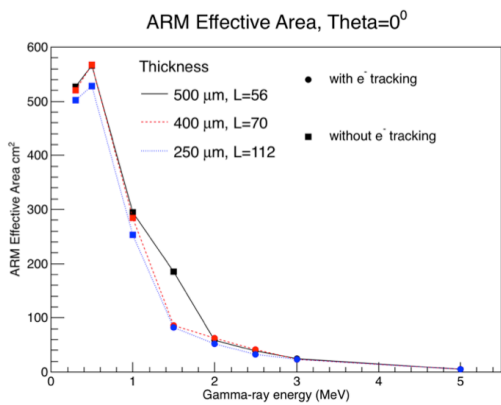
Using the event selection that minimizes the angular resolution we show in the above figure the effective area.
In the left panel, when the number of total radiation lengths is fixed we have obtain the same effective area independent of the simulated geometry.
In the right panel, we have kept the number of layer fix to 56, in this case we observe that, for low energies, for thickness of 250 microns the effective area drop dramatically in comparison with 400 and 500 microns.

Pair production regime

We have studied the angular resolution in the energy range [10, 3000] MeV using pair production events. The angular reconstruction is done using the Kalman 3D filter that was recently implemented in MEGAlib.
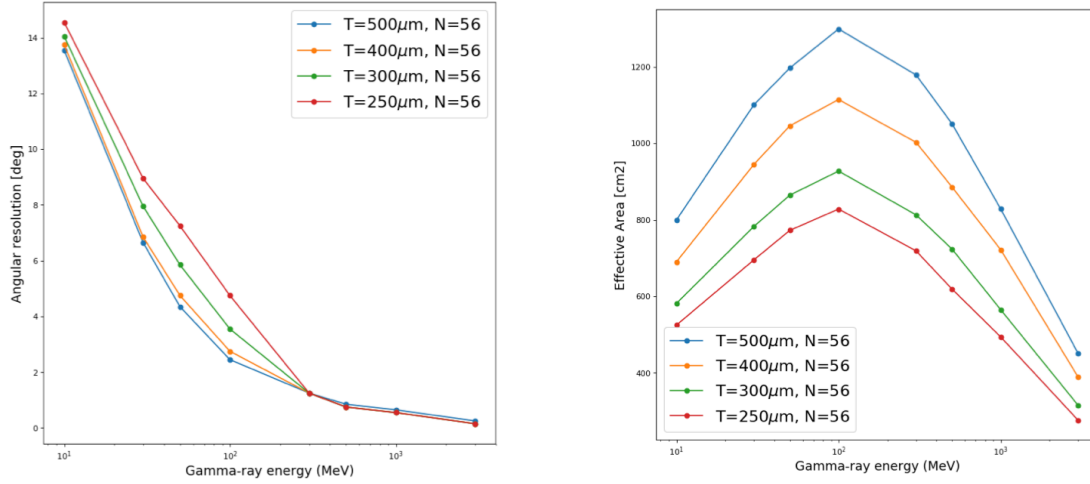
In the above figure we show the results when we have fixed the number of layers to 56. In the left panel, the angular resolution. We can see a dependence on the thickness, the angular resolution gets better when we increase the thickness of the layer.
In the right panel, we show the effective area as a function of the energy. We can see that the effective area decrease as the thickness of the layer get smaller.
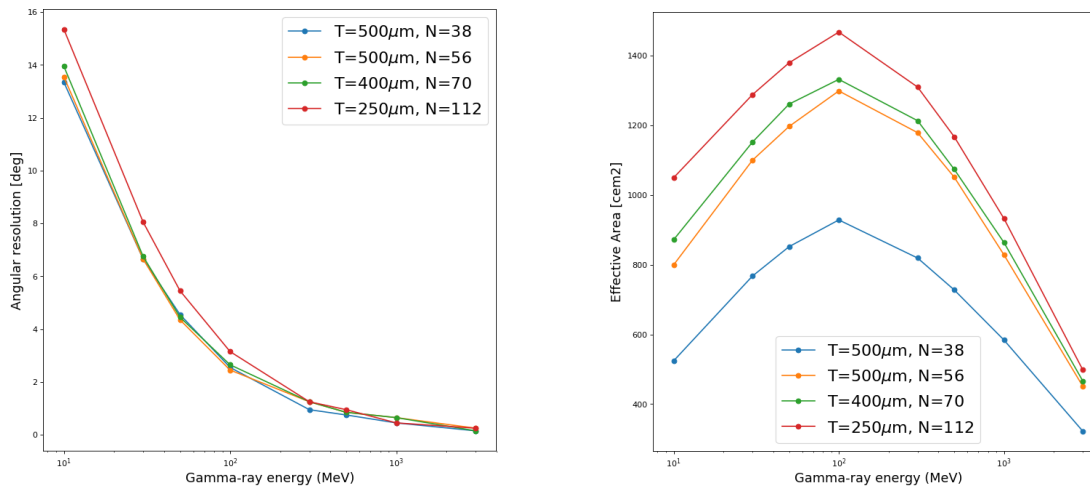
Finally, in the above figure we show the results when the number of interactions length is fixed to $0.3X_o$ (except for 500 microns and 38 layers). In this case, in the left panel we observe that the angular resolution is the same independent of the thickness. In the right panels, we show the effective area that slowly increase when the thickness decreases.

Conclusions

We have simulated different geometries for the eASTROGAM silicon tracker using MEGAlib framework.
We have studied the Compton and Pair production regime by simulates different energies range from 0.3 to 5 MeV for Compton and 10 MeV to 3000 MeV for the pair production.

In the Compton regime we have found that the energy resolution do not depends on the simulate geometry.

For the angular resolution we have to make an event selection between reconstructed events w/o electron tracking to obtain the best possible resolution. After the selection the angular resolution is independent of the geometry. We have found difference in the effective area when the number of interactions lengths is smaller than $0.3X_0$.

In the pair production regime the angular resolution is independent of the geometry when the number of interactions lengths is fixed than $0.3X_0$. We have found some dependence with the thickness when we have fixed the number of layers. We have obtained a better resolution when we increase the number of layers.

Our main conclusion given the results obtain from the different tracker geometries is that the base simulation with a thickness of 500 microns and 56 layers is already an optimize geometry for eASTROGAM.

TO BE DONE.
Check the resolution when we change the pitch from 240 microns to 480 microns…

FUTURE GAMMA-RAY MISSIONS' POLARIMETRIC PROSPECTS

A. F. V. Cortez[1,2], R. M. Curado da Silva[1,2], G. Rodriguez[3], P. Cumani[4,5], A. Morselli[3], M. Hernanz[4], V. Tatischeff[5], J. M. Maia[1,6], P. Von Ballmos[7], A. Zoglauer[8]

[1]*Laboratório de Instrumentação e Física Experimental de Partículas, Coimbra, Portugal*
[2]*Department of Physics, University of Coimbra, Coimbra, Portugal*
[3] *INFN Roma Tor Vergata, via della Ricerca Scientifica 1, I-00133 Roma, Italy*
[4] *ICE-CSIC/IEEC, Campus UAB, 08193 Bellaterra, Barcelona, Spain*
[5] *CSNSM, IN2P3-CNRS and Univ Paris-Sud, F-91405 Orsay Cedex, France*
[6]*Department of Physics, University of Beira-Interior, Covilhã, Portugal*
[7]*IRAP, 9, av. du Colonel-Roche, Toulouse 31028, France*
[8]*Space Sciences Laboratory, University of California, Berkeley, California 94720, USA*

High-energy astrophysics polarimetry may greatly benefit from e-ASTROGAM (enhanced ASTROGAM) mission proposal legacy or from future AMEGO (All-sky Medium Energy Gamma-ray Observatory) proposal, since so far limited polarimetric measurements were performed in this domain by instruments that were not designed neither optimized for polarimetry. Gamma-ray source emissions have been studied almost exclusively through spectral and timing analysis of the measured fluxes and by using imaging techniques based on coded-mask cameras or telescopes equipped with high efficiency focal plane detectors. Polarization measurements will increase the number of observational parameters of high-energy sources by two: the polarization angle and the level of linear polarization. Celestial sources polarimetric analysis can provide important information about the geometry, the magnetic field, the composition and the emission mechanisms. Polarized emissions are expected in a wide variety of gamma-ray sources such as pulsars, solar flares, active galactic nuclei, galactic black-holes and gamma-ray bursts [1].
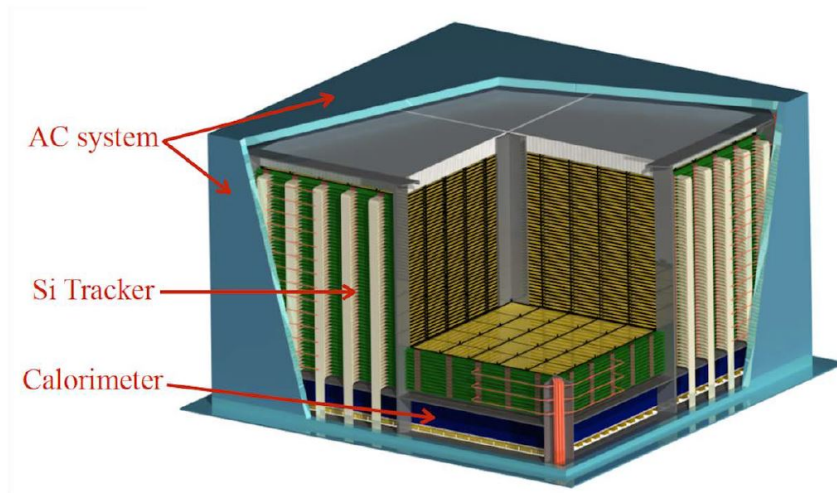

Fig. 1. The e-ASTROGAM scientific payload, composed by the Silicon Tracker, the Calorimeter and the Anticoincidence system [2].
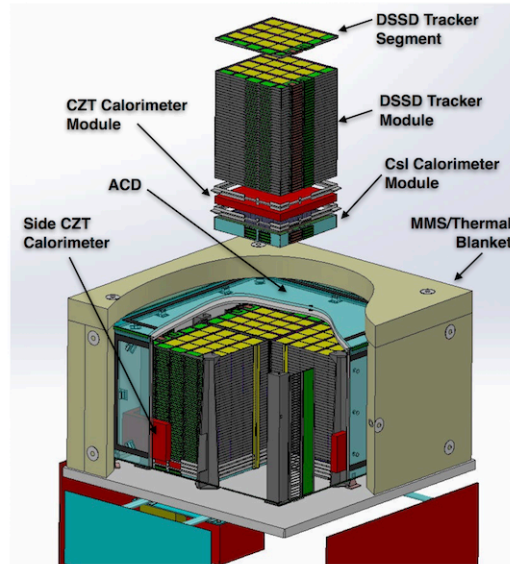
Fig. 2. AMEGO scientific payload.

These mission cocepts share design similitudes based on Silicon trackers, CsI calorimeters, however AMEGO includes a CZT calorimeter mode and a CZT anticoincidence system while e-ASTROGAM is composed by a plastic scintillator anticoincidence (Fig. 1). e-ASTROGAM operates in the 0.3 MeV up to 3 GeV energy band and AMEGO between 0.2 MeV and 10 GeV. The Compton (up to ~2 MeV) polarimetric potential of both mission proposals was analyzed by mass model simulations using MEGAlib simulation tools [3], for different tracker, calorimeter and anticoincidence system configurations (x, y and z dimensions, number of detection elements, etc.) as well as detection units' types (scintillators and semiconductors), within the mission mass and power margins (Fig. 2). Different background levels were simulated for different alternative orbits and main gamma-ray sources were modelized on- and off-axis. Partial (tracker, calorimeter and anti-coincidence system) and overall polarization modulation factor was calculated as well as Minimum Detectable Polarization for each source within the mission time frame.
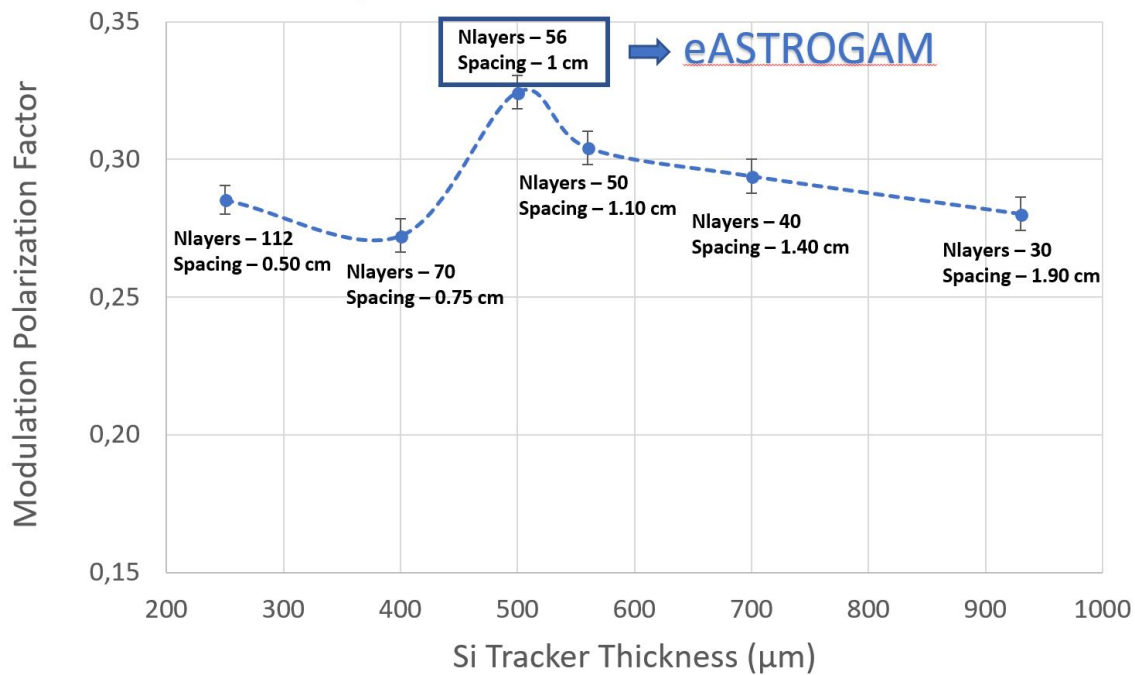
Fig. 3 – e-ASTROGAM tracker modulation polarization factor for different number of layers and spacing configurations.

The best overall configuration for Compton polarimetry will be determined and analysed considering the mission limits and will be used as input for future missions' configuration that should result from the trade-off between all the scientific measurements (spectroscopy, imaging, time-variability, polarimetry, etc.) mission objectives.

AMEGO vs. e-ASTROGAM

The polarimetric performances of both mission proposals (AMEGO and e-ASTROGAM) will be compared under the same measurement environment simulation conditions (background, emission source, pointing, etc.). Although, the main configuration concepts of both missions are relatively similar, the calculated polarimetric sensitivity obtained for each mission (Fig. ???) will be analysed and discussed taking into account the most relevant design differences: Si tracker DSSD arrays (5x5 for e-ASTROGAM and 4x4 for AMEGO) and number of layers, the calorimeter composition (CsI and CZT+CsI for AMEGO) and the anticoincidence composition and design.
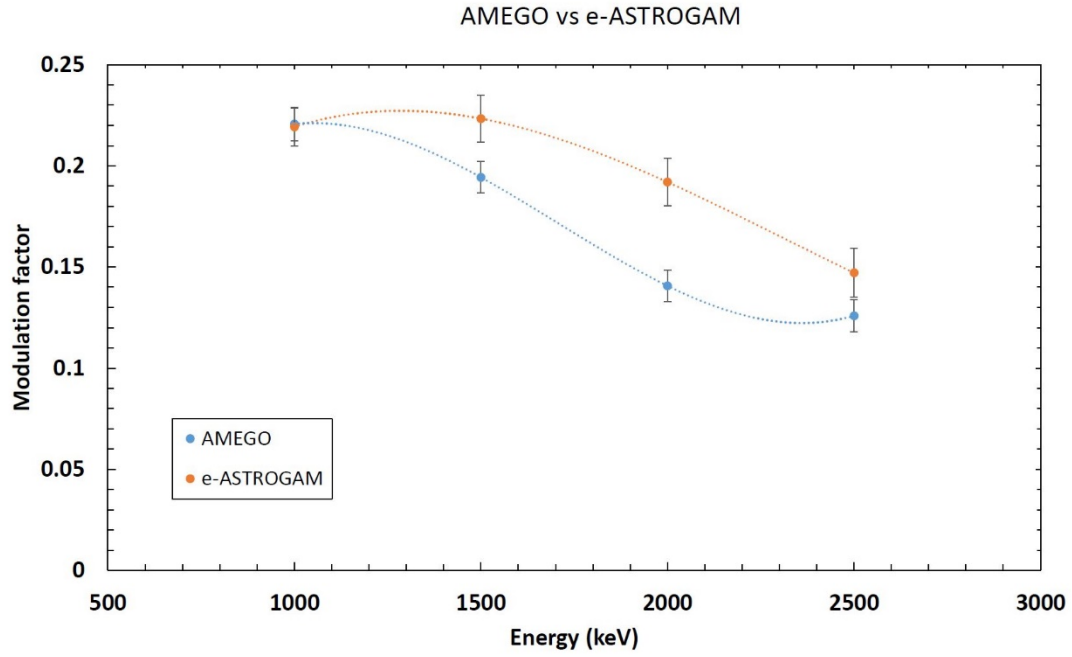
Fig. 4 – AMEGO vs e-ASTROGAM polarization modulation for different monochromatic point sources between 1 MeV and 2.5 MeV.
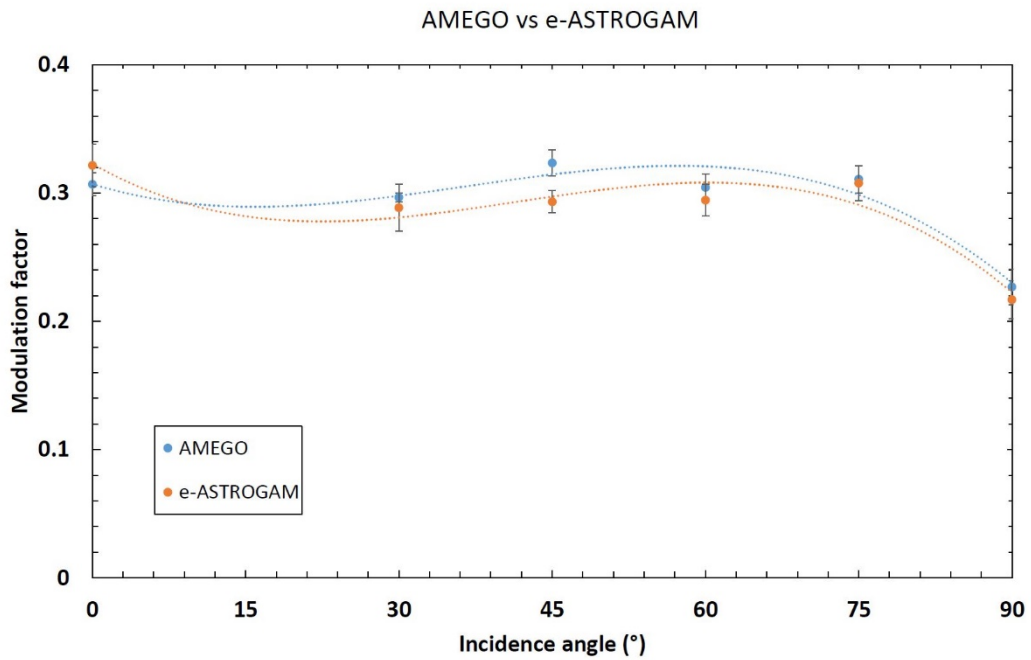

Fig. 4 – AMEGO vs e-ASTROGAM polarization modulation for different source flux incidence angles, where the source is a Crab like spectrum within the 0.2 up to 2 MeV energy range.

The main conclusions of these results analysis will be discussed, in order to optimize enhanced future medium energy gamma-ray observatories and in particular particular its potential to perform advanced polarimetric measurements.

[1] Lei et al. Compton polarimetry in gamma-ray astronomy, Space Sci. Rev., 82, 309-388 (1997).

[2] De Angelis et al., The e-ASTROGAM mission: Exploring the extreme Universe with gamma rays in the MeV - GeV range, Exp Astron., 2017, 44, 1, 25

[3] Zoglauer et al., MEGAlib – The Medium Energy Gamma-ray Astronomy Library, New Astronomy Reviews 50 (2006) 629–632.

<u>team 2 : Ge-Based Compton Telescopes (ASCI)</u>

IRAP Toulouse : P. von Ballmoos, P. Jean
University College Dublin : L. Hanlon
Space Sciences Laboratory, UC Berkeley : S. Boggs, A. Zoglauer

Background study of Germanium based Compton telescopes

AHEAD report

first draft - October, 2018.

A. Gostojic[a,*], P. von Ballmoos[a], P. Jean[a], L. Hanlon[b]

[a] *IRAP, Univ. Paul Sabatier, CNRS, CNES, Toulouse, France*
[b] *UCD, Univ. College Dublin, Dublin 4, Ireland*

1. Introduction

To be added (TBA)

2. 2016 COSI flight data

To begin with, I will introduce the two main COSI data sources used in the following background analysis. These comprise of the data recorded during the 2016 COSI campaign which lasted for approximately 47 days, starting on 17th of May, 2016 and ending on 2nd of July, 2016. Important to note is that the times and dates are given in GMT zone and are direct transformation of the UNIX time format used and recorded on board the COSI instrument. The data is partially preanalyzed by the Berkley team after the extraction of the raw data from the detectors and was repacked in MEGAlib format, which will be explained in the following Section 1. The two main data groups are: 1 – Events recorded by the array of Ge main

*Corresponding author
Email address:* `aleksandar.gostojic@irap.omp.eu` (A. Gostojic)

detectors; 2 – Data recorded by the Anti-Coincidence Shield, CsI detectors,
as well as flight data regarding the location of the instrument in the Earths
atmosphere.

2.1. Data from the Ge detectors

The main data obtained from the COSI's core Ge detectors and preanalyzed
by the team at UC Berkley comprises of 47 files in .tra format. Each file
corresponds to one day of flight, starting from the first timestamp: Tuesday,
May 17., 2016. 12:00:14.473 AM GMT and finishing with the last timestamp
corresponding to Saturday, July 2., 2016. 4:47:01.242 PM.

The .tra format corresponds to MEGAlib's file format, and as mentioned
the data within the files is sorted according to MEGAlib's notation. A
snippet of such COSI's detected events is represented on Figure1.

Additional information for each of the 47 files tells us that approximately
one third are Compton events, two thirds are Photoelectric events and only
several percent of the data are Unknown. While the total number of detected
events varies from day to day, it is still in the order of $1-20 \times 10^6$ events which
provides more then satisfactory statistics for the analysis. More detailed
explanation of the MEGAlib's notation and the abbreviations shown on the
Fig. 1 is given in the short listing below:

SE – Start Event: beginning of the next event

ET – Event Type: shows the type of the recorded event, in our case: CO
for Compton, PE for photoelectric and UN for unknown events.

ID – Identification: number of the event within a given file

2

```
SE
ET CO
ID 8
TI 1465689986.766764200
GX 175.252 -2.87027
GZ 262.933 38.9067
HX -57.3394 0.645507
HZ 86.129 89.1967
CC AS -14.190995 -101.39828 237.33937 -0.64550709 -0.47818008 1465689989.000000000
CC NStripHits 5
SQ 3
CT 0.0260454 0.43921
TL 1
TE 911.556
CE 539.655 1.63028    911.556 1.28952
CD 0.3816 -8.62935 -4.35575    0.057735 0.057735 0.0291611    0.3816 -8.42935 -4.35575
   0.057735 0.057735 0.0291611    0 0 0    0 0 0
LA 0.2
SE
ET PH
ID 9
TI 1465689987.001218400
GX 175.252 -2.87027
GZ 262.933 38.9067
HX -57.3394 0.645507
HZ 86.129 89.1967
CC AS -14.190995 -101.39828 237.33937 -0.64550709 -0.47818008 1465689989.000000000
CC NStripHits 2
PE 171.299
PP -6.2184 7.22935 -5.321
PW 0
SE
ET UN
ID 10
TI 1465689987.043962300
```

Figure 1: A snippet taken from one of the COSI's data files. Preanalyzed by UCB team using MEGAlib based software. Three main types of events are noted in "ET" columns: CO - for Compton events, PE - for photoelectric (single interaction) events and UN - for unknown, or events which are not identified during the reconstruction. See text and MEGAlib's documentation for full explanation of the data and notations.

TI – Time: time of the event, expressed in Unix Time format in [sec]

GX/GZ – Galactic coordinates of the direction of X/Z axis of the instrument

CE – Compton Energy: energy in [keV] with uncertainties for the two first Compton interactions within the detector.

CD – Compton Direction: positions in 3D: X,Y,Z in [cm], with attributed uncertainties for the first two Compton interactions within the detector.

PE/PP – Photoelectric Energy and Position: Energy in [keV] and position in 3D: X,Y,Z in [cm] for the photoelectric (single interaction) events.

It is important to note that we explain only the events we directly used in the analysis of the background, for the full details and more information refer to [1]. In addition, further in the text we will keep the applied shortcuts for Compton (CO) and photoelectric (single or PE) events.

2.2. ACS - Anti-Coincidence Shield rates and the telemetry data

Second vital source of information regarding COSI's flight are the readings from the Anti-Coincidence Shield (ACS) such as the recorded shield rates, as well as, the sets of geolocation and altitude readings corresponding to that shield rate. Both are contained in a data file, which uses a given nomenclature for the contained data sets:

Unix_Time (ut) – Time of the recorded input in [sec] expressed with Unix Time format.

Counts (cts) – Number of counts (events) recorded by the ACS i.e. shield rate.

Time/100ns (Δt) – Length of the time window for recording each event, in [sec] .

Livetime_fraction (lv) - Lifetime of the detector, expressed as fraction in percent [%].

Latitude/Longitude (lat,lon) – Are the geographic coordinates, given in [deg].

4

Altitude (Alt) – COSI's altitude at a given time in [m].

We have again done the repacking into, easier to handle, python .npz files, doing a quick calculation of the ACS count rate ACS_{rate} and its error $\sigma(ACS_{rate})$. Secondly, we reformatting the time, in a way that the we defined the beginning i.e. $time = 0\,sec$ to corresponds to the start of COSI's flight, thus counting each subsequent second as 1st, 2nd, ... second of flight time. These calculations are given by equations $1 - 3$:

$$ACS_{rate} = \frac{c}{\Delta t \times 10^{-7}} \times \frac{100.}{lv} \tag{1}$$

$$\sigma(ACS_{rate}) = \frac{\sqrt{c}}{\Delta t \times 10^{-7}} \times \frac{100.}{lv} \tag{2}$$

$$t' = t - t_{START} \tag{3}$$

where: t' is the reformatted time and $t_{START} = 1463441719.0$ is the launch date in seconds in Unix Time format. In such a way we have enabled easy access through Python NumPy's .npz file to the following information: ACS rate, detectors dead time, time and altitude and geolocation stamps.

3. First analysis and data selection and rejection criteria

We have developed several python scripts to access and analyse all the data available. Here, we briefly present the general logic (trend) used in all further analysis. For the purpose of reducing the time consumption and easier handling of the data, our first step was to reformat all the available data strings (detected events, ACS etc.) into average values for each data type per certain time interval. After experimenting with several options

5

we finally decided to settle on an interval of $\Delta t = 10\,[min]$. This lead to dividing the total flight time of $\approx 47\,days$ to 6676 intervals of 10 minutes. Therefore, every data point presented in the graphs thorough the rest of this report will be in this format. Furthermore, we will be referring to the data points by number e.g. 100th data point, which would be the average at 100th 10 minute time interval of the flight time. In simple terms one point will represent the flight time interval of $(100 - 101) \times 10$ minutes of flight time. In such manner we present on Figures 2 and 3 extracted and averaged values for the recorded altitude and latitude and longitude over the whole duration of the COSI's flight.
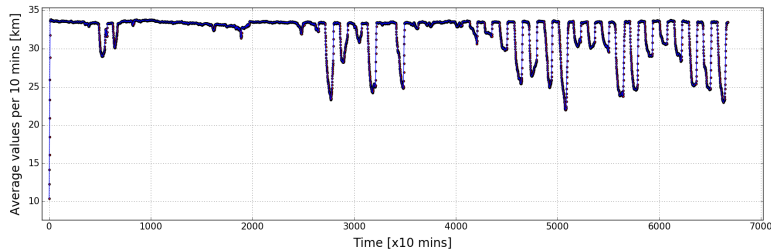

Figure 2: COSI altitude profile for the whole duration of the flight. Each point represents an average value of altitude in [km] for the period of 10 minutes of the flight. The maximum altitude is between 33 and 34 kilometeres. Noted altitude variations, especially in the second half of the flight are majorly caused by the day-night cycle during the flight.

Additionally, a more intuitive representation of the COSI's flight path is given by the illustration on the Figure 4

3.1. ACS and 511 keV count rates

Continuing with the analysis, we accessed the Ge detectors data, firstly making a selection between Compton and photoelectric events. Then for each of
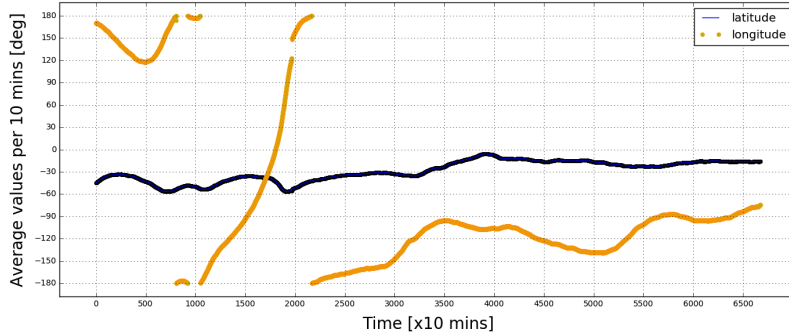
6

Figure 3: Geographical latitude (dark blue data) and longitude (yellow data), expressed as average values in [deg] for each 10 minutes of the flight time.

these events, as the first analysis necessities, we selected interaction locations and deposited energy for each type of events. In the case of Compton events this involves two interaction positions and two deposited energies, which are defined by two Compton scatters of the detected gamma-ray within the layers of Ge detectors. This allowed us to reconstruct the energy spectra for the desired type of events.

Shown, on Fig. 5 is the energy spectrum obtained by selecting only Compton events during 24h of flight time or for one day on 18th of May, 2016. We then proceeded to select the 511 keV line as the first and foremost important basis for the later background analysis. Accordingly we needed to determine the average rate i.e. number of counts per second for any moment or period during the flight time. To obtain the correct 511 keV rate, we applied a simple continuum approximation and subtraction according to the formula given by equation 4. After this, we ere able to calculate the average rate for a specific time period, including the defined (see: Sec. 1)
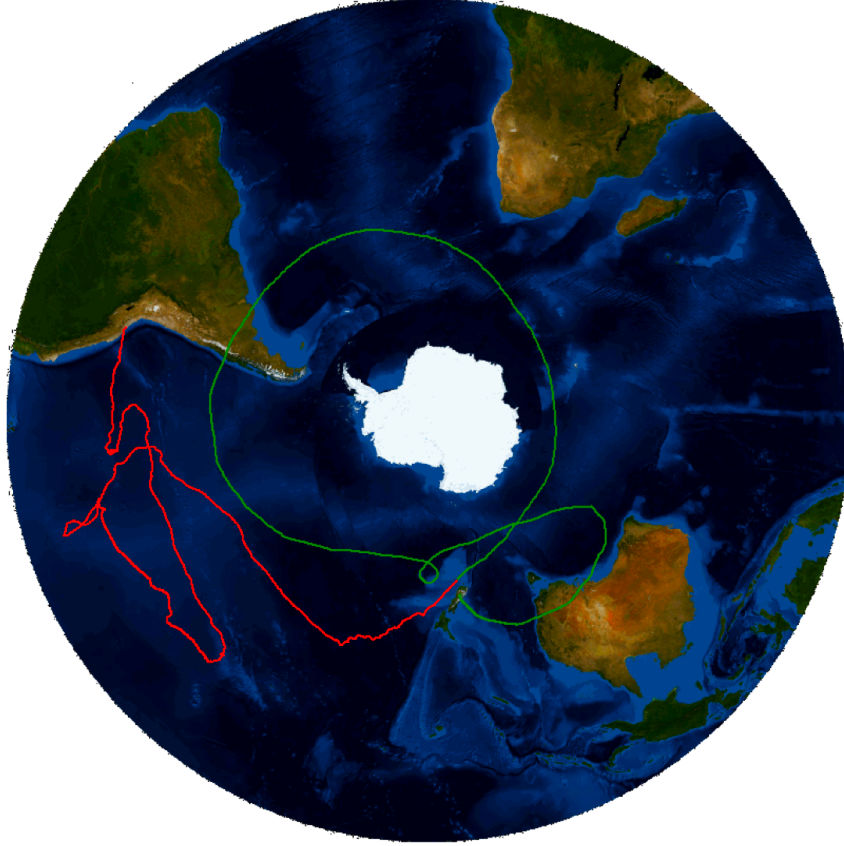
7

Figure 4: Illustration of the COSI's flight path in reference to the Earth. Starting location was at New Zealand on 16th of May, 2016, and after circling the South Pole and traversing the Pacific, COSI landed upon reaching land in South America on 3rd of July, 2016.

average values for each 10 minutes of flight time.

$$R_{511} = rate(e_{b2}, e_{a1}) - \frac{1}{2} \times \left(\frac{rate(e_{b1}, e_{b2})}{e_{b2} - e_{b1}} + \frac{rate(e_{a1}, e_{a2})}{e_{a2} - e_{a1}}\right) \times (e_{a1} - e_{b2}) \ (4)$$

Where $rate(e_1, e_2)$ in [counts/keV], representing the total number of counts
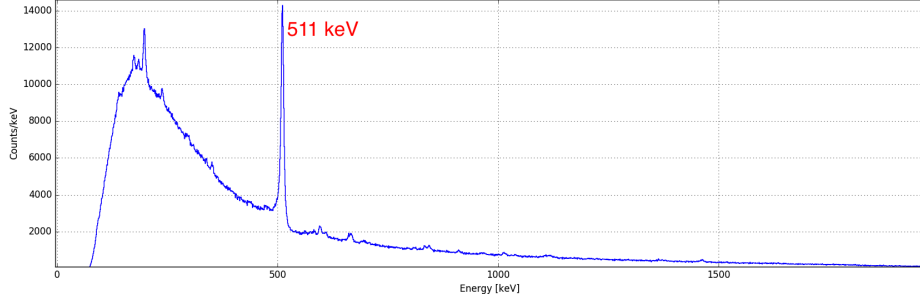
Figure 5: Reconstructed energy spectra corresponding to 18th of May, 2016, obtained by selecting only Compton scattered gamma-rays i.e. Compton events. The 511 keV annihilation line is clearly visible and marked on the histogram.

within the interval between energies e_1 and e_2, is given by the sum 5.

$$rate(e_1, e_2) = \sum_{i \in e_1, e_2} S_i \times \Delta E \tag{5}$$

Where S_i is the total number of counts [count rate per keV] per each histogram bin i within the range between energies e_1 and e_2, and ΔE is the width of the bin within the histogram 5. Combining equations 4 and 5, we basically select an interval $(e_{b2}-e_{a1})$ of $\pm 10 \, keV$ around the $E_\gamma = 511$ keV line, where the starting energy is $e_{b2} = 501 \, keV$ and the end energy $e_{a1} = 521 \, keV$. In a similar way, we are able to define two more intervals, interval before 511 keV line $(e_{b1}-e_{b2})$ and interval after the 511 keV line $(e_{a1}-e_{a2})$ which help us define the continuum. The values of these intervals was tested for $\Delta E = 10, \, 20 \, and \, 40 \, keV$ where we opted to use the intervals of 20 keV i.e. $e_{b1} = 481 \, keV$ and $e_{a2} = 541 \, keV$. The whole method is simplified on Figure .

This method allowed us to calculate the event rates in [cts/sec] for each
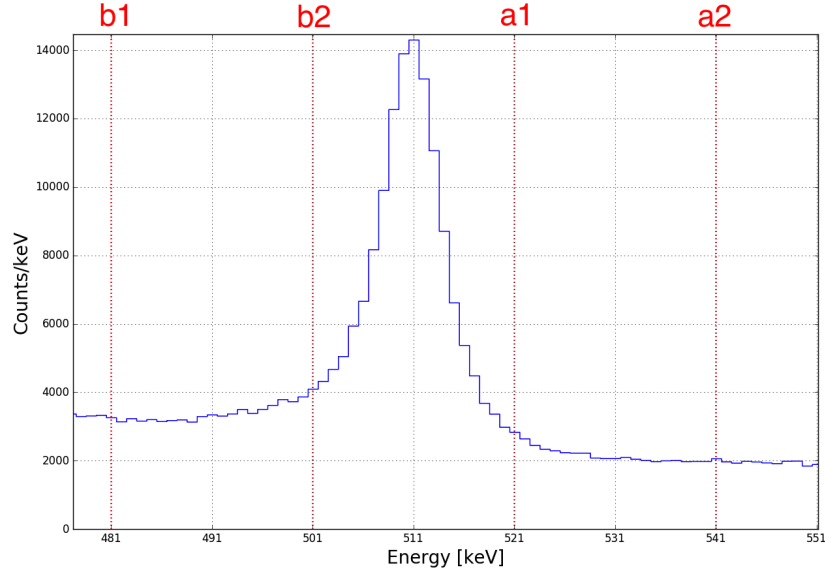
9

Figure 6: Zoomed 511 keV line from the reconstructed energy spectrum of the detected Compton events. The selected energies e_{a1}, e_{a2}, e_{b1} and e_{b1} (discussed in text) are the ranges we used to estimate the number of counts for the 511 keV line, while subtracting the contribution from the continuum eq. 4.

10 minutes of the flight time for the three types of of the available events
135 Compton (CO), photoelectric (PE) and shield rates (ACS). In addition, we calculated the uncertainties for the 511 keV rates as the statistical error of the number of counts, equation 6. These were, in general, in the order of several percent over the whole period of COSI's flight.

$$\sigma(R_{511}) = \sqrt{R_{511}} \tag{6}$$

The analysis algorithm contains a method for timestamps comparison,
140 providing us the ability to combine different files such as detected gamma-

10

ray events with the ACS data, therefore calculating average values for any time periods (e.g. days, hours, 10 minutes), but more importantly it allows us to correct the calculated average count rates for the dead time of the detectors. The used detector lifetimes are shown on the Figure 7, and as seen on the figure apart from several anomalous events indicate detectors dead time of the order of several percent.
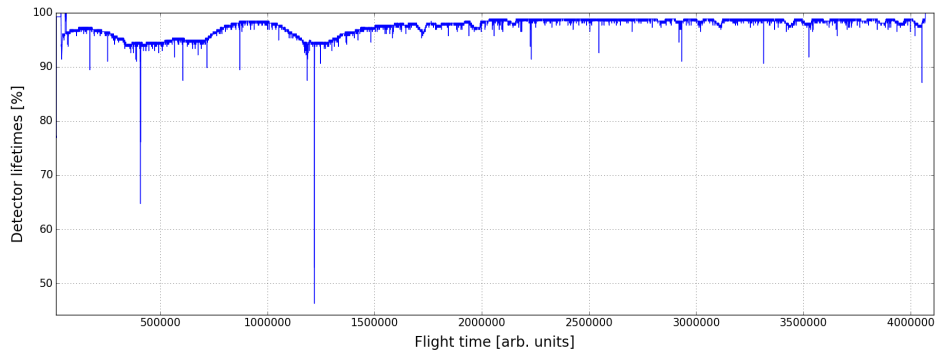

Figure 7: Raw plot of the recorded detector lifetimes over the whole duration of the COSI's flight, illustrating a general trend of low dead times of the order of several percent. The two large jumps correspond to the two recorded DREP events, as discussed later in the text.

After such analysis, we were able to produce the average rates for all of the event types recorded with COSI as well as ACS rates, and proceed to study and compare them. An overall counting rates for $E_\gamma = 511\,keV$, together with the scaled ACS rates is presented on the Figure 8 for the whole duration of the flight.

The overview of the counting rates seen on the above Figure 8 provided us with several insights:

– There seems to be an overall agreement in the trends of the counting
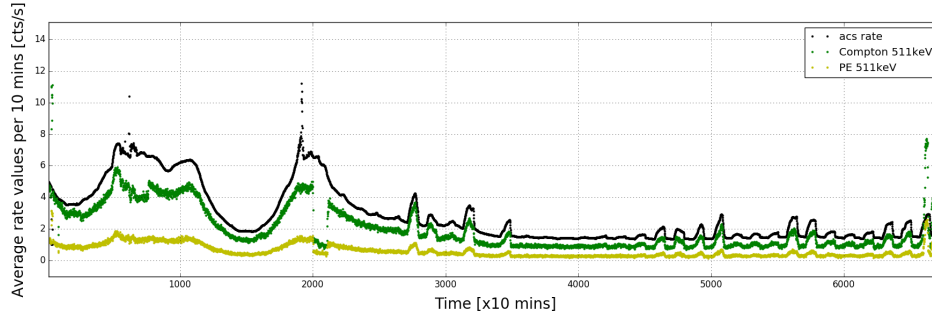
11

Figure 8: Calculated average rates for each 10 minutes of flight time for three types of events: Compton (CO) – green data, photoelectric (single) – yellow data and ACS rate – shown in black and is scaled by a factor of 5000 for the purpose of presentation, with two extreme maxima at $R_{ACS} \approx 180 \times 10^3$ [counts/s] at approximate time of $Time = 616 \times 10\,mins$ (103rd hour of flight), corresponding to the first DREP event and maximum $R_{ACS} \approx 200 \times 10^3$ [counts/s] at approximately $Time = 1916 \times 10\,mins$ (320th hour of flight), corresponding to second DREP event.

rates for the 511 keV line reconstructed from detected Compton and photoelectric events, in addition both seem to agree with the overall ACS count rates e.g. night-day oscillations starting around $Time = 3000$.

– The two above mentioned Duskside Relativistic Electron Precipitation (DREP) events – are the two recorded events caused by the precipitation of the electrons from the outer radiation belt, which caused the two maxima in the ACS count rate, as is expected in such cases.

– We, however, noted two distinct discrepancies between the 511 keV and ACS rates. Two intervals where the rate seems to decrease in a "step" manner, where however the shield rate remains smooth. First can be seen at $Time \approx 650$ just after the first DREP event. Second

12

starts just after $Time = 2000$.

– Finally, there are several random irregular events, such as also ascend and descend data, all of which are discussed in the next section.

3.2. Data rejection criteria

We continue the discussion of several noted anomalies regarding the calculated average rates of events over the flight time, as they effected the data rejection and cuts which we performed before going further into the background analysis. Directly related to the observations regarding the plot on Fig. 8 we have omitted multiple intervals from the further analysis. The following list (related to the our 10 minute average point system) contains all of the rejected events and is valid for all the plots and results (if not stated differently) presented in the report further on:

1. The ascend i.e. the beginning of flight has 0–12 points removed which corresponds to 120 minutes of flight time.

2. A period, corresponding to data points 31–42nd (310th until 420th minute of flight time) was removed due to a verified problem with high voltage (HV) of the ACS shield. It is clearly seen on the Fig. 9

3. A rather long period between 674–775th data points was also removed. The noted decrease in the CO and PE data is due to instrumental error, where three out of twelve Ge detectors were off. This was confirmed with the Berkley team as well as the COSI's flight log and our own analysis, e.g. see Figure 12

4. Another larger portion of data excluded from the analysis are within the range 2000–2117th data point. This corresponds the period following a massive problem with the cryostat on 30th of May, 2016. (GMT)

13

In fact we have no usable data for the 30th of May after 4:13:20 PM (GMT). Following this period, starting from approximately 05:30:36 PM on 31st of May, 2016. (GMT) COSI was operating without two out of three rows of detectors i.e. with only four out of twelve Ge strips, which caused a noticeable decrease in the recorded CO and PE 511 keV count rates. These problems were confirmed with Berkley group and are also noted on our own analysis, again refer to the Figure 12.

5. Finally, the last 77 points, corresponding to range 6600-6677th data point, which represents the descent of the balloon have been removed as well. In a similar way as the ascent, they present an unstable period of the flight, giving anomalous data readings due to rapid altitude changes or exposure to the high radioactivity while passing through the Pfotzer maximum – an altitude region within the atmosphere where the external radiation is at its highest.
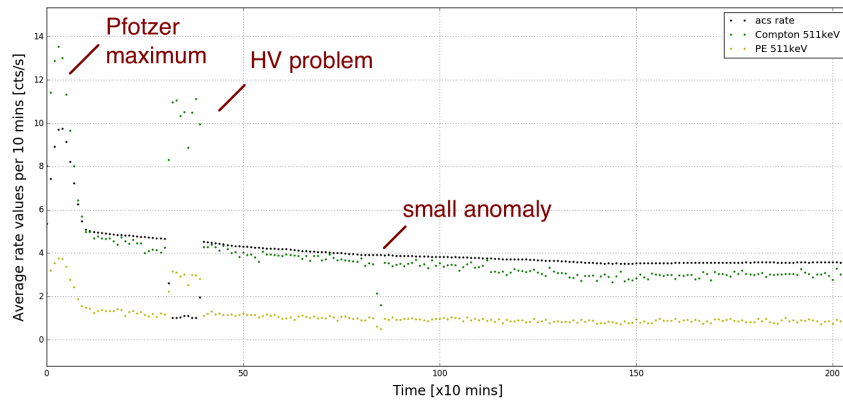

Figure 9: First 30 hours of flight time, with CO and PE 511 keV rates in green and yellow respectively, and scaled ACS rate $[\times 5 \times 10^{-3}]$ in black points. The plot is showing COSI's ascend and passage through the Pfotzer maximum, as well as two minor instrumental problems, all of which are noted on the plot.

14

After the successful selection of the "good" data we proceeded to study several correlations (ratios) between the calculated rates for the three data sets (CO,PE,ACS). These are presented on Figures10 and 11
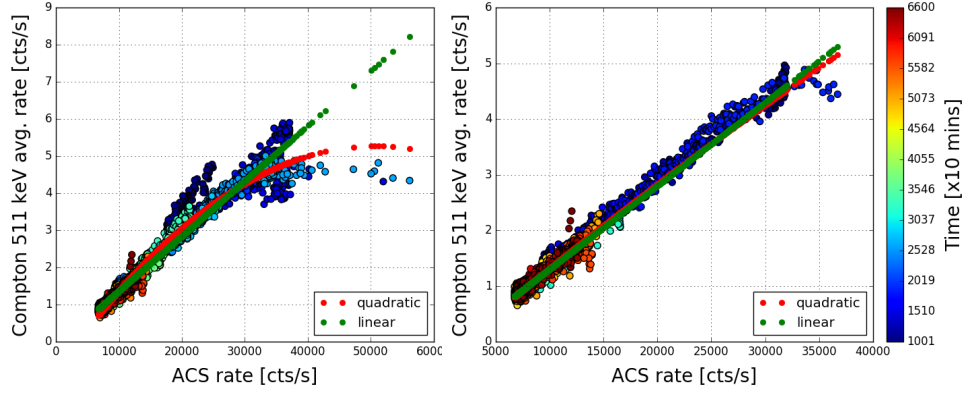

Figure 10: **Left** – Ratio over total flight time, between 511 keV line rate from Compton events and ACS count rate. As previously described, the rates are given as average values in [cts/sec] for each 10 minutes of flight time. The relation was fitted using linear and quadratic fits, equations 7. **Right** – The same as on the left plot with stronger data rejection, fitted in the same manner with linear and quadratic fits given by equations 8.

$$Lin: \quad R_{511} = 0.11 + 1.46 \times 10^{-4} \times R_{ACS}$$
$$Quad: \; R_{511} = -0.77 + 2.39 \times 10^{-4} \times R_{ACS} - 2.36 \times 10^{-9} \times R_{ACS}^2 \tag{7}$$

210

where: R_{511} and R_{ACS} are Compton 511 keV line and ACS rates in [cts/s] respectively, and the residuals of the linear and quadratic fits are $< Residual > \approx 7\%$.

$$Lin': \quad R_{511} = -0.19 + 1.49 \times 10^{-4} \times R_{ACS}$$
$$Quad': \; R_{511} = -0.29 + 1.65 \times 10^{-4} \times R_{ACS} - 0.47 \times 10^{-9} \times R_{ACS}^2 \tag{8}$$

15

215 Where again: R_{511} and R_{ACS} are Compton 511 keV line and ACS rates in [cts/s] respectively, and the residuals of the linear and quadratic fits with stronger data rejection are $< Residual > \approx 5.5\%$.
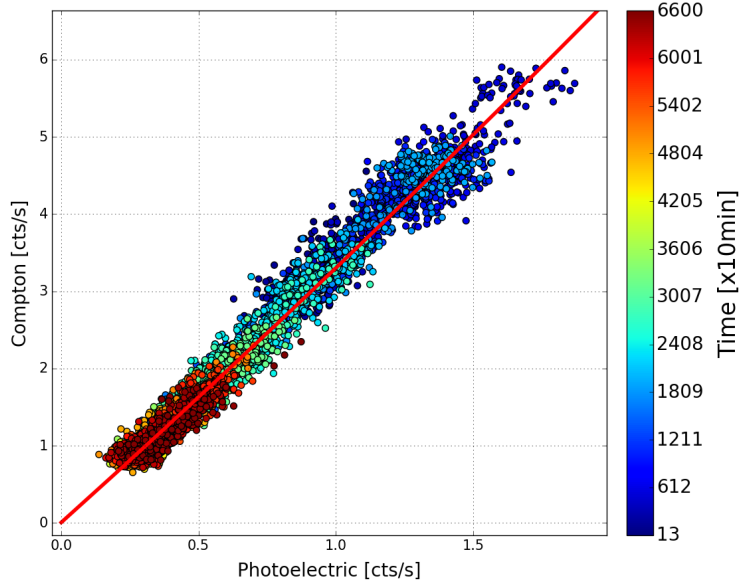

Figure 11: Ratio between 511 keV line rates for Compton (y axis), and photoelectric (x axis) events. Averaged for 10 minutes of flight time, with color representing the flight time. The quadratic fit (red line) is given with equation 9.

$$R_{511}^{CO} = 6.863 \times 10^{-3} + 3.191 \times R_{511}^{PE} + 0.102 \times (R_{511}^{PE})^2 \tag{9}$$

Where, R_{511}^{CO} and R_{511}^{PE} are rates in [counts/s] of the selected 511 keV line

220 for the Compton and photoelectric events, respectively, with the quadratic fit having average residuals in the order of $< residual > \approx 8\%$.

16

3.3. Interaction locations and detectors ON/OFF periods

Studying the data so far, specifically plot representing rations Fig. 10 along

225 with the COSI's flight log, and referring to the list of problems (points 3.
and 4.) in Sec. 2.2 we conducted a brief study of the overall COSI's main
detectors performance. In general the geometry of the germanium detectors,
distributed into three layers with four detectors each, allowed us to spatially
distinguish (redistribute) the recorded event hit locations using Compton or

230 photoelectric data. In such way we were able to distinguish a timeline of
several configurations during the flight time, which correspond to different
number of detectors being active (ON) or having a malfunction or being
shut down (OFF). One of such illustrations is given on the Figure 12.

A brief study of in regard with the Figure 12 and its caption shows that

235 indeed we can divide the flight into four separate "configurations" depending
on the number of active detectors:

    I Starting from launch until $Time = 113 \times 10\,[mins]$ we have all 12
       detectors working (All configuration).

    II In the period $Time = (113 - 255) \times 10\,[mins]$, one detector is not

240   working (-1 or 1 OFF configuration).

    III Within two periods $Time = (255 - 627) \times 10\,[mins]$ and $Time = (762 -$
       $2930) \times 10\,[mins]$ two detectors were down (-2 or 2 OFF).

    IV Finally, within the period $Time = (627 - 762) \times 10\,[mins]$ and from
       $Time = 2930 \times 10\,[mins]$ until the end of flight, three detectors were

245   malfunctioning (-3 or 3 OFF).

Furthermore, we can easily recognise the period where two detector layers were off after a cryostat malfunction, referring to Figures 8 and 12, within
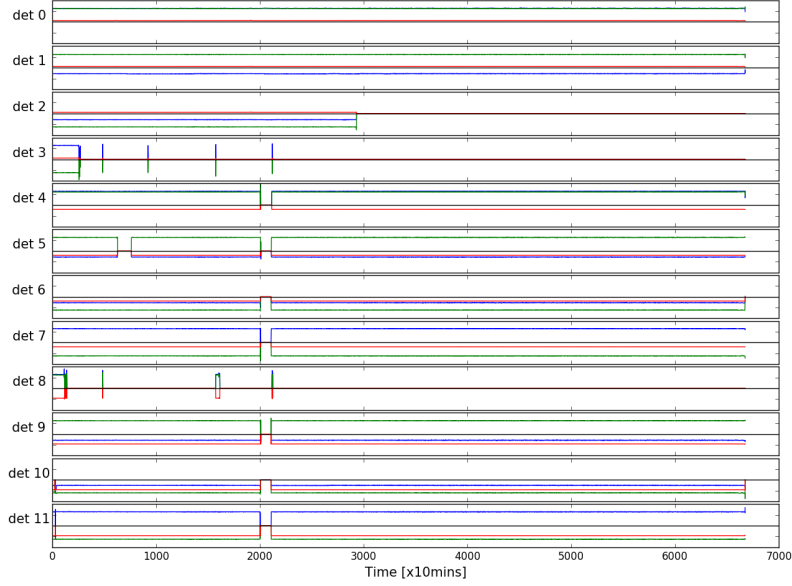
17

Figure 12: The figure is intended for illustrative purposes of the different ON/OFF periods for different detectors within the COSI's configuration. Detectors noted 0–3 are from the top layer, 4–7 middle layer and 8–11 bottom layer. With blue,green and red colors denoting average values for each 10 minutes of the three coordinates (X,Y,Z) of the reconstructed position of the first gamma-rays interaction with a Ge detector. We used recorded Compton events. Middle line in black, in each of the 12 plots (bars), represents a zero value, thus if any of the colored lines (X,Y,Z values) are coinciding with the zero value, means that detector is not recording any events during such periods.

time marks $Time = (2000 - 2117) \times 10\,[mins]$. Another illustration of the hit locations within the ON/OFF detectors is given on Figure 13. Such plots were used as additional confirmation and study tool to help distinguish the ON/OFF periods for different detectors.
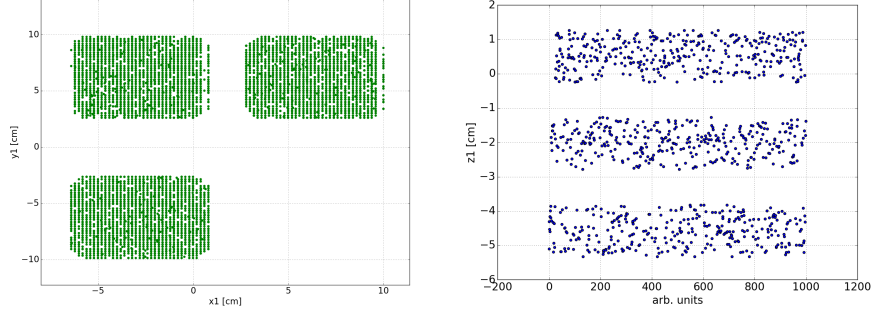
18

Figure 13: **Left** – Distribution of the first Compton interaction locations, in terms of X,Y [cm] coordinates within the reference system defined by COSI's dimensions (size). Presented, are the first 10^4 events recorded on the 22nd of May, 2016 (GMT). The layer of the Ge detectors (one out of three detector planes) is the top most one, closest to the entrance window of COSI. Note that only three groupings are shown, corresponding to three working Ge detectors and one detector OFF, within the given layer at that period of the flight. Even more, it is possible to note the individual strips within each detector. **Right** – Simplified interpretation of the three layers of Ge detectors within COSI, according to depth-of-interaction (DOI). Noted z1 value in [cm] shows the thickness of Ge detectors within each layer and distances between active detectors in reconstructed COSI geometry.

4. Cut-off rigidity

Cut-off rigidity estimation was one of the mayor requirements for achieving a valid background model. Additionally, it helps us further in the goal of simulating a Ge detectors based satellite outside of the Earths atmosphere. To simply estimate the cut-off rigidity, we applied the method from [2]. However, this method uses what is known as "Shifted dipole approximation" of the Earth's magnetic field, where the field is approximated by a dipole whose center with the coordinates (λ_d, φ_d) is shifted by δ from the center of the Earth. This approximation is time dependent, meaning that the dipoles coordinates are non-stop evolving, thus we had to calculate the

19

correct values for the year 2016. and update the method [2], which provides values for the year 1998.

4.1. Shifted dipole approximation

If we start from the method explained in [?], the magnetic field, of a dipole representing the Earth's magnetic field, is given by $B = -\nabla V$, where the potential V takes form as in equation 10.

$$V(r, \theta, \phi) = R_E \sum_{n=1}^{\infty} \sum_{m=0}^{\infty} \left(\frac{R_E}{r}\right)^{n+1} (g_n^m \cos m\phi + h_n^m \sin m\phi) P_n^m(\cos \theta) \quad (10)$$

Where: R_E is Earths radius, (r, θ, ϕ) are the spherical coordinates related to the Earth's center, $P_n^m \cos \theta$ are quasi-Schmidt normalised associated Legendre polynomials and g_n^m and h_n^m are the Gauss coefficients of degree n and order m. This expansion is an infinite series, but in practice it is calculated up to $n = 10$ or $n = 12$.

In addition, the International Association for Geomagnetism and Aeronomy (IAGA) is experimentally determining and within it's International Geomagnetic Reference Field (IGRF), providing values for these Gauss coefficients. These publications are periodically updated for different epochs (e.g. 5 years) with the values of coefficients given as definitive for the past years and, as approximative values, for the several years in the future until the next publication.

In order to find the needed Gauss coefficients for the year 2016, we consulted the IGRF 12th generation of coefficients [3]. The required coefficients can be found in the Table 3 of this publication, and since the IGRF calculated the coefficients for 5 year "epochs", we used values provided for the

year 2015 and added a 1 year approximation which represents the predicted values for the year 2016 according to the model. Now, having obtained the coefficients we returned to calculations provided by [?], and began by defining the dimensionless coordinates xi,eta and zeta (ξ, η, ζ) through the coefficients, as shown in equations 11.

$$\xi = \frac{(L_0 - g_1^0 \times E)}{3B_0^2}$$
$$\eta = \frac{(L_1 - g_1^1 \times E)}{3B_0^2}$$
$$\zeta = \frac{(L_2 - h_1^1 \times E)}{3B_0^2} \tag{11}$$
$$where :$$
$$B_0 = (g_1^0)^2 + (g_1^1)^2 + (h_1^1)^2$$

Next, we calculate L_0, L_1, L_2 and E as shown in the set of equations 12.

$$L_0 = 2g_1^0 g_2^0 + \sqrt{3}(g_1^1 g_2^1 + h_1^1 h_2^1)$$
$$L_1 = -g_1^1 g_2^0 + \sqrt{3}(g_1^0 g_2^1 + g_1^1 g_2^2 + h_1^1 h_2^2)$$
$$L_2 = -h_1^1 g_2^0 + \sqrt{3}(g_1^0 g_2^1 - h_1^1 g_2^2 + g_1^1 h_2^2) \tag{12}$$
$$E = \frac{L_0 g_1^0 + L_1 g_1^1 + L_2 h_1^1}{4B_0^2}$$

From here, the distance of the magnetic dipole center from the center of the earth δ is given by equation 13:

$$\delta = R_E \times \sqrt{\xi^2 + \eta^2 + \zeta^2} = 579.3686\,[km] \tag{13}$$

Where, $R_E = 6371.2km$ is Earths radius. Now, we are able to express the

dipole shift in Cartesian coordinates (x,y,z) given in kilometeres by the sets of equations 14.

$$
\begin{aligned}
x &= R_E \times \xi \\
y &= R_E \times \eta \\
z &= R_E \times \zeta
\end{aligned}
\tag{14}
$$

300

Finally, if we pass to spherical coordinates, we get $\varphi_d = 138.362\,[deg]$ and $\lambda_d = 22.5694\,[deg]$, which together with δ provide us with the necessary informations regarding the magnetic dipole for the year 2016.

4.2. Cut-off rigidity estimation method

305

Having calculated the needed variables, we return to the main cut-off rigidity estimation method provided in 18.

In the first step we find geomagnetic latitude and longitude (a set of coordinates tied to Earths magnetic poles) using geographic latitude and longitude. This transformations between geolocation (λ_g, φ_g) and geomagnetic one (λ_m, φ_m) is given by the set of equations 15.

$$
\begin{aligned}
\lambda_m &= \arcsin\Big(\sin\lambda_g \sin\lambda_p + \cos\lambda_g \cos\lambda_p \cos(\varphi_g - \varphi_p)\Big) \\
\varphi_m &= \arcsin\Big(\frac{\cos\lambda_g \sin(\varphi_g - \varphi_p)}{\cos\lambda_m}\Big)
\end{aligned}
\tag{15}
$$

Where: $(\lambda_p = -80.4deg, \varphi_p = 107.3deg)$ are the coordinates of the magnetic North pole, taken for the year 2016.

315   Next, we have two sets of equations 16 and 17 which are written from

22

the Center of the Dipole coordinates.

$$x_d = \delta \times \cos\varphi_d \cos\lambda_d$$
$$y_d = \delta \times \sin\varphi_d \cos\lambda_d \qquad (16)$$
$$z_d = \delta \times \sin\lambda_d$$

Where (x_d, y_d, z_d) define the center of the dipole, and φ_d, λ_d and δ are the values found in the previous section.

$$x_c = \delta' \times \cos\varphi_c \cos\lambda_c$$
$$y_c = \delta' \times \sin\varphi_c \cos\lambda_c \qquad (17)$$
$$z_c = \delta' \times \sin\lambda_c$$

Where $\delta' = R_E + altitude\,[km]$, is the distance between the Center of the dipole and COSI, and (φ_c, λ_c) are the known geographic latitude and longitude of COSI during it's flight. Then we proceed to complete the cut-off rigidity estimation with equations 18.

$$d = \sqrt{(x_d - x_c)^2 + (y_d - y_c)^2 + (z_d - z_c)^2}$$
$$\Delta P = -3P \times \frac{\Delta d}{d}$$
$$P = 14.9 \times \cos^4\lambda_m \qquad (18)$$
$$\Delta d = d - R_E$$

Where: ΔP is the final cut-off rigidity estimation, d is the distance between COSI and the dipole center, and P is simplified P_{cut} taken from [2], calculated using geomagnetic latitude λ_m.

The final cut-off rigidity is graphically presented on Figure 14 for the

23

whole duration of the COSI's flight. In addition, we show a slight difference between the model calculated for the year 1998, which corresponds to the original calculation from 18 and our calculation using IGRF coefficients for the year 2016.
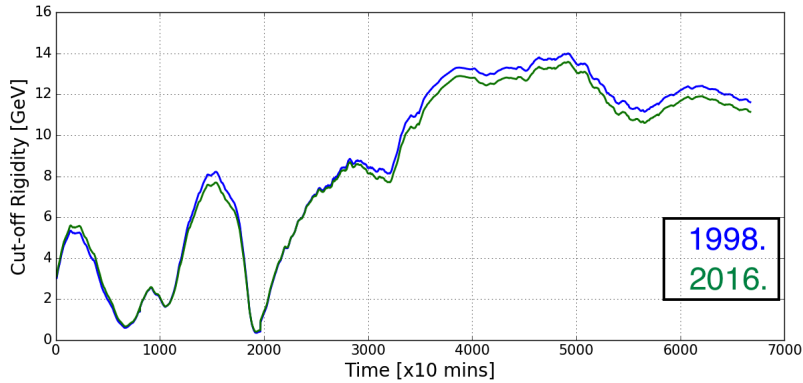

Figure 14: Estimated rigidity models. Blue- corresponds to model calculated for the year 1998. Green - corresponds to model using IGRF coefficients for the year 2016. Again these are averaged values for each 10 minutes of flight time.

For the purpose of comparison we also show the calculated rigidity, on Figure 15, compared to the used geographic latitude and longitude.

5. Background estimation and models

As previously discussed, we require a background estimation for the COSI instrument which would allow us to progress further in exploring the space instrumentation made with similar concept. We would like to be able to extrapolate our results i.e. the background model obtained with experimental data and have a valid estimation of a background and performance of a concept simulated using a similar geometry, same detectors and the same detection techniques as COSI used. To achieve this, we started by
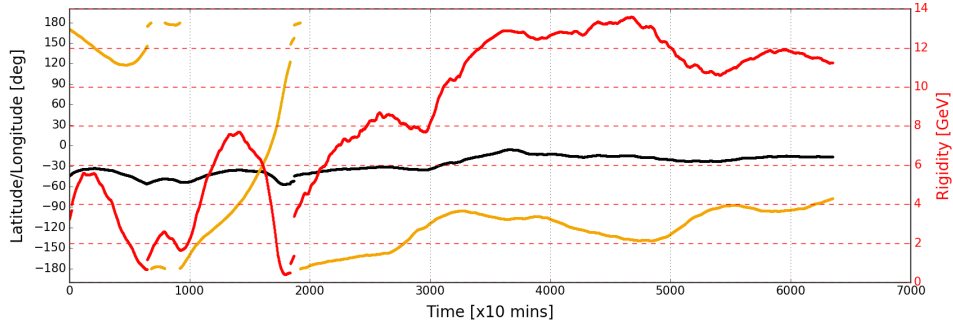
24

Figure 15: Calculated rigidity, expressed with red data with corresponding values on the right vertical axis, expressed in [GeV], shown, with respect to, geographical latitude and longitude – blue and yellow data respectively with corresponding values shown in [deg] on the left vertical axis.

incorporating the measured and analysed data, such as recorded altitude, estimated cut-off rigidity and recorded Compton and PE events obtained in the analysis described in the previous chapters.

5.1. Fitting the altitude and cut-off rigidity

We began to connect the available data by plotting a three variable dependency plots, in order to link the position of the COSI balloon in the atmosphere, with the recorded rates, either from the ACS or from the detected gamma-rays. One of such plots is seen on Figure 16, where we linked the altitude profile (see: Fig. 2), estimated rigidity (see: Fig. 18) and the calculated rates of 511 keV line from the selected Compton events, Fig. 8.

Now, going into more detail regarding the plot on Fig. 16 we notice a couple of trends. First, the rate of 511 keV line seems to go decrease as the cut-off rigidity grows from several up to $\sim$ 14 GeV. This is to be
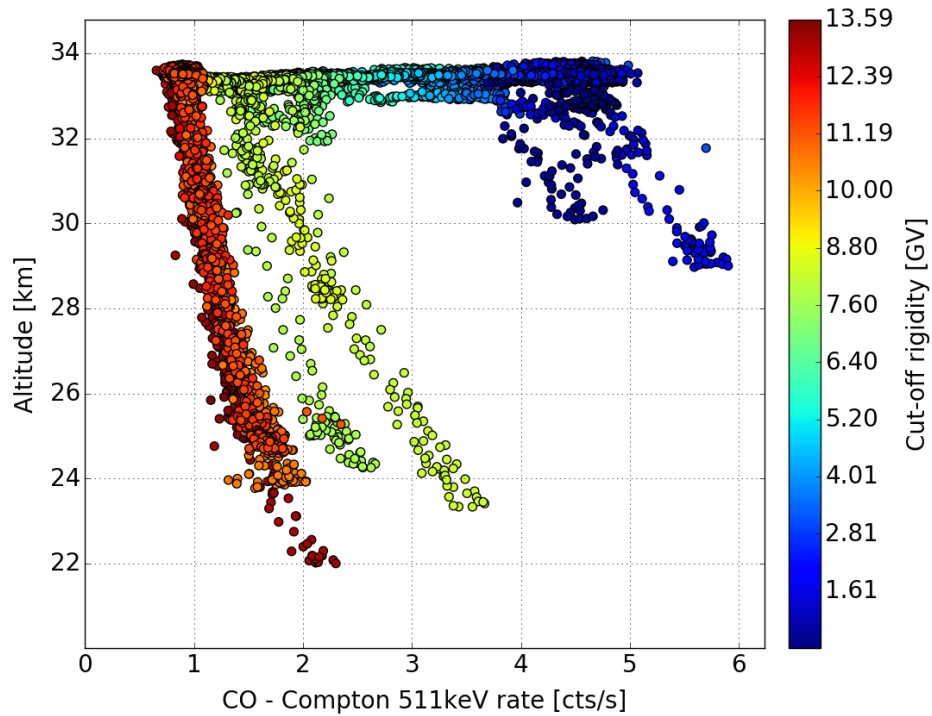
25

Figure 16: A three variable dependency plot, showing how the 511 keV rate from the Compton events changes with altitude oscillations, as well as the cut-off rigidity over the total flight time. Each point as before represents the averaged values over 10 minutes of flight time.

expected as the stronger rigidity means less cosmic rays. However, we did notice several irregularities, regarding such dependency, in the recorded data which will be discussed further in the text. Second important trend is the change of the Compton 511 keV rate with altitude oscillations. These can be seen as "fingers" on the plot for the points where Altitude [km] goes lower then $\approx 32\,km$. These groupings are also connected to several values of cut-off rigidity, which, in fact, was the first idea we pursued. We had

26

365 hopped to be able to fit each group (finger) where we have altitude drops, and do the selection criteria based on the different rigidity values (colors on plot). In fact, we wanted to have a fit of the type $R_{511} \sim f(Alt)$, $Rig = const. interval$. However, such approach has proven to be unsuccessful, as below 7 GeV there is not enough data and/or the data is not following

370 any trends specific trend, having big dispersions which we were not able to fit. One good fit which gave does give us a valid dependency of R_{511} from altitude changes was obtained for the group above $Rig \approx 10$ GeV. This group is presented on Fig. 16 in orange and red points and it can be seen isolated and plotted with the axis inverted on the Figure 17.

375   The two fit functions of the type $R_{511} \sim Altitude$ used on the plot in Fig. 17 are a simple exponential decay and a second order polynomial, equations 19.

$$R_{511} = f_1 \times e^{f_2 \times Altitude}$$
$$R_{511} = p_0 + p_1 \times Altitude + p_2 \times Altitude^2$$
(19)

On other hand if we return to the plot on Figure 16, we explored another

380 dependency of the type $R_{511} \sim Rigidity\, Altitude = const.$. In other words, we wanted to see how the 511 keV rate changes with cut-off rigidity. To do so, we replotted the Figure 16 to show us the desired dependency as seen on the Figure 18.

    Looking closer to the Fig. 18 we can note several data trends, such as

385 the peaks caused by altitude variations e.g. at $Rig \approx 8\, or\, 10\, GeV$. The darkest blue points on the top of the plot come from COSI ascend and the higher count rates for the same points probably come from irradiation passing through the Pfotzer maximum. However, if we now take this same
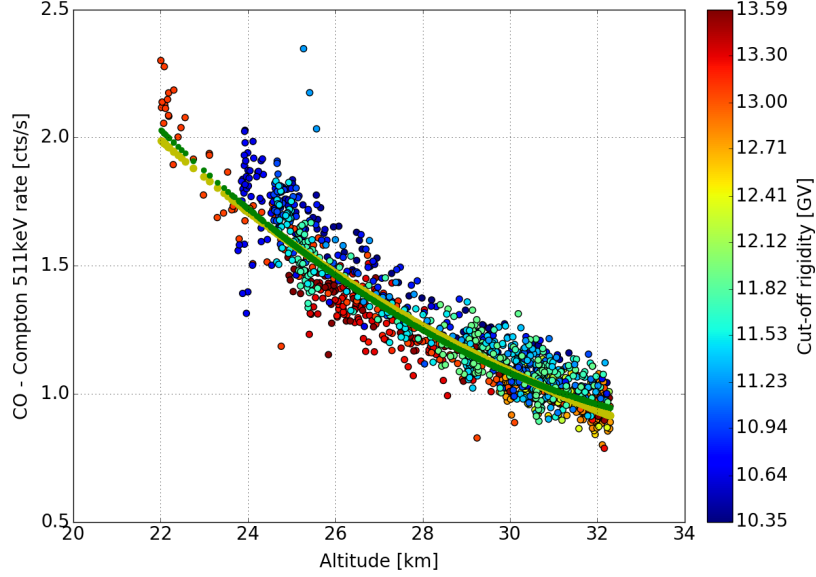
27

Figure 17: Figure showing the dependency of 511 keV rates from Compton events (CO on y axis in [cts/s] from the altitude changes (shown on x axis in [km]), for the periods of flight where cut-off rigidity (shown as colors with colorbar) was Rig≥10GeV. The data are dispersed but we were able to obtain two similar fits given by equations 19, with second order polynomial shown in green and exponential function shown in yellow.

plot 18 and select only the data points corresponding to the maximal altitude interval of the COSI, which is between 33 and 34 kilometres we have a bit different plot as seen on Figure 19.

Starting with the Fig. 19 we were able to explore further a dependency of the 511 keV count rate and the cut-off rigidity, $R_{511} \sim g(Rig)$, $Alt = const. interval$. Just by observing the plot we can note three decreasing threads of data points. The main one seems to nicely follow the exponential decay law, these are the points in blue, green orange and red on the plot.
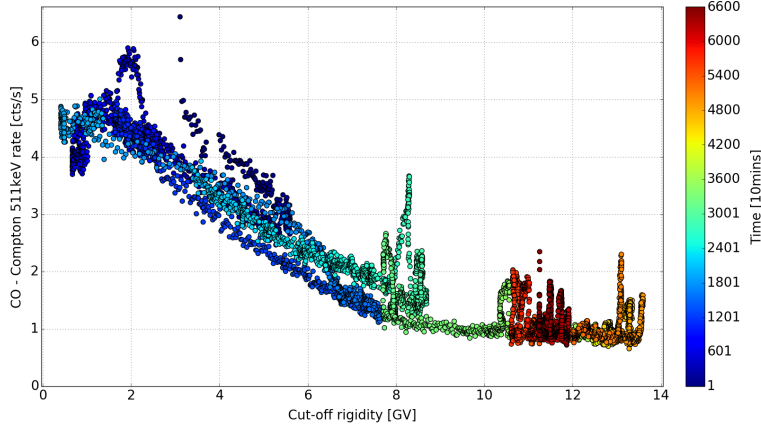
28

Figure 18: Dependency of the 511 keV rate from Compton events (y axis) from the cut-off rigidity (x axis), for the whole duration of the flight, where time is represented by colors related to the colorbar on the right hand side of the figure.

However, we see that the darkest blue points have increased count rates, as well as the points in light blue and cyan color (cut-off rigidity $4-8$ GeV). The first increase we associated, as mentioned above with the Pfotzer maximum and the COSI ascend, however the second trend remains problematic, and is highly affecting our predicted background models as we explain further.

Returning, to the "ideal" case from the Fig. 19 we could say that the majority of the data indeed corresponds to a type of exponential decay, and can the dependency of the 511 keV from cut-off rigidity can be fitted with a combination of polynomial and exponential functions given in equation 20 and shown on Figure 20. The residuals of such fit are $\approx 5.2\%$.

$$R_{511} = (6.78 - 0.9 \times Rigidity + 0.04 \times Rigidity^2) \times e^{-0.08 \times Rigidity} \quad (20)$$

29
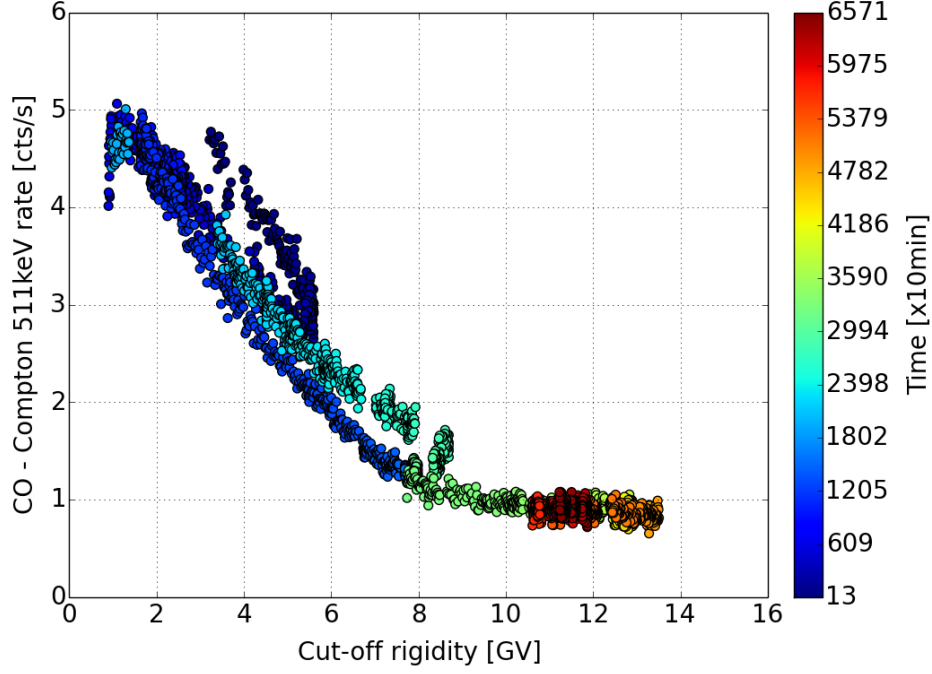
Figure 19: Same as Figure 18 with additional data selection criteria for the altitude to be above 33.2 km; $Alt \geq 33.2 \, km$.

However, in a realistic case we have to deal with the data shown on the Fig. 19. Here, we encounter a problem, such trends can be fitted with the same exponential mode, as shown in eq. 20 but it can also be fitted using only the polynomial function as a fit. Such fitting functions are shown on Figure 21 and given by the equations 21, with the corresponding residuals of 12% and 9% for exponential and polynomial fits, respectively.

$$R_{511} = (5.77 + 0.45 \times Rig - 6.6 \times 10^{-6} \times Rig^2) \times e^{-0.22 \times Rig}$$
$$R_{511} = (5.88 - 0.70 \times Rig + 0.03 \times Rig^2) \tag{21}$$

30
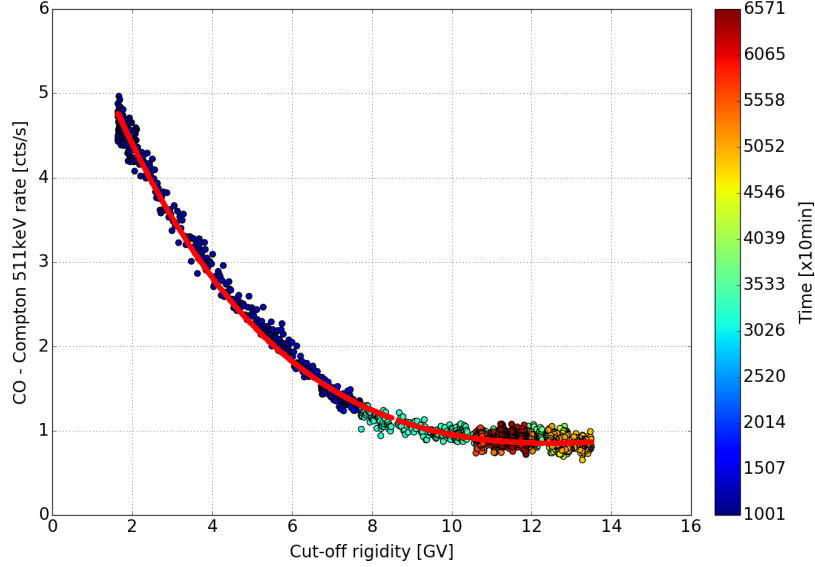
Figure 20: Ideal exponential fit

5.2. Background models

The first background approximation model (from here on also referred as "*Model* 0") is a function of a type: $R_{511} \sim f(Altitude) * g(Rigidity)$. To obtain the correct shape of such function we used the two independent fits of altitude, eq. 19 and cut-off rigidity, eq. 21 as guides. In such manner we created a single fit function with two variables (altitude and cut-off rigidity) and fitted the R_{511} rates for all the Compton events for the totality of the flight time, by letting the coefficients within R_{511}, be free parameters. The obtained results are presented on Figure 22 and the equations of the fits are

31
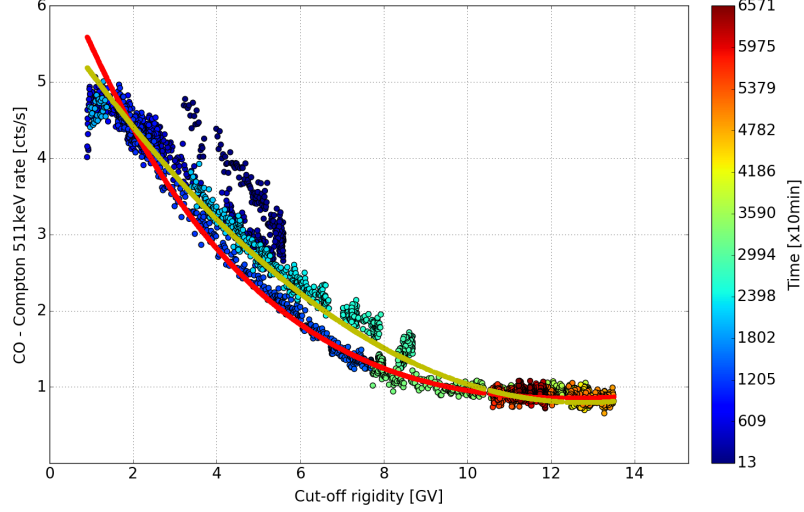
Figure 21: Two fit functions of the 511 keV rate dependency from cut-off rigidity for Alt$\geq 33.2\,km$. The exponential function (red line) and the polynomial (yellow line) are given by equation 21.

22 and 23.

First fitting function for $Model\,0$, shown in red on Fig. 22 and given by equation 22 is a complex fit using exponential and polynomial functions with 5 free parameters. The average value of the fitting residuals for this fit is $< Res_{Model\,0}^{complex} > \approx 10.8\%$.

$$R_{511} = \left((29.58 + 4.47 \times Rig + 0.18 \times Rig^2) * e^{0.06 \times Rig}\right) \times e^{-0.05 \times Alt} \quad (22)$$

Where, R_{511} is the rate of 511 keV line for Compton events and Alt and Rig represent altitude and rigidity. The other fit from the Fig. 22, corresponding

32
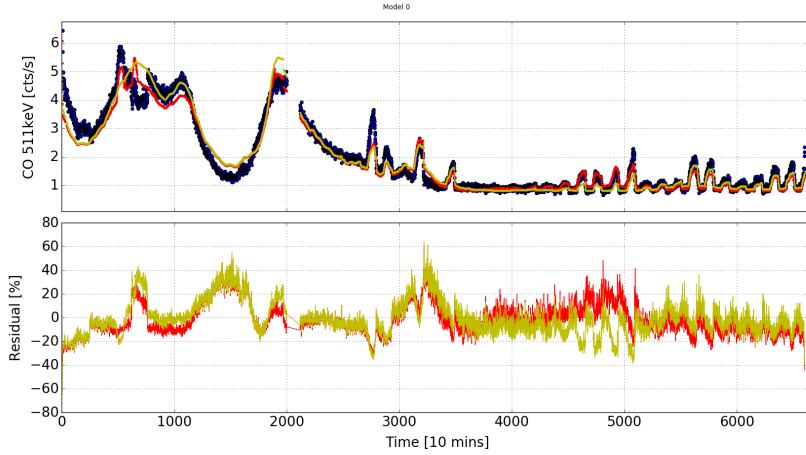
Figure 22: **Top** – Background estimated $Model\,0$. The 511 keV count rate is fitted with two functions given by equations 22 in red and 23 in yellow. **Bottom** – Fitting residuals corresponding to the two functions from the upper plot given in [%].

to the function and residuals represented in yellow on the figure, are a simplified fit given by eq. 22. The function, given by equation 23 is in fact a second order polynomial where the variable is the product of two variables – rigidity and altitude. The residual of such function is $< Res_{Model\,0}^{polynomial} > \approx 11\%$, which is almost equal to the residual $< Res_{Model\,0}^{complex} >$ but obtained with only three free parameters.

$$R_{511} = 5.80 - 2.26 \times 10^{-2} \times (Rig \times Alt) + 2.57 \times 10^{-5} \times (Rig \times Alt)^2 \quad (23)$$

As the first step to improve the $Model\,0$ and lower the high fit residuals, we tried to adjust the fit functions to the several observed periods (see: Sec. 2.3 and 12), where COSI had different instrumentation configurations (cases I – IV, Sec 2.3). Therefore, if we have one or multiple detectors not

33

working, we know that the ratio between the passive and active material changes. These changes should further influence the rates of the recorded events, as well as the recorded background contribution. Accordingly, here we introduce a new background model, which we will refer to as $Model\,1$ further in the text. The method is simple, use the fit functions given by equations 22 and 23 and fit the four different configurations (cases I – IV, Sec 2.3) by having four sets of parameters for these intervals. On the Figure 23 we show the $Model\,1$ applied using 23 i.e. a simpler second order polynomial fit. In such way we obtain an average value of the fit residual $< Res_{Model\,1}^{polynomial} > \approx 9.63\%$. Which is a slight improvement over the $Model\,0$ fits.
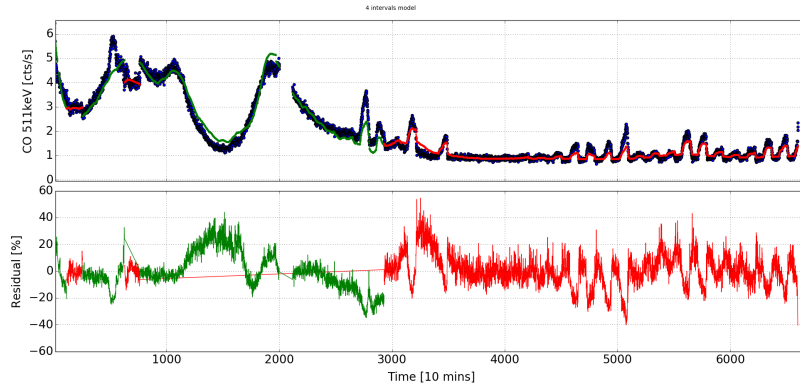
Figure 23: **Top** – $Model\,1$ of the background estimation. With green and red colors denoting different periods fitted with functions of the shape 23 using different fit parameters. **Bottom** – Fit residuals given in [%].

Another similar test was done using the relation given in Sec. 2.2, Figure 10 and by equations 7 and 8. In a similar way as for previous models we created an estimation of the background using the relation between 511 keV

34

line rates from Compton events and the count rates from the ACS. This model, named $Model\,ACS$, was also adjusted for the several periods with different detectors turned on and off. Both of these fits are presented on Figures 24 and 25.
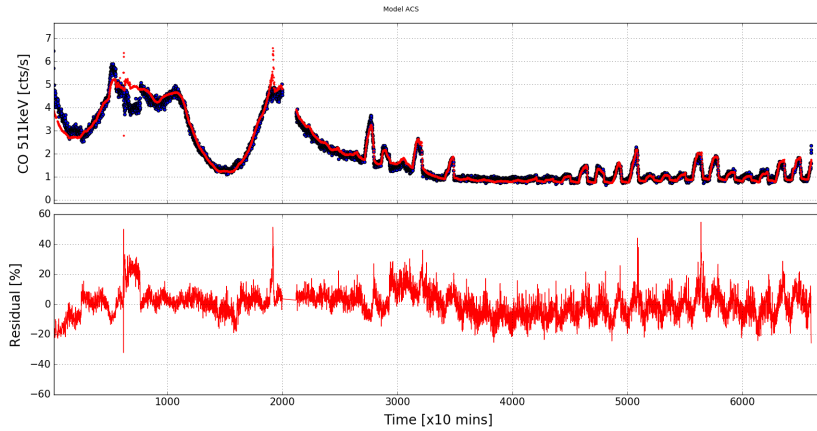
Figure 24: **Top** – $Model\,ACS$ fitted with quadratic function eq. 24. **Bottom** – Residuals of the fit given in [%].

The fit presented on Fig. 24 is a quadratic function given in equation 24, with the fit residuals $< Res_{Model\,ACS} > \approx 6.9\%$.

$$R_{511} = -0.63 + 2.16 \times 10^{-4} \times R_{ACS} - 1.56 \times 10^{-9} \times R_{ACS}^2 \qquad (24)$$

Results presented on the Figure 25 correspond to the $Model\,ACS$ adjusted for different detectors ON/OFF periods, using again a quadratic fit function with different parameters for different periods. The final residual of such fit is $< Res'_{Model\,ACS} > \approx 5.9\%$.

Two further improvements are planned to be added to the fit. Explore the contribution of the delayed radiation component, which should be of

35
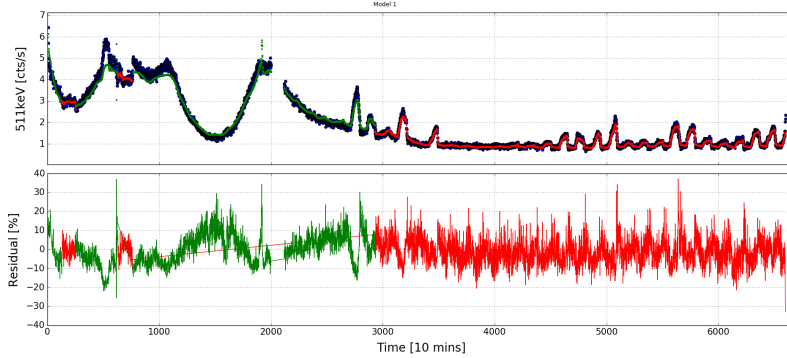
Figure 25: **Top** – *Model ACS* fitted with multiple quadratic functions, with parameters corresponding to the periods with different number of working Ge detectors. **Bottom** – Residuals of the fit functions given in [%].

the shape of $e^{\frac{t}{\tau}}$ where t is the time and τ is the decay constant and an exploratory effort to search for the contribution of the galactic center when it is in the field of view of the COSI.

5.3. 511 keV Model Improvement

To further improve the 511 keV modeling, we have completely reworked the python codes for data analysis and selection, this was done to verify already done work and gain another level of analysis and optimize speed for data selection and processing. Regarding the 511 keV line we have tested two additional python scripts for line and background selections i.e. estimating the number of counts within a selected peak. First we simplified the method explained in Section 3, creating an automatic algorithm which searches for a peak maximum within a given range e.g. $511 \pm 3keV$ within the energy spectrum histogram, then it finds the two local minima around the peak within given borders e.g. from $511 \pm 10keV$ to $511 \pm 20keV$ and using a simple trapezoid rule subtracts everything below the line connecting the two

36

minima. The simple method is illustrated on the left panel of Fig. 26.
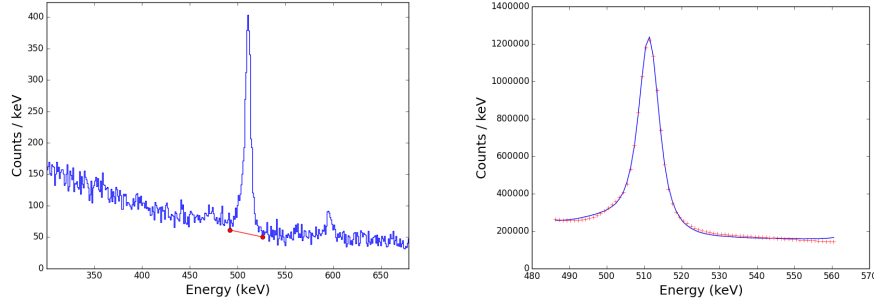
Figure 26: **Left** – Simple illustration of the algorithm used for line selection, for the 511 keV line from Compton selected events, for the period of $\Delta t = 10\,minutes$ of the flight time. **Right** – Example of fitting with python library: recorded 511 keV peak (in blue) fitted with a complex function of power law and a Gaussian (in red), for the duration of one flight day.

⁴⁸⁵ Second peak selection method, included using a fitting library for python, where we used a complex fit made out of two or more functions. First function was usually a power law or a linear function, which represented the background and second function such as Gaussian or Lorentzian function, which represents the peak was superimposed on top of the first one. An ⁴⁹⁰ example is given on the right panel of Fig. 26 However this proved to be rather complex and time consuming so we concluded that simple method correctly and fast provides accurate approximation of the number of counts within a peak.

Continuing with a simple peak selection criteria we redid the background ⁴⁹⁵ modeling as presented in previous Chapter and obtained another model of the 511 keV rate as a function of altitude and rigidity, similarly to result shown on Fig. 22. However, this time, instead of continuing with the path of multiple detector failure (Fig. 23) and correcting for different instrumental configurations, we tried to correct for other possible processes which con-

37

tributed to rather high fit residuals as seen on the the results from previous Chapter.

First improvement is concerning the first several days of flight. We started by assuming that by ascending the COSI instrument passed the Pfotzer maximum somewhere between 10-25 kilometers, and indeed by zooming in on the beginning of the 511 keV rate plot e.g. Fig 9 we can se a clear peak of the increased rate followed by a tail. Both should be a consequence of high activation within a specific layers of atmosphere followed by decay period. To further study this part of the flight, we compared an average energy spectrum from Compton events for the first one and a half day of flight, or approx. 36 hours. followed by the next 36 hours. In such a way we could produce a complete energy spectra and compare the differences at the moment of intense activation and at the time following it over several days. An example of such spectra comparison is shown on Figure 27. It is clear that the activation is effecting all of the observed background lines and therefore is not a product of a specific isotope or a process, but mainly is a consequence of higher activation caused by higher flux of primary and secondary cosmic particles produced in the atmosphere.

To compensate for the increased events production, we decided to add a time dependent decay component to the 511 keV fit model. Such component was found by fitting the first two days of flight by fitting the 511 keV production rate over time with a polynomial function, as done in the previous Chapter and adding an exponential component 25

$$R_{511} = Polynomial(altitude, rigidity) + e^{kt} \qquad (25)$$

where the Polynomial represent the already existing fit function, k rep-

38
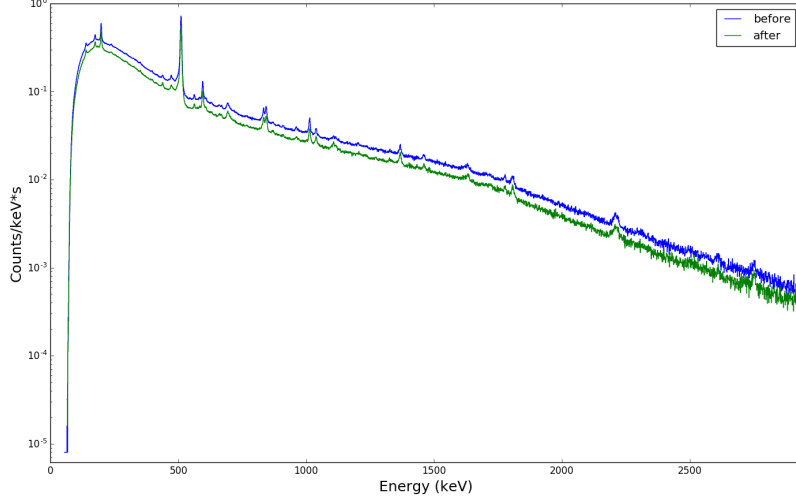
Figure 27: Comparison of two histograms representing two energy spectra: blue corresponds to start of the flight until a selected break date – 18th May at 12:00 UTC; and green corresponding to the period from the break date until the end of third flight day – 19th May at midnight. The spectra are represented as average rate $[counts/(keV \times s]$ (y-axis) over 1 keV bins (x-axis).

resent the decay constant and here is used as free fit parameter, and t is the flight time. In such a way we have greatly increased the precision of the 511 keV production model by improving the fit error over first several days from 20% to 6%. Next step was to add another parameter to represent the Pfotzer maximum itself as the fit improvement wasn't enough. This was done by fitting the first hours of the flight trying to model the small peak in 511 keV rate, caused by passing through the Pfotzer maximum. The improved model is given by eq. 26,

$$R_{511} = Polynomial(altitude, rigidity) + e^{k_1 t} + e^{k_2 t} \tag{26}$$

where, Polynomial and $e^{k_1 t}$ functions are the same as in 25 while $e^{k_2 t}$

39

corresponds to free parameter k_2 and flight time from the Pfotzer maximum fit. The finished process is illustrated on the Figure 28.
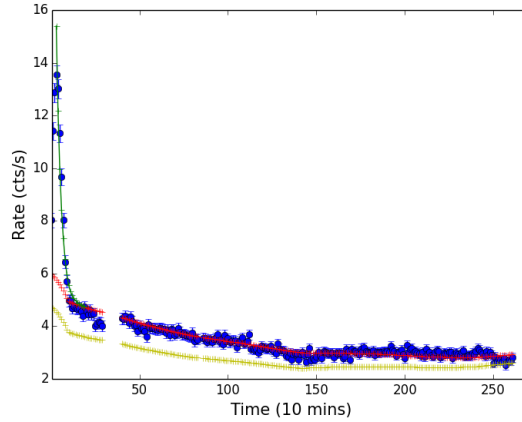
Figure 28: Illustrated improvement of the model of 511 keV production rate over the first two days of flight. In yellow is represented $Model\,0$, in red improved model given by equation 25 and in green we can see the improvement brought by the second factor in equation 26.

⁵³⁵ Second bigger improvement to the 511 keV model, was to correct the big altitude oscillations within second half of the flight. These were caused by the day night cycle, and are represented e.g. on Fig 8. Additionally, it is clear, by observing any of the presented 511 keV models the fit doesn't correctly represent such oscillations, which causes increased model inaccu-
⁵⁴⁰ racy. Returning to the Fig. 16, $Model\,0$ or $Model\,1$ take into account that the majority of the flight is at maximal altitude e.g. between 32.-34. kms. as was discussed previously. However, there is a clear problem once the altitude is lower within different rigidity regions, here the fit is not good enough. Fig. 16 clearly shows several trends of 511 keV rates change within
⁵⁴⁵ different rigidity bands, e.g. above 10 GV or between 6-10 GV etc, and

40

this can be seen on fit residuals of shows Models as well, specially the problems with second half of the flight. Therefore, we decided to introduce a simplified solution, and treated altitude changes as if we would activation. Saying that once an altitude drops for 5-10 kilometers the surroundings of the COSI become more active, having higher fluxes of atmospheric particles thus activating the instrument and passive material more. We take this into account by adding a third component to our basic polynomial model, as shown by equation 27:

$$R_{511} = Polynomial(altitude, rigidity) + e^{k_1 t} + e^{k_2 t} + e^{p_2 \times Altitude[km]} \quad (27)$$

where, the first part of the euqation is identical to eq. 26 and the last member is an exponential function of altitude and a free fit parameter p_2. The effect of this fix is shown on Figure 29.
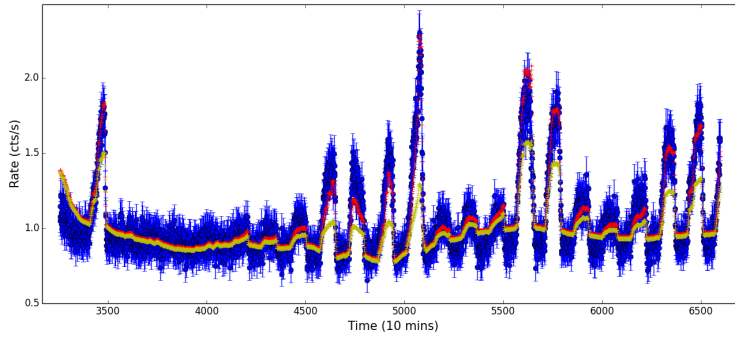
Figure 29: Brief illustration of the improvement achieved by having a last member in the equation 27: In yellow we show a 511 keV production model given by eq. 26 and in the red the one given by equation 27. The time period covers last 21 days of flight, with the improvements to the fit error from $\approx 10\% \, to \, 8\%$.

Finally taking into account all of these improvements we created a new model for 511 keV rates, based on $Model \, 0$ and $Model \, 1$ and eq. 26 and is

41

given by eq. 27 and shown on Figure 30.
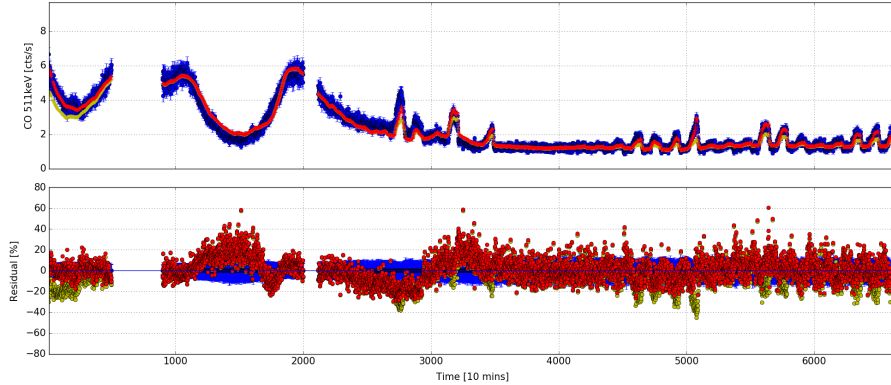
Figure 30: **Top** – Comparison of Model 0 (given in yellow data points) and improved 511 fit model given by equation 26 (in red). **Bottom** – The improvements to the fit are illustrated by the residuals plotted, with the colors corresponding to above given functions. With: $< RES > Model0 \approx 10.5\%$ and $< RES > Improved \approx 8.9\%$.

₅₆₀ *5.4. Checking for Galactic Center contribution to the 511 keV line*

One of the side tests we performed was to rapidly utilize a method explained in e.g. [4] to check if COSI observes the galactic center and to see if there is a contribution to the 511 keV production significant enough to influence our presented fit models. The method referred from now on as ₅₆₅ "mirror method" is based on a simple approximation of the source observed by the Compton telescope and by background subtraction using the so called mirror point. The idea is that if background is uniform we can take an azimuthally symmetrical point in the sky called a mirror point and give it the same treatment as we would to a potential source. Therefore if a real ob- ₅₇₀ served source is a source it should have a number of excess events which are produced by the physical body creating that source compared to the number of events in the mirror point which should represent the background.

42

Such method has been tested and proved and provides a rough idea of the source strength which is perfect for our needs. We tried the method on several data sets, each representing a day of flight, and in the following bullets bring the major data selections (with number of remaining events after each step) and operations performed to obtain a final result.

- *Start data set* – Full day of flight 25. June 2016.

- *Events selection* – Detected Compton events: 3.5 M events

- *Compton scattering angle* – Only events with $\Theta_{Compton} \leq 40^o$: 800k evts.

- *Energy selection* – Events within $\Delta E = 511 \pm 30 keV$.: 80 k evts

- *Horizon cut* – Selecting events coming from above the instrument horizon: 70k evts.

- *Zenith cut* – Events coming within $\Theta_{Zenith} \leq 70.^o$: 50 k evts.

- *GC and MM cut* – Selecting events within $r = \pm 5.^o$ around GC and MM positions.

Several results are illustrated on the following Figures 31, 32

From the Fig. 32 it was evident that there is indeed observed excess of 511 keV Compton events originating from the galactic center, however taking into account all of the performed data selections the end number of these events (several hundred per day) was not enough to cause a noticeable effect on the modeling of the 511 keV line production within the atmosphere during the whole flight duration.
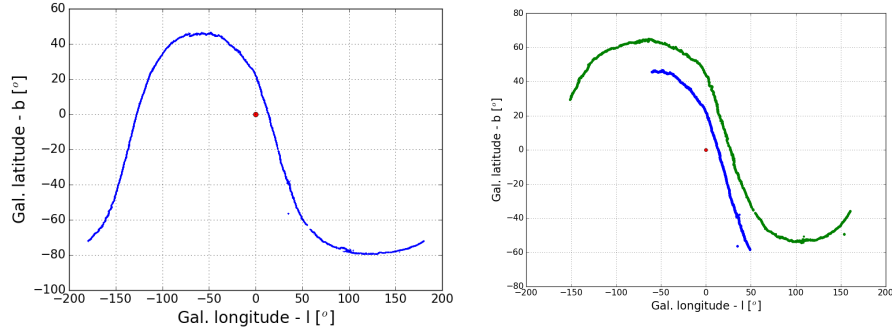
Figure 31:   **Left** – Orientation of the COSI's z-axis (shown in blue) in the galactic coordinates, longitude (l) and latitude (b) in degrees, corresponding to X and Y axis respectively. Red dot represents Galactic center (with coordinates $l = b = 0^o$. **Right** – Similar plot after several data selection steps, with added position (in green) of the calculated mirror point corresponding to symmetrical position of the galactic center tied to the COSI Z-axis (in blue).
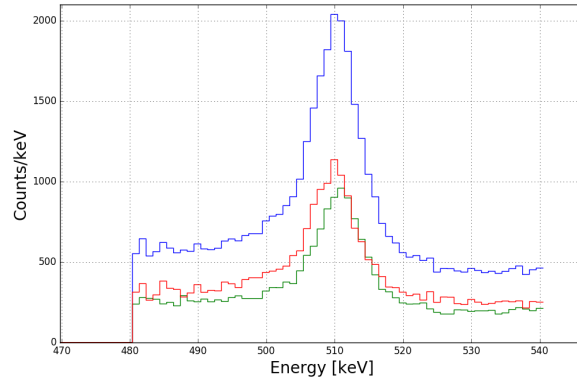
Figure 32: Final result of the mirror method, showing the selected 511 keV energy spectra. In blue is the number of counts per keV bins within $d = 10^o$ circle around the galactic center, and in green for the mirror point. Finally the red gives the difference (by subtraction) between the two, corresponding to the total of ≈ 200 events for one day (25.06.2016.) of flight time.

44

5.5. Modeling other background lines

Observing the recorded energy spectrum, integrated over the whole flight time given by Figure 33, we decided to perform a rapid study of several other background lines.
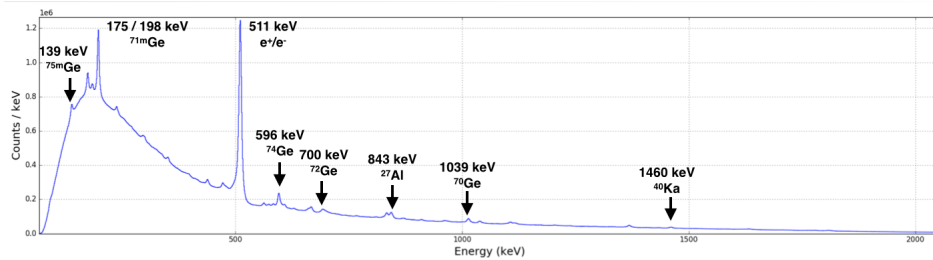
Figure 33: Energy spectrum for the whole flight duration in [counts/keV] per 1 keV bins, with noted some of the stronger background lines used in analysis.

Here we opted for a specific selection of the lines strong enough that we could extract a time profile during the flight time, in a similar way we did for the 511 keV line. Only several lines were strong enough for such analysis:

- 139 keV from ^{75m}Ge, shown of Fig. 36

- 198 keV from ^{71m}Ge, shown of Fig. 37

- 596 keV from ^{74}Ge , shown of Fig. 38

- 1460 keV from ^{40}K, natural radioactivity , shown of Fig. 39

Some of the examples of the line selections using both custom algorithm and more complex – the double fit functions using a python library are presented on Figures 34 and 35. Again we opted for the simpler method to estimate the number of events in selected peaks within a specific time interval.
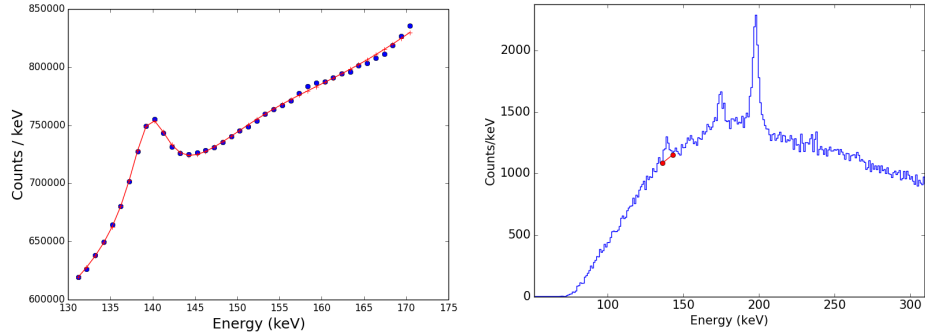
Figure 34: **Left** – An example of fitting a 138 keV line using a power law for the background and a Gaussian function for the peak. **Right** – Using an algorithm to roughly estimate the number of counts within a 138 keV peak, for the period of $\Delta t = 1 hour$ of flight time.
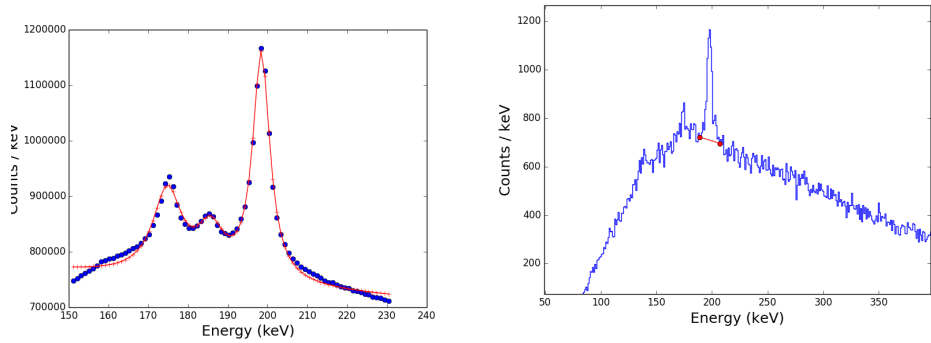
Figure 35: **Left** – Same as on Figure 34 but using a linear function for a background and three Lorentzian functions for the three peaks corresponding to background complex between 170 and 200 keV. **Right** – Rough estimate of the number of counts within a 198 keV peak, for the period of $\Delta t = 30 mins$ of flight time.

The models for background lines production over time depending on atmospheric position, shown on Figures 36 through 38, are fairly consistent with the ones we obtained for the 511 keV. The same trend through the flight period, and similar fluctuations of the lines rate with rigidity and altitude are seen. All have been fitted with a function, eq. 27, which shows that

46

the polynomial model works pretty well within the uncertainties dependent from mostly available statistics (number of events).
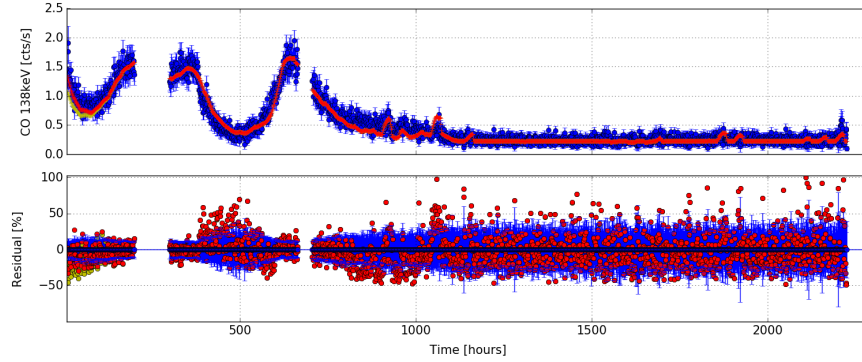
Figure 36: **Top** – The 139 keV line from ^{75m}Ge production [evts/s] averaged over each 1 hour of flight time (blue points) with calculated uncertainty (blue bars). The fit is given by 27 (shown in red). Yellow points show an older $Model\,0$ to illustrate an improvement in reproducing the first several days of flight as discussed in previous subsection. **Bottom** – Corresponding fit residuals expressed in percentage (red/yellow points), with blue bars showing again the sigma from the top plot. The large residuals are mostly influenced by poor statistics. The overall mean precision is $< RES > \approx 36\%$.
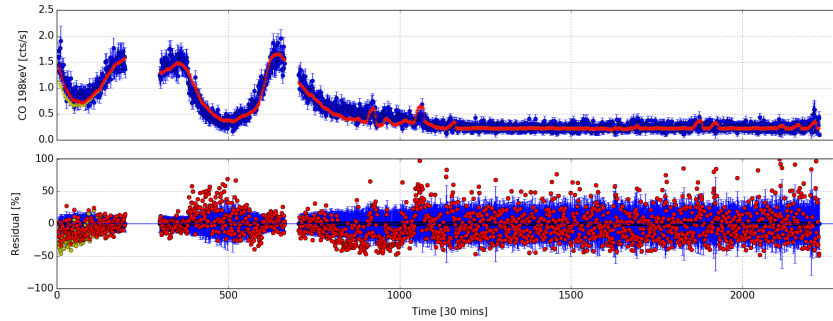
Figure 37: Same as Fig. 36 but calculated for 198 keV line from ^{71m}Ge averaged over each 30 minutes of flight, obtaining $< RES > \approx 20\%$.

Finally, a quick study of ^{40}K line, Figure 39, shows a fairly constant rate

47
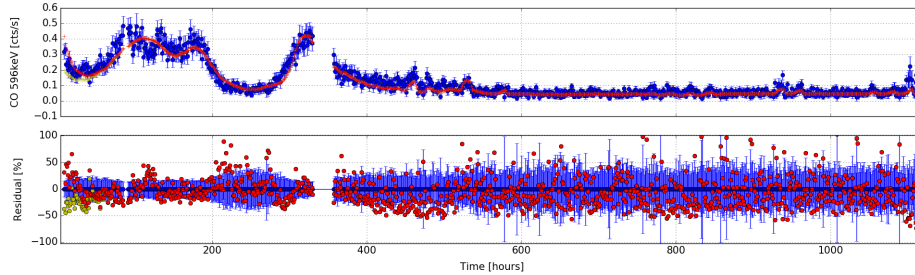
Figure 38: Again, same as Fig. 36 but calculated for 596 keV line from ^{74}Ge averaged over each 1 hours of flight, obtaining $< RES > \approx 20\%$.

of the 1460 keV line over the second half of the flight (right side of the plot), as was expected due to the nature of the line. However, the fluctuations in the rate shown in the first half of the flight is probably due to inconsistent instrument configuration, as noted in Section 2.3, multiple detectors went on and off due to instrumental problems which then causes the changes in recorded rates of all events.
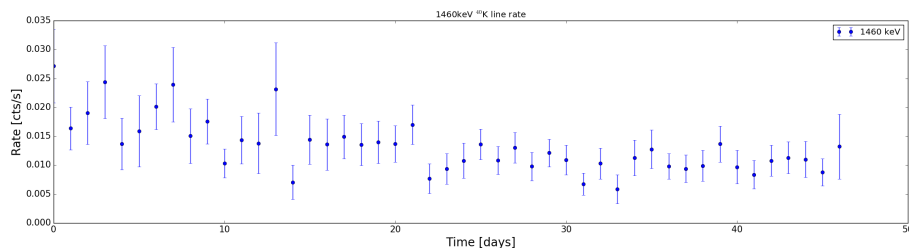
Figure 39: Production of $^{4}0K$, 1460 keV line over 46 days of flight.

6. Modeling the continuum part of the energy spectra

Here we will show the application of a similar logic previously demonstrated for modeling the background lines, (previous Section) on the modeling of the background continuum. We started by selecting a default energy

48

band value e.g. $\Delta E = 100\,keV$ and finding an average values of recorded rate

630 [events/second] within a predefined time interval $\Delta t = 10.\,minutes$. Same as we did for the background lines. Having such information, we could plot and fit the rate change over the flight time for each of these energy bands. One of such examples is shown on Figure 40.
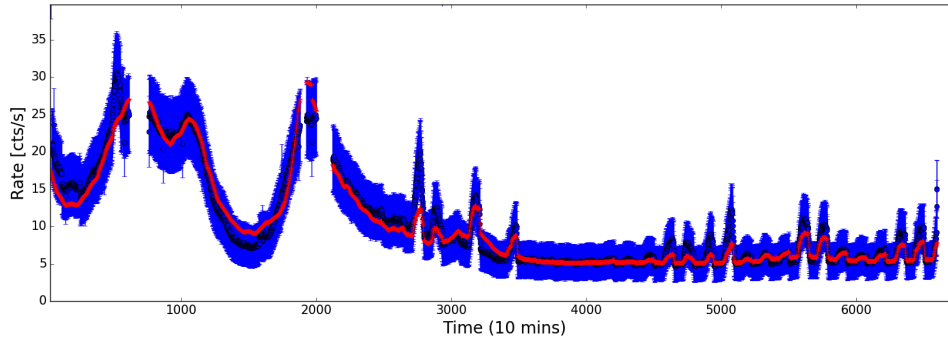
Figure 40: An example of fitting the events rate [cts/s] averaged over each 10 minutes of flight time for the selected events within an energy band $\Delta E = 300 - 400\,keV$. Used fit is a simple polynomial function of third order of $(altitude \times rigidity)$ as in $Model\,0$, with $< RES_{300-400} > \approx 8.7\%$.

The events rate within this band could be fitted fairly well with a function

635 given by eq. 28 which corresponds to a polynomial function of COSI's atmospheric position (altitude and rigidity), as was done in $Model\,0$ and $Model\,1$

$$Rate_{\Delta E} = \sum_{k=0}^{n} c_k \times x^k \tag{28}$$

where, k is the power of polynomial function, we found that $k = 2 - -4$ all works well, and where c_k are the polynomial coefficients and $x =$

640 $Altitude[km] \times Rigidity[GV]$.

49

Next step was to automate such fitting process and produce a set of fit functions of the above type, eq. 28 for each of the $\Delta E = 100\,keV$ energy band between 100 and 2500 keV. Using these 25 fit equations we studied their coefficients c_k and the contribution of each polynomial component $c_k \times x^k$, as can be seen on Figures 41 and 42. From here we obtained the dependency of fitting parameteres c_k of the mean energy of used energy bands.
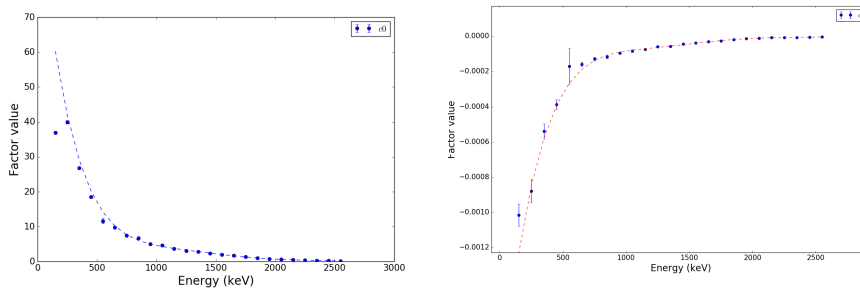
Figure 41: **Left** – First parameter c_0 from a polynomial fit model (eq. 28), fitted with another fourth order polynomial function depending on the energy of the band (x axis) **Right** – Same thing done for the second parameter c_2.
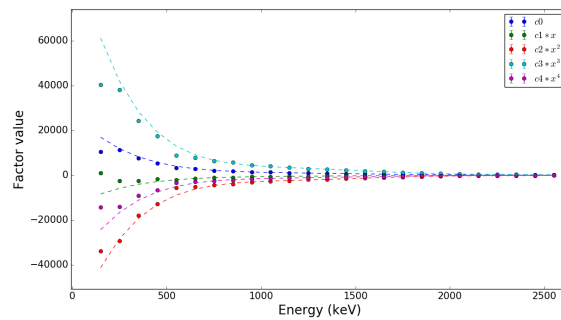
Figure 42: All elements $c_k \times x^k$ of the polynomial fit eq. 28 with corresponding fits.

The data points for each of the c_k coefficients are fitted with a polynomial

50

function of a fifth order, given by eq. 29.

$$c_k(E) = \sum_{l=0}^{n} q_l \times E^l \qquad (29)$$

where: l is the power of polynomial function, q_l are its coefficients and E is the mean energy for used energy band (e.g. from 200-300 keV, E $= 250$ keV). Once this has been done for each of the $c_k\, where\, k = 0, 1, ..., 5$ and for each of the 25 energy bands, we were able to construct an overall fitting function which would model the production of Compton events within a any energy range and within any instrument position in the atmosphere. This general model is based on eq. 28 and is given by eq. 30.

$$Rate[evts/s] = \sum_{m=0}^{n} C_m(E) \times X^m(Altitude[km], Rigidity[GV]) \qquad (30)$$

where simple polynomial coefficients from eq. 28 have been replaced with complex functions of energy $C_m(E)$. Some of the examples of such function are shown on Figures 43 and 44
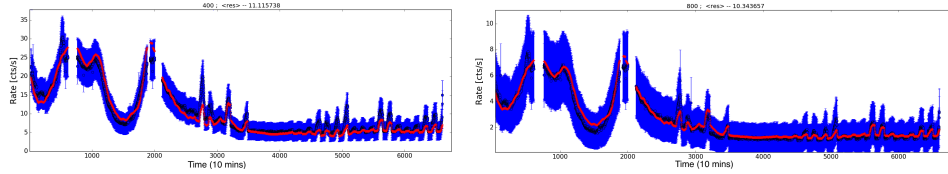
Figure 43: **Left** – Model of the Compton events production over the flight time (avg. rate [evts/s] per each $\Delta t = 10\, mins$ of flight time. Blue points with bars represent the recorded rate, while red points show the corresponding fit given by eq. 30 for the energy interval between 300 and 400 keV, with average fit residuals on the bottom panel of $< RES >_{300-400keV} \approx 11\%$. **Right** – Same as on the left plot for an energy interval from 700 to 800 keV and $< RES >_{700-800keV} \approx 10\%$
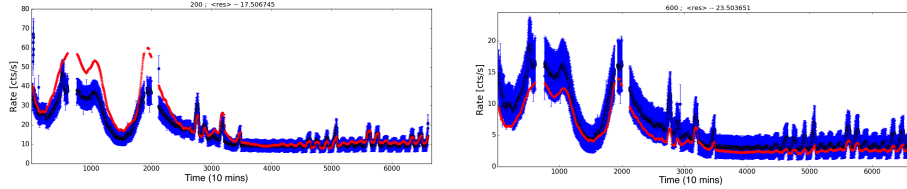
Figure 44:   Same as on figure 43, but for energy bands of $\Delta E = 100 - 200 \, and \, 400 - 500 \, keV$, on the left and right plot respectively. It is clear that the fit function provided by eq. 30 reaches its limitations when the overlaying background lines i.e. 138, 198 and 511 keV are too strong even with subtraction of the total number of events from the peak. The obtained average residuals are $< RES >_{100-200keV} \approx 18\%$ and $< RES >_{500-600keV} \approx 23\%$

Discussing the above results we have several notes to add. While fitting
660   the bands with stronger background lines, the counts obtained for the lines (Section 5.) for the same selected period of time Δt were subtracted from the number of events calculated for the energy band. This has been done for $\Delta E = 100 - 200 \, keV$ with lines 139 and 198 keV as well as $\Delta E = 500 - 600 \, keV$, and line 511 keV. Nevertheless, as shown on Fig. 44 the
665   fit provided by eq. 30 is underperforming as the background continuum is strongly influenced by the produced lines, and simple line subtraction wasn't adequate to compensate for this. Furthermore, above $E = 1. \, MeV$ the used statistics (events per time interval within energy range) becomes lower which creates large standard deviations on the calculated average rage
670   points. This is caused by the width of the energy bands being too low, or the time period being too short to have enough events not to be overwhelmed by statistical uncertainties (1σ). Therefore, in a second run adjustments were made. We used larger energy intervals $\Delta E = 200 \, keV$ and a time interval of $\Delta t = 1 \, hour$. Furthermore, since the trends shown on Figs. 41 and 42
675   become more linear the fit of the energy dependent coefficients $C_m(E)$ (eq. 30) became simpler, as equation 29 becomes simplified polynomial function

52

of fourth order, opposed to sixth order used for the energy ranges between 0.1 and 1.2 MeV. Such results are illustrated on Figure 45.
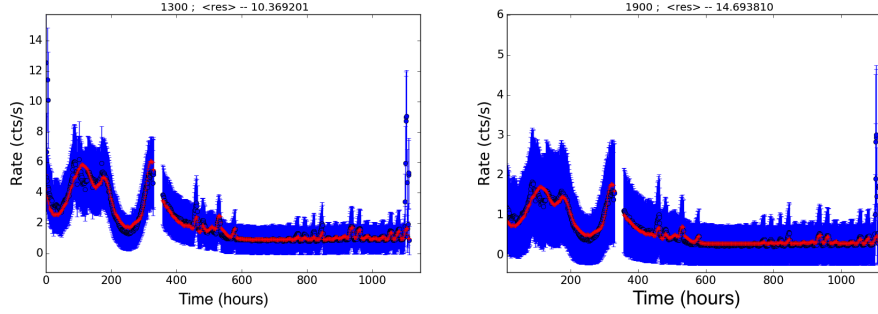
Figure 45: Similar to two previous figures but for $\Delta E = 1200 - 1400 \, and \, 1800 - 2000 \, keV$, on the left and right plot respectively. The used statistics for the average rate over time (blue points) is still not adequate but better then before. The obtained average residuals are $< RES >_{1200-1400keV} \approx 10\%$ and $< RES >_{1800-2000keV} \approx 15\%$, showing that such modeling works pretty well up to 2.0 MeV.

Finally, we may conclude that provided model having an average fit residuals $< RES > \approx 10\%$ over a majority of the covered energy range (0.2 - 2. MeV), is working well to predict the production of Compton events over the flight period of COSI within the atmosphere.

7. MEGAlib simulations

TBA

7.1. L2 orbit

TBA

8. Conclusions

TBA

References

[1] A. Zoglauer, et al., MEGAlib - The Medium Energy Gamma-ray Astronomy Library, New Astronomy Reviews 50 (2006) 629–632. `doi:10.1016/j.newar.2006.06.049`.

[2] Marco Potenza and Davide Grandi, Cut-off rigidity estimation guide. URL `http://hpamsmi2.mi.infn.it/~wwwams/geo2.html`

[3] E. Thébault, et al., International Geomagnetic Reference Field: the 12th generation, Earth, Planets and Space 67 (1) (2015) 79. `doi:10.1186/s40623-015-0228-9`. URL `https://doi.org/10.1186/s40623-015-0228-9`

[4] P. von Ballmoos, et al., Centaurus A Observation at MeV - Gamma-Ray Energies, Astrophysical Journal 312 (1987) 134. `doi:10.1086/164855`.

team 3 : Laue Lens & wide field monitor and spectrometer (ASTENA)

UNIFE: Piero Rosati, Filippo Frontera, Cristiano Guidorzi, Enrico Virgilli
INAF-IASF Bologna: Lorenzo Amati, Natalia Auricchio, Loredana Bassani, Riccardo Campana, Ezio Caroli, Fabio Fuschino, Claudio Labanti, Angela Malizia, Mauro Orlandini, John B. Stephen
DTU Space, Copenhagen: Carl Budtz-Jorgensen, Irfan Kuvvetli, Soren Brandt
INAF, Osservatorio Astronomico Brera, Merate: Giancarlo Ghirlanda
INAF, Osservatorio Astronomico Bologna: Roberto Gilli
University of Coimbra, Portugal: Rui Curado da Silva

ASTENA Simulation Working Group final report

Enrico Virgilli et al.

October 2018

The ASTENA mission, conceived within the EU funded the AHEAD framework, consists of two coaligned instruments, a broad band Wide Field Monitor/Spectrometer WFM/S and a broad band Narrow Field Telescope (NFT). In the NFT a large geometric area Laue lens (3 m diameter, 20 m focal length) allows to focus the radiation of the 50 - 700 keV energy pass-band. Differently from other proposed Laue lenses in the past, the NFT is made of optimised thickness bent crystal tiles, made with Silicon and Germanium. With these assumption we have optimised the instrument Field of View (FoV) to 3.5 arcmin with the angular resolution of 20". The Laue lens is coupled with a high efficiency ($>80\%$ above 600 keV) focal plane position sensitive detector, with 3D spatial resolution of at least 300μm in the (X,Y) plane and fine spectroscopic response (1% @511 keV) and with polarization sensitivity. In this paper we will mainly describe the NFI geometry and its simulated performances but also an overview on the main satellite configuration and a description of all the instruments will be done. The wide field monitor and spectrometer (WFM/S), mainly dedicated to GRBs, is composed by different units and is sensitive in the range 1 keV - 20 MeV. The total isotropic detection area will be $\sim$3.0 m2 with a FOV of about 1.35 sr. The WFM will allow the detection and spectroscopic and polarimetric characterization of all classes of GRBs. Each WFM module is a coded mask telescope that will allow the source localization within few arcmin up to 50 - 100 keV. The detector core is based on the coupling of low-noise, solid-state Silicon Drift Detectors (SDDs) with CsI(Tl) scintillator bars. Low-energy and high-energy photons are discriminated using the on-board electronics. The instrument design and preliminary experimental characterizations are reported and discussed in this report.

1 The ASTENA mission concept

The Advanced Surveyor of Transient Events and Nuclear Astrophysics (AS-TENA) is a designed mission which was conceived within the EU supported AHEAD project (Integrated Activities in the High Energy Astrophysics Domain [20]). The AHEAD goal is to support an efficient synergy and interaction in the european astrophysics community between scientists, engineers and technical support in order to end up with common projects at the most advanced state of the art that will provide the highest throughput for the next X- and Gamma-ray missions.

Particularly, within the AHEAD/Work Package 9 (WP9), simulations, feasibility studies and assessment of instrumentation devoted to the hard X-ray
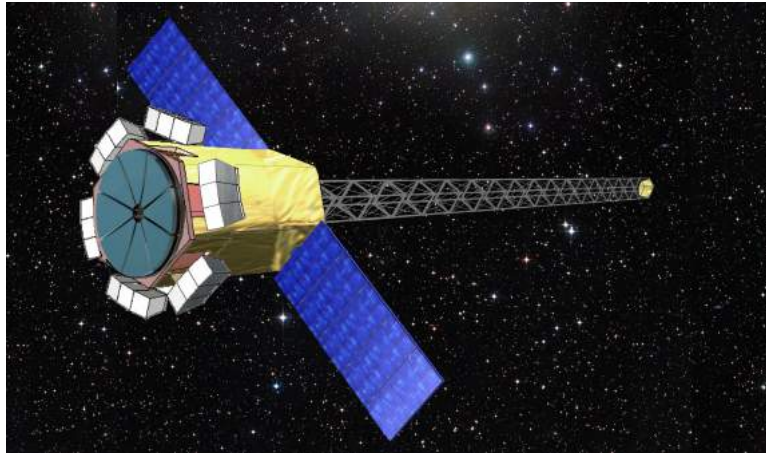
Figure 1: a) Drawing of the ASTENA concept mission where are visible the 6 grey modules, each module is composed by 3 units. b) concept of the Narrow Field Telescope based on a large collecting area Laue lens (see text for further details).

to soft-medium gamma-ray range were encouraged. Within the WP9 the Science Advisory Group (SAG) has identified the most important open issues to be addressed in the top-priority science themes that resulted to be Gamma-Ray Bursts and Nuclear Astrophysics. The ASTENA mission concept is one of the selected mission design to be further developed as one of the possibly proposed next generation of gamma-ray observatory. The ASTENA mission concept, is composed by two instruments, a Wide Field Monitor Imager and Spectrometer (WFM-IS) and a Narrow Field Telescope (NFT). Depending on their particular configuration, the two instruments are partially coaligned.

The WFM-IS which is sensitive to the 1 keV - 20 MeV energy pass-band, is made by 18 detector units bundled in 6 modules and each module is composed by 3 units. Within a module the three units are misaligned by 60 degrees to increase the Field of View (FoV) of the instrument that is larger than 1 sr. The full detection area is 1.8 m^2. Each detector consist of an array of long bars of scintillator with very small cross section, and readout from both sides with solid state thin detectors (e.g. Silicon Drift Detectors, SDD). One of the SDD is used as soft X-ray Position Sensitive Detector. A possible crystal material is CsI(Tl), but also other faster crystals such as LSO(Ce) or CeBr3 are being examined. The detector modules are coupled to a light coded mask, for obtaining a GRB localization accuracy of order of 1 arcmin between 1 and 30/50 keV.

The NFT, which is sensitive in the energy range 50 - 700 keV, is a full pass-band focusing optics based on diffraction from bent Germanium and Silicon crystals in transmission configuration (Laue lens). The 30 × 10 mm^2 large crystals are assembled in concentric rings with an extemely packed filling factor of 0.87. Thanks to the wide diameter of 3 m and to a focal length of 20 m, the optics has an extremely large geometric area 7 m^2 even with a moderate weight of 120 kg. The NFT is coupled to a high efficiency (>80% above 600 keV) focal plane position sensitive detector, with 3D spatial resolution of at least 300 μm in the (X,Y) plane and fine spectroscopic response (1% @511 keV) and with polarization sensitivity.

The general picture of the ASTENA mission is shown in Fig. 1. The ASTENA main body is essentially a 5 m long hollow prism shape with exhagonal basis. On one side of the main payload body is placed the NFT optics. At launch configuration the 18 WFM-IS units are arranged within the payoad envelope in such a way that in the operational phase they are slide out externally from each corresponding opening made in the payoad main body. Also the focal plane detector of the NFT is stored at launch in the main ASTENA body. With an extendable boom the focal plane detector can be positioned 15 meters far from the basis of the central body without the need of separate spacecraft for reaching the nominal focal length of 20 m from the Laue lens.

The performance of a gamma-ray observatory strongly depends on the chosen orbit. To ensure a low background level, as well proven by previous X-ray missions the equatorial Low Earth Orbit (LEO) is foreseen for the ASTENA spacecraft. A previous study on the expected background for a Laue lens based mission has been presented [15] .

The ASTENA mission benefits from the lightweight of the Laue lens as focusing device for the NFT and of the compactness of the WFM-IS modules. Such properties make ASTENA an ideal candidate for the ESA Medium Size Mission, given the imposed limits on the payload weight and size for this class of missions. Both NFT and WFM-IS are fully conceived and being developed within our collaboration.

2   Science with ASTENA

As mentioned earlier, one of key astrophysical question that have lead the design of the ASTENA mission is the decennial research and still not completely understood phenomena that originates GRBs. The interest in this field has increased even more recently when the relation between short GRBs and gravitational waves has been established. With the WFM/S, we will have a powerful tool to search for electromagnetic counterparts of Gravitational Wave events. Furthermore, thanks to the unprecedent total geometric area of the WFM-IS we expect to accurately determine the energy spectrum of GRB prompt emission in the broadest band ever achieved with a single instrument and to measure the gamma-ray polarization of at least the brightest GRBs. In addition, thanks to the mentioned scintillator bars and fast electronics, the Lorentz invariance for the brightest events can be tested. At the same time, with the coaligned NFT which is at least 100 times more sensitive at a few hundred keV than any other past, present or planned mission, we can perform for the first time a long-sought study of the afterglow spectrum of GRBs up to high energies (600/700 keV), including its polarization level.

Even with the improvement of efficiency and angular resolution of the instrumentation available for the observations, nuclear astrophysics is still strewn with unanswered questions. For instance, despite 30 years of theoretical and observational investigation, the main sources of positrons that originates the 511 keV annihilation line have not been identified yet, also due to the high propagation distance that positrons can travel from their production sites, making difficult to infer the source distribution from the observed map of 511 keV emission. Nevertheless, thanks to the high angular resolution of the WFM-IS (about 20") an unprecedent tool will be available to establish whether the 511 keV e^+/e^-

annihilation line is due to the superposition of emission from point-like sources or, on the contrary, it is due to a diffuse emission.

Beside the mentioned primary scientific key points, ASTENA will also cover different topics of Legacy Science. In the still poorly explored ASTENA energy passband a number of questions still remain unanswered. Among them, the nature of the hard emission tails of magnetars (already detected with INTE-GRAL) is still unidentified. Such excess which is present in both Anomalous X-ray Pulsars and Soft Gamma-Ray Repeaters need more sensitive observations, also capable to determine more accurately the cut-off energy that must be be present at few hundreds of keV.

Concerning Blazars, their total energy output is often dominated by the high-energy emission in X-rays and gamma-rays. The spectral energy distribution (SED) of these rapidly variable sources displays two characteristic broad humps, one peaking between infrared (IR) and X-ray frequencies and the other between the X-ray and Gamma-ray energy bands. It is quite clear that the low-energy hump is attributed to the synchrotron process of relativistic electrons while the high-energy peak is associated with the inverse Compton (IC) scattering of low-energy photons by relativistic electrons. Nevertheless, especially the region of the spectrum where the two components intercept eachother is poorly covered by observation due to the lack of sensitivity of current instruments. The unprecedented sensitivity of the NFT will contribute to better describe this part of their spectra.

One crucial aspect is the determination of the sources that give rise to the diffuse gamma-ray background (DGRB) above 100 MeV. For example, one could determine the high-energy cutoff from spectra of relatively bright AGN and study how this depends on the physics of the accretion (e.g. BH mass, Eddington ratio). We emphasize that the unprecedented sensitivity of the NFT below 1 MeV coupled with the large total collection area of the WFM-IS sensitive at higher energies will provide a large discovery potential never reached so far.

3 Narrow Field Telescope study

3.1 Introduction

Instruments on board past and present missions like *Beppo*SAX and INTE-GRAL have demonstrated the importance of the X–ray broad band (0.1–200 keV and beyond) observations to study a large number of astronomical phenomena. Nevertheless, their weak point is that they do not have focusing capability therefore a limit in their minimum detectable flux is given by their geometric area which cannot exceeds reasonable dimensions. Indeed, the increase of the sensitivity by a factor of ~ 3 can be obtained only if the collecting area is increased tenfold, with a consequent increase in terms of payload weight and, more importantly, of the detector noise.

Focusing telescopes overcome this limitation, thanks to the physical decoupling between collecting and sensitive areas. As the detector noise is roughly proportional to its volume, it turns out that focusing telescopes represent a key tool with which to maximize the signal-to-noise ratio. It has been shown that focusing telescopes in the 60–600 keV energy band could overcome the sensitivity limits of the current generation of non focusing gamma–ray telescopes [9, 22]

by a factor $\sim$10–100.

The soft X-ray energy band ($\sim$0.2–80 keV) has already took advantage of the focusing concepts through the employement of multilayer coatings (NuS-TAR [14]). Future attempts are those of enhancing this technology to push the limit ahead to focus photons up to few hundreds of keVs. Unfortunately, to date there is not a solid technology that would allow the realization of a focusing Gamma-ray mission with analogues performances to that of low and medium energy instrumentation. On the other hand, hard X-rays can be focused through the Bragg diffraction by crystals in transmission configuration. This methodology known as Laue lenses is now beeing developed and demonstrated with prototypes for focusing both broad and narrow energy bands. The main advantages with Laue lenses are those of both covering large collecting areas and allowing a reduced Point Spread Function (PSF) wich both allow to dramatically increese the sensitivity of current non focusing instruments of orders of magnitudes.

Another aspect of key importance is the possibility for an instrument to perform polarimetric measurements. To date, celestial X and gamma-ray source have been mainly observed through spectral, spatial, and temporal measurements. Nevertheless polarimetry, which is a still unexplored field in the hard X-/soft gamma-ray pass-band, represents an important window that can give important information about the emission geometry and the structure of the magnetic field around a variety of X and gamma-ray sources.

For this reasons, the next generation of space instruments are expected to acquire polarimetric information together with that provided by standard analysis. Two reasons make polarimetry a still unexplored field. On one hand, only few percent of the radiation is expected to be polarized for the large part of the surces of interest. On the other hand the principles over which high energy polarimetry is based requires detection and image reconstruction technologies which are still under development even if new technological solution are now expendable.

3.2 Design of the NFT

As a focusing instrument, the ASTENA/NFT consists of two devices, the Laue lens optics, which represents the collecting area, and the focal plane detector unit. Due to the instrument focal length, they are physically separated, therefore the design of the NFT entails the optimization of both the instruments and their coupling. In spite of their separation, both the collecting area and the detection unit features strongly define the NFT performances.

The NFT FoV set constraints on the size of the crystals composing the Laue optics (virgilli et al. 2018 in prep.) as well as on the detector size. The NFT energy pass band also constrain the type of crystals, the Laue lens inner/outer radius and focal length as well as the detector technology, design and thickness in order to optimize its efficiency. Our approach to the NFT opimization consists of a first phase where a dedicated software is used for the Laue lens definition, starting from the NFT requirements. Next, also taking into account the output from the Laue lens optics, a model of spectro-imager focal plane detector was developed. In Tab. 1 the properties of the NFT optics and focal plane detector are reported. In the following sections the different phases of the optimization are described.

Optics	Substrate	Quartz glass
	Frame	Invar
	Pass-band	$50-700$ keV
	Focal length	20 m
	R_{in}/R_{out}	18/149 cm
	Crystals specimen	Si (111), Ge (220)
	Crystals size	30 mm $\times$ 10 mm (optimized thickness)
	Number of rings	48
	Filling factor	87%
	Total geometric area	69800 cm^2
Focal plane detector	Detection type/technology	CZT strip detector
	Detector unit dimension	20×20 mm^2
	Number of detector units	4
	Efficiency	80% @ 700 keV
	Spatial resolution	300 μm (x, y, z)
	Energy resolution	1% @ 511 keV

Table 1: Parameters of the NFT optics and focal plane detector on board AS-TENA.

3.3 Laue optics

The NFT is designed to operate in the $50-700$ keV energy pass-band. To this end, crystals made with Silicon and Germanium have been chosen to diffract the lower part of the pass-band ($\sim 50-200$ keV) and its higher fraction (~ 200 - 700 keV), respectively. In the boundary region the two specimen coexist in order to provide a more smooth effective area. Even if the technology to obtain bent crystals is to date limited to the thickness of 3 mm, in the simulations the thickness of the crystals has been optimized to their maximum efficiency, that depends on the energy pass-band to which is targeted.

Thanks to the 20 m long focal length, the large collecting area (impressive geometric area of ~ 7 m^2) and a narrow FoV (fw arminutes), the NFT is an ideal instrument for high sensitive and deep field observations of known sources with unprecedent capability in terms of angular resolution (better than 30" 500 keV). The NFT optics diameter is designed to be within the limit imposed by the common available launchers like the Proton-Medium vehicles allowing payload fairing with a diameter of 4.35 meters (and recently introduced new fairing 5.2 meters wide) or SpaceX Falcon 9 launch vehicles whose housing allows a payload dynamic envelope with a maximum diameter of 4.6 m. Thanks to the light weight of the Laue lens optics also the mass limits are well under any launcher restrictions.

The Laue lens optics has been designed and optimized with a simulation software named Laue Lenses Library (LLL). The LLL has been extensively described elsewhere, therefore we olny report its main features. At first the main Laue lens properties have to be defined (inner and outer radius, focal length, energy passband). Secondly, the crystal properties are set (crystal size, material, diffraction planes). A new feature of the software is the possibility to chose between flat or bent, perfect or mosaic crystals. In particular, within the ASTENA/NFT bent crystals have beed preferred, due to their capability of focusing the radiation into a detector area smaller than the crystals size itself with a significant improvement in terms of Point Spread Function (PSF) and

eventually on the Laue lens sensitivity. After the definition of both the optics properties and the source of radiation, the interaction between them occurs through the diffractions laws. The output of the software are mainly the Field of View (FoV) of the lens, its sensitivity, and the PSF as function of the energy and of the source off-axis angle. In the optimization process we also included all the factors that can potentially worsen the performances of the optics. They are mainly related to the quality of the optics which is made by a number of crystals. These factors can be summarized as follow:

1. accuracy in the realization of the optical components;

2. accuracy in the optical components assembly.

Concerning the first source of uncertainty, in order for the PSF to be minimized, the curvature radius of the crystals needs to be equal to the double of the focal length. Differently, the radiation will result to be out of focus and at the nominal focal distance the radiation will be spread in a larger area with a consequently broader PSF. The second source of uncertainty concerns the accuracy in the assembly process. The simulation of the nominal PSF obtained with the complete NFT in the full operative passband 50 - 700 keV is shown in Fig. 2 (a) together with the mentioned cases of crystals with curvature radius with a gaussian distribution around the nominal value and with a FWHM of 6 m that corresponds to a 15% uncertainty, and crystals with nominal curvature radius of 40 m affected by mounting uncertainty with gaussian distribution (centered at zero misalignment and with FWHM = 15"). The two cases are labeled with b and c, respectively.
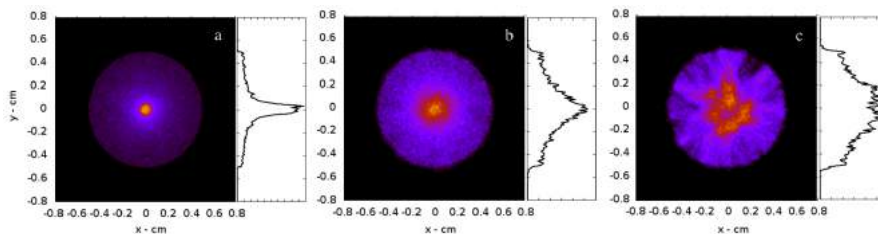
Figure 2: Simulation of the PSF for the NFT (full energy pass-band 50 - 700 keV) in the following operative conditions: a) all the crystals with nominal curvature radii of 40 m and nominal mounting accuracy (no uncertainties in the production and assembling phase). b) crystals curvature radii with a gaussian distribution around the nominal value (FWHM$_{radial}$ = 6 m) and with nominal assembly. c) crystals with ideal curvature radii and with a gaussian distribution in the misalignment around the ideal position of each crystal (FWHM$_{misal}$ = 15").

3.4   Focal plane detector

In order to exploit the throughput of the Laue optics, the focal plane detector must have high efficiency in the working pass band. One of the most important key features to be defined for a focal plane detector coupled with Laue lenses is its collecting area. Unfortunately Laue lenses work as concentrators and is affected by off-axis aberrations therefore off-axis sources result in PSF spread

over larger areas than that for sources placed on-axis. Moreover, as the source off-axis angle increases, the signal to noise ratio dramatically decrases. This behaviour influences the choice of the detector area, that eventually limits also the FoV of the instrument. Another key point that rules the definition of the focal plane detector is the thickness of the sensitive material, on which the instrument efficiency depends. As reported in Tab. 1 the requested efficiency is 80% at 700 keV which is the most demanding requirement.
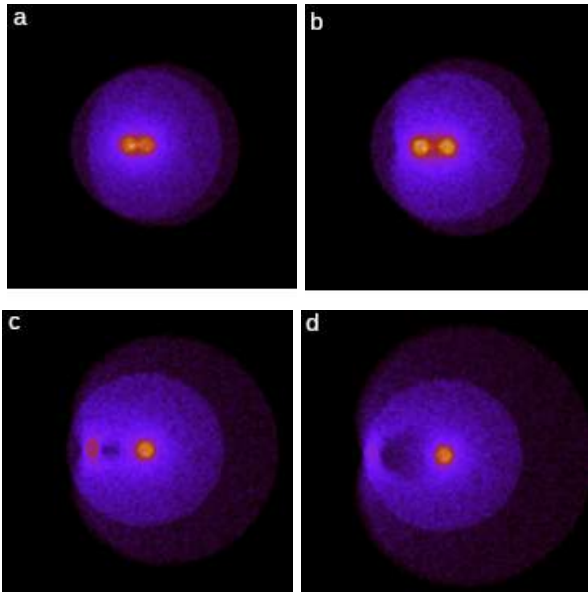
Figure 3: Simultaneous simulation of two separated polychromatic point sources, one on-axis and the second positioned with increasing off-axis angle: a) 0.4 arcmin, b) 0.8 arcmin, c)1.4 arcmin, d) 1.8 arcmin. The degradation of the quality of the image is apparent as the off-axis angle increase. The simulation is made with 10^5 impinging photons and the output is measured with a detector whose size is 20×20 mm^2.

Optimization study of focal plane detector coupled with Laue lenses have already been made (e.g. [1]). Recently, double sided strip solid state detectors [15] have been proposed. In this case, Germanium and Silicon have been compared even if the efficiency for Silicon was found to be limited at 54% at the upper energy limit, therefore Germanium resulted a better solution. Simulation were performed using both MEGAlib toolkit [28] for the geometry definition and the SILVACO utility to define the required full depletion voltage and to minimize the detector noise. Nevertheless, the use of germanium in space under optimal conditions may be a limiting factor, therefore for the NFT on board ASTENA a model based on the technology that has been conceived and realized at DTU - Space [16] is being evaluated. The technology is based on the Cadmium Zinc Telluride (CZT) Drift Strip detector principle that have been developed to detect high energy photons from few tens of keV up to $\sim$ 1 MeV therefore are ideal detector for Laue lens based instruments. The main advantage of using CZT is that, in spite of their limited polarimetric capability, especially at low energies ($<$ 150 keV) they are available at room temperature, differently from the aforementioned semiconductors. Furthermore, the developed technology of 3D CZT Drift Strip detectors offer imaging capability with sub-millimetric res-

olution in all the 3 spatial directions [4] . For the first prototype detectors CZT 20 mm × 20 mm, 5 mm thick crystals were used.

It can be demonstrate that the physical dimensions of the crystals composing the Laue lens influence its FoV. While the dimension along the curvature does not affect the FoV, the smaller is the non focusing dimension of a crystal, the sharper is the resulting PSF. On the contrary, smaller crystal dimensions increase their number to cover the optics surface, with evident constructive problems. We have evaluated a trade off between the different aspects and crystal with cross section of 30×10 mm^2 result in a good filling factor with a moderate number of crystals and with a reasonable FoV. Using the above mentioned crystal dimensions, in Fig. 3 is shown the response of the full Laue lens of the NFT at two polychromatic point source, one on axis, and the second off-axis by 0.4, 0.8, 1.4, 1.8 arcminutes. As expected, the PSF progressively worsen as the off-axis angle increases. It has been evaluated that, 1.8 arcmin represents the limit angle over which the signal to noise (interpret as the peak level) is equal to 3, therefore 3.6 arcmin is the evaluated FoV of the NFT in the mentioned configuration.

It is worth noting that the polarimetric capability which is under study in the case of Laue lenses optics like the one which is equipped the NFT, will work for on axis sources, i.e. when the photons (on first approximation) converges in a single point over the detector, from the multiple sites where the radiation is diffracted by the crystals. On the contrary, for off-axis source, the signal is spreads over a larger size area and the symmetry is broken. Nevertheless the Compton reconstruction technique would allow the reconstruction of the original source direction.

To improve the polarimetric capability at low energies, we have considered a model made with a number of CZT layers surrounded with a stack of double-sided silicon strip detector (DSSD). For the detector design we have used the Geomega library within the MEGAlib toolkit. Free parameters of the model are the number of layers, their thickness, the interspace between the layers for both the CZT and the DSSD. These parameters are being optimized according to the required efficiency at 700 keV.

3.5   Experimental support to the ASTENA/NFT

Past and ongoing work of the ASTENA team is now focused on experimental tests and computer simulation on the main components of the mission concept with the goal of increase and strengthen the TRL of all the involved technologies. To date, the readiness level of the Laue technology is of the order of 3. In the recent past, laboratory prototypes have been realized and successfully tested ([10, 23, 2]) with different levels of accuracy in the crystals selection and mounting accuracy. One test on balloon have been made so far[13, 26] proving that the technique is practicable outside the on ground laboratory environment even if more steps forward in different aspects of the technology are highly desirable (optics accuracy and efficiency, thermal stability). Recently, a new activity supported by the National Institute of Astrophysics INAF and the Italian Space Agency has been started with the goal of increasing its technology readiness level (TRL) to 5-6. The activity is guided by the Physics and Earth Department of the University of Ferrara in the LARIX facility, with the fundamental contribution from the other two partners INAF-Bologna and IMEM/CNR-Parma.

Within this project the main goal is to realize a laue lens module which is made by a number of sub-modules. Such strategy, which has been demonstrated to be winning in other proposed or accepted missions will help in terms of integration time and positioning accuracy.

It is also though to benefit from a modular design which is highly recommended for mass production. Both the properties contribute to achieve the unprecedented telescope collecting area.

In Fig. 4 is shown the modular concept for the Laue lens. Each petal of Laue lens is made of a number of sub-modules. Each module host few tens of crystals. Thanks to the alignment method and the gluing procedure adopted the obtained accuracy per each single crystal is of the order of 10-15 arcsec. The main advantages of adopting this methods is that each module can be realized in a considerably short time and the small size makes the mounting accuracy
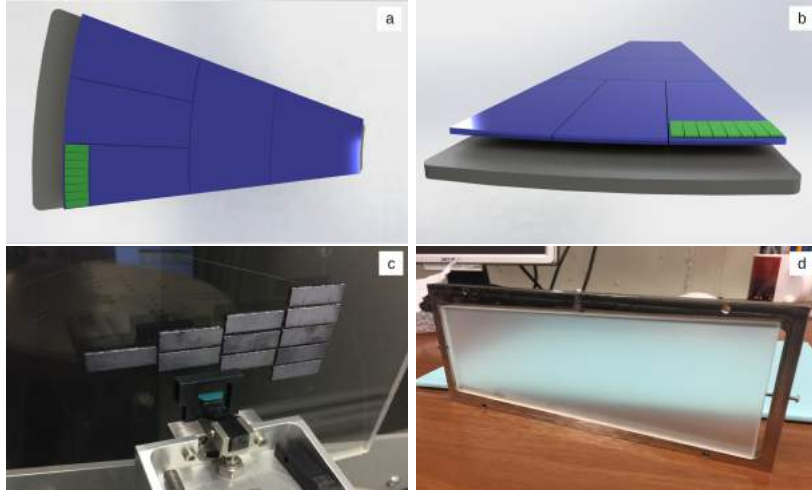
Figure 4: Rendering of a fraction of Laue lens named petal (a) and (b). Each petal is made of a number of sub-modules to exploit the modular concept that would increase the accuracy of the overall Laue lens assembly. One module have been realized with a transparent substrate consisting of 11 GaAs crystals with the goal to demonstrate the alignment capability and the long term stability (c). After 5 days the alignment of the crystals were measured and the discrepancy with respect to the nominal alignment was within 30 arcsec. The goal is to reduce such discrepancy of a factor 3 by using more stable materials and different fixing methods of the crystals on the substrate (d).

The ASTENA mission concept is at an advanced stage of development and also an expansive experimental activity is supporting this idea with the goal to to demonstrate its feasibility in a reasonable short time. New ideas devoted to improve the assembly method and to the realization of a new generation of diffractive crystals are being evaluated. Concerning the first point, a modular approach is being investigated. In this context, a number of sub-petal each one housing few tens of crystals and later the sub-modules are assembled and oriented to the main focal point. Thanks to this implementation on small scale we expect to improve the crystal mounting accuracy.

As already pointed out the quality of the crystals represents a crucial aspect to obtain a satisfactory PSF. Nevertheless, also cylindrically bent crystals are physically limited by their capability of focusing the radiation in one direction,
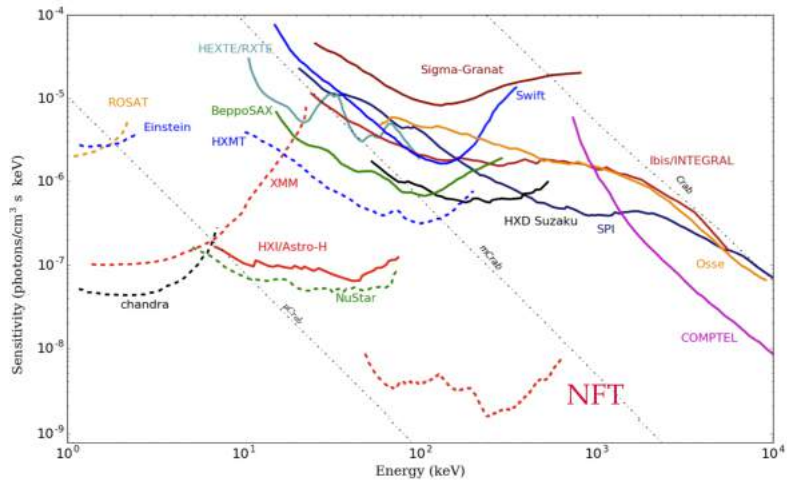
Figure 5: Expected sensitivity for the NFT (red dashed curve) compared with other past and present both focusing and non focusing mission operative in the energy from 1 keV to 10 MeV. All the curves are determined with an exposure time of 10^5 s and calculated at 3 σ confidence level with an energy bin size of E = E/2.

but no focusing effect is expected in the perpendicular direction. Hence, each crystal produces a diffracted image which has rectangular shape whose height depends on the crystals dimension in the not-focusing direction while the width of the diffracted signal (which is of the order of 1 mm) depends on the crystal mosaicity and thickness. To overcome this limit, a new crystal configuration is being evaluated using a bunch of Silicon 111 crystals that are specifically worked for this end. The method is now under investigation at LARIX facility of the University of Ferrara in collaboration with the Italian Space Agency and the National Institute of Nuclear Physics and the first results are expected by the end of this year.

4   Sources of uncertainty in the realization of the Narrow Field Telescope

Focusing optics based on Laue lenses represent a challenging system to focus the radiation from the hard X and soft Gamma-ray sky. The use of bent crystals represent a compelling expedient to enable the capability of focusing the radiation in a region smaller than the crystal size itself and consequently offering the possibility to reduce the Point Spread Function size to few tens of arcseconds for a focusing instrument with at most 20 m focal length. Such important feature would lead to a significant step forward compared with current Gamma-ray instruments. Such a big leap in terms of point spread function size would be effective only if the technology level would guarantee high rely on the crystal realization/preparation and high accuracy in the crystal tile assembly. The crystals curvature, for instance, represents a very important feature for the PSF minimization, therefore it needs to be achieved through a reliable and ma-

11

Figure 6: Simplified drawings of a flat mosaic crystal (a) and a bent mosaic crystal (b). In the former case the mean average planes have the same direction along the perpendicular to the crystal surface while in the latter case they continuously change along the curvature direction. Such feature is the reason that induces the focusing effect.

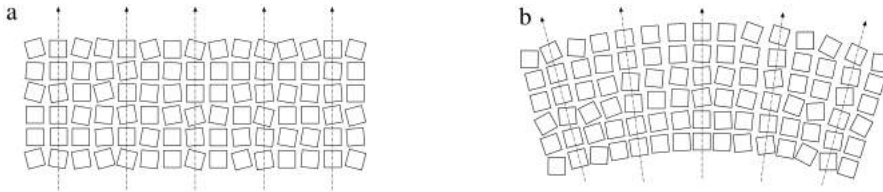ture technology. On the other side, a fast and precise method to set and orient a large number of crystal tile in a reasonable short time is also a challenging task. The distortion of the photon distribution on the focal plane detector due to the effects of crystal misalignment and radial distortion with respect to the nominal curvature are discussed. The photon distribution on the lens focal plane has been investigated analytically, with Monte Carlo simulations with the support of the experimental tests performed at LARIX facility. For the Monte Carlo we have made use of the laue lens library LLL that has been developed for these purposes and recently integrated with the features capable to simulate the discussed sources of uncertainties.

We have discussed the effects of the so called mosaic defocusing and its relation with the curvature radius of the adopted crystals. We have found that a radial distortion within 10% of the nominal curvature radius does not affect the crystal PSF. We have discussed also the distortion of the PSF in some of the available crystals and we have proposed an explanation for its appearance. We also show through experimental tests the achieved accuracy assembling a module of Laue lens and the alignment stability on days time scales. The different technologies that are involved in the Laue lens method has in recent years reached different maturity levels. In this paper we face two aspects: the realization of proper bent crystals in terms of curvature stability and uniformity, and the alignment capability.

4.1 Introduction

Astronomical sources in the X and Gamma ray domain are very faint, thus to acquire information from them we need to collect light by using optical systems capable to concentrate photons. Furthermore, the dominant background makes the collection and the observation of these sources more difficult. Laue lenses are futuristic instruments capable to enable imaging in Gamma-ray Astronomy. Observations in the sub-MeV domain, particularly with high angular resolution, would help to distinguish between diffuse emission candidates and point sources of these excesses. Several attempts have been made to realize effective geometries and also with combined methods (including coded masks, or Compton telescopes) (e.g. [12]) that offer angular resolution of few arcminutes.

Focusing the radiation is the best way to improve the angular resolution and consequently the sensitivity of an instrument with respect to non focusing devices. Nevertheless, the penetration power of the hard X-rays and soft

Gamma-rays is so effective that, so far, the only effective method to concentrate them is to define a smart geometry exploiting the diffraction from crystal lattice. Flat crystals have been largely studied and used for a number of demonstration models [23] or flying prototypes [13] with promising results. Nevertheless, flat crystals have at least two evident limits: their PSF has the same dimensions of the crystal cross section and the critical effect called *mosaic defocusing*, induced by the crystal mosaicity β [17]. Thus, a lens made of crystals with cross section of a few cm^2 will be limited by a PSF of a similar area, with loss of sensitivity due to the extremely broad PSF.

In an upgraded version of the Laue lenses challenge named LAUE project [11, 24], cylindrical bent mosaic and perfect crystals have been selected as basic elements for the diffraction process. Their particular configuration allows the focusing effect to be present along one of the two directions (the curvature direction) while, as expected, the same effect is not present along the perpendicular direction. A bent crystal is then itself a concentrator with a significant advantage, given that, under specific conditions, the PSF can be smaller than the crystal cross section, although for bent mosaic crystals the mosaic defocusing effect is still necessarily present. While on one side the reduction of the PSF dimensions represents a remarkable advantage making each single crystal a powerful focusing device for Gamma-rays, on the other side the curvature radius must be obtained with high accuracy in order to fully take advantage of such a property. Preliminary attempts to realize crystals with spherical curvature are very promising and are under development ([1]). Their employment would dramatically increase the crystals focusing power, being capable to overtake the limit imposed by the cylindrical curvature.

Bent mosaic and perfect crystals can be obtained trough a large variety of methods [21]. For instance, mechanical clamps directly applied to the crystals are the most straightforward method to generate a bent lattice structure. Nevertheless, for Laue lenses used as astrophysical concentrators, additional mechanical parts applied to each crystal would increase the device weight, its complexity and the opacity to the radiation, therefore this does not represent the most suitable solution. One method that have reached a mature technological readiness is the surface lapping procedure ([8, 6]) finely implemented at IMEM–Parma (Italy), and successfully applied to Gallium Arsenide (GaAs) mosaic crystals. The process consists on a controlled surface damage induced on one of the crystal main surfaces and such uniform strength steadily bend the crystal. The amount of induced curvature has been experimentally related to the surface working time, to the grain of the lapping machine and to the thickness of the crystals. The lapping procedure can be combined with an etching process that is used to decrease an excess of curvature, so that the two methods can be combined in order to tune the curvature radius of a sample at the desired curvature radius. Bent GaAs crystals with a mosaic spread of 10-15 arcsec and crystallite size of $\sim$ 50-100 μm are good candidates for the realization of Laue lenses. Thanks to their good reflectivity (30-35%), with an optimized thickness for each energy pass-band they can be successfully employed from few tens up to hundreds of keV. Efficiency of flat mosaic and perfect crystals has been studied and their behaviour have been extensively theoretically explained and confirmed with experimental tests (i.e. [27]). In particular, for bent perfect crystals, it has been demonstrated ([3]) that for some crystallographic orientations of the diffraction planes the efficiency can overcome the limit of the 50% efficiency

13

exhibited by flat crystals, due to continuous change of the incidence angle of an x-ray trajectory with the crystalline planes, reaching even 80-90% of the incident beam. On the other hand, is still debated whether or not the efficiency of a bent mosaic crystal is expected or not to overcome the crystal efficiency of the equivalent flat crystal. Some author found a possible linear correlation between curvature and efficiency in both perfect and mosaic crystals ([5]). Nevertheless, such results must be taken carefully given that is also reasonable to suppose that the mosaic crystal structure is though as an agglomerate of not-deformable microcrystals, therefore while for a flat crystal the mean average plane does not change along the crystal surface, the bending process would changes continuously the crystallite average direction along the curvature direction (Fig. 6) and not the punctual efficiency that depends only on the structure of the perfect micro-crystals.

Goal of this work is to compare the performances of a nominal Laue lens with that of real Laue lens made of bent mosaic crystals, affected from the main sources of aberration that will be discussed in Sect. 4.2. To qualify the lens performances the main tool is the Point Spread Function (PSF) and the Half Power Diameter (HPD). After the qualification of each crystal tile in terms of curvature radius and its deviation from the nominal value, the PSF of a nominally mounted lens will be presented. In the last section we will present the simulated PSF of the entire Laue lens with both the radii distribution and the achieved mounting accuracy taken into account.

4.2 Sources of aberration in a Laue lens

Each optical system suffer from various kind of aberrations. One effect involves different performances of the optical system depending on the interacting radiation wavelength. Other effects are strictly related to the imperfection or to the inhomogeneity of the optical system itself. As general rule, which is valid for each optical system at any wavelength, the realization of a first order model of the optics is followed by a description through analytic treatise and/or ray tracing simulations of the interaction between radiation and optics. Finally, some figure of merit is defined and some interplay parameters are introduced in order to minimize the aberrations and to optimize the optics performances. For bent mosaic crystals the first order of aberration is the so called *mosaic defocusing*. Indeed the photon are not focused towards a single focal point and the spread of the image mainly depends on the mosaicity of the crystals, i.e. the angular spread of the crystallite distribution with respect to their most probable orientation. On one side a large value for the mosaicity increases the crystal diffraction efficiency and contributes to the crystal pass-band, but also increases the photon spread over the focal plane. On the other side, a small mosaicity value results in a sharp point spread function, but with reduced efficiency. Through appropriate experimental conditions, the mosaicity is a parameter that can be controlled during the growing process even though some degree of uncertainty can be present.

Although some of the methods capable to induce a self-sanding curvature have reached a mature technological readiness ([3, 6, 7]), the crystal curvature radius can deviate from its desired value. This inaccuracy and/or not homogeneity of the crystal curvature represents another source of aberration. At first order approximation, in the following discussion we will treat the crystals as

perfectly cylindrically bent. Within this assumption only the mismatch of the curvature radius from its nominal value has been considered, rather than the inhomogeneity of its curvature along the crystal. Hereafter we call this effect *radial distortion*. The unavoidable presence of the radial distortion produces a degradation of the final PSF given that each crystal will not focus at its proper focal point.

As will be pointed out in Sect. 4.6, while the crystal curvature distortion consists of a larger or smaller curvature radius with respect to the nominal value, the *focusing inhomogeneity* represents a worsening contribution that consists of a different focusing behaviour along the crystals non-focusing direction. The non-uniformity of the PSF have been experimentally identified and analytically quantified. Furthermore, for some diffracted images, it has been found that the PSF FWHM changes along the PSF path that results irregularly wider in some region and narrower in some other.

Another crucial source of aberration is due to the incorrect orientation of the crystals once they are set to diffract a fraction of the incident x-ray beam at a given focal distance. The main difference between this source of aberration and those previously discussed is that in the latter case the aberration are intrinsically related to the crystal structure, while in the former case the aberration is due to the cumulative effect of setting the crystals over a common substrate, with a certain degree of mounting accuracy. The overall effect on the point spread function given by the superposition of the diffracted signals can be evaluated only through Monte Carlo methods given the large number of crystals composing a full Laue lens. The Monte Carlo simulations are performed using a specific software written in Python named Laue Lens Library. The code (that is extensively described in [25]) allows to include in the simulations the radial discrepancy and the crystal mounting uncertainties with both uniform or Gaussian distribution. Nevertheless, the mentioned contributions named *focusing inhomogeneity* and irregularity have not been included in the simulations tools yet.

4.3 Crystal sample

A sample of 60 GaAs crystal tiles with cross section of 30×10 mm^2 and 2 mm thick have been grown and cut in order to exploit the diffraction from the (220) planes. Next, the tiles were bent through a surface lapping process that introduces defects in a superficial layer of few tens of microns, generating a highly compressive strain capable to self sustain the curvature. All the experimental processes have been done at the Istituto Materiali per Elettronica e Magnetismo IMEM-CNR (Parma). The crystals were qualified at the LARIX facility in terms of mosaicity and curvature radius and the results were consistent with those found during the characterization phase made at IMEM-CNR. Among the 60 prepared crystals, a bunch of 11 randomly taken crystals have been used to realize a mock-up of Laue lenses to test the capability in the assembly procedure.

4.4 Crystals position accuracy

The spatial position of a crystal is defined by the x, y and z coordinates of its center of mass and by its orientation defined by three angular coordinates around the principal axes of the crystal (ϕ, α and θ respectively around x, y and

z). As already pointed out elsewhere [25], two out of the three orientation angles (θ and ϕ) need to be accurately set in order to position properly the diffracted beam at the focal point. The variation of the third angle α does not affect significantly the position of the diffracted image on the focal plane detector. Moreover, the effects of ϕ scales with the radial position of the crystal (which is of the order of ~1-2 meters) in comparison with the effects generated by θ which scale with the focal length (in the present case 20 meters). Therefore it results that the latter effect on the position of the diffracted image is at least one order of magnitude larger then the former. Each crystal is properly positioned and oriented through a high precision robotic device, while the X-ray beam impinges on its surface. As mentioned earlier, the positioning process produce random aberration effects due to the concurrent presence of a bunch of crystal tiles. Each crystal need to be oriented through an external device and next fixed over a common substrate. After the release from the device, the angular misalignment with respect to the desired position, are recorded. By fitting the x and y profiles of the diffracted image with a generalized flat-top Gaussian (Eq. 7, its centroid is determined with an accuracy which is one order of magnitude better than the focal plane detector spatial resolution (200 μm), therefore each diffracted image is properly oriented within a fraction of arcsec. Once the centroid of the diffracted image from the crystal is correctly positioned, the crystal is bonded on a substrate and the mechanical clamp release it. In the condition free from angular uncertainties the centroid of the signal generated by each single crystal coincides with the reference focal point of the Laue lens. In real conditions, the centroid of the diffracted signal is generally shifted by a quantity ΔX along the X axis and ΔY along the Y axis due to the positioning uncertainties mainly originated from the bonding process. The above quantities are easily related to the angular misalignments with the following relations:

$$\theta = \frac{\Delta X}{2F} \phi = \frac{\Delta Y}{r} \ , \tag{1}$$

where F is the focal distance and r is the distance between the center of the crystal and the lens axis. The accuracy for both the mechanical rotation angles is about 1 arcsec. In order to evaluate the assembly accuracy and the long term stability of the assembly procedure, 11 crystal tiles were preliminary positioned and fixed as mock-up model of Laue lens. The arrangement procedure, the details of the method employed and the materials used for the substrate are being submitted for patenting. The crystal position accuracy with respect to their nominal position were evaluated after 7 days from the assembly, by recording a pair of uncertainty angles (θ_i, ϕ_i) for each crystal. In Fig. 11 is shown the distribution of misalignment θ and ϕ with respect to each crystal nominal position for the full sample. The measured values of θ cover the interval [-5 arcsec, +18 arcsec] while the measured values of ϕ cover the interval [-10 arcsec, +15 arcsec]. Among the 11 crystals, 10 suffer from a positive θ angle, suggesting a possible systematic uncertainty due to some effect ascribable to the critical process of bonding the crystal over the common substrate. On the other hand, for the distribution of the ϕ angles, a clear systematic effect is less evident. Statistical analysis have been performed on both θ and ϕ in order to better qualify the spread on both the angles. The process of fixing each crystal over the substrate is independent from a crystal to another and a large number
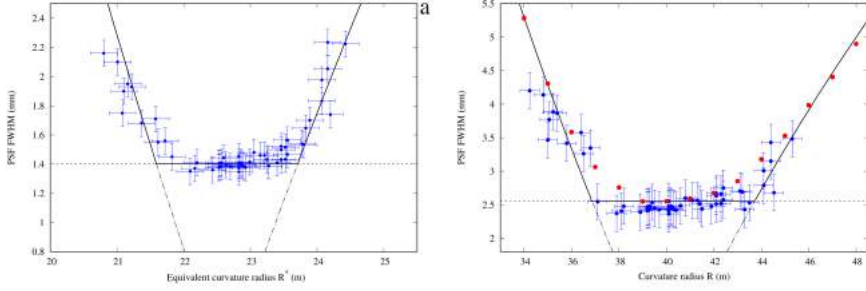
Figure 7: Effects of the radial deformations on the PSF FWHM of a single crystal. Blue points represent the measured PSF FWHM for the 60 available crystals performed at LARIX facility. Data are plotted as function of the equivalent radius of the crystals. The nominal radius of the crystals is 40 m, therefore, according to Eq. 6, the equivalent nominal radius is 22.7 m. Dot-dashed line represents the dependence of the FWHM PSF from the radial deformation (Eq. 4). Dashed line corresponds to the mosaicity contribution (Eq. 3). Solid line represents the overall effect of the two contribution, according to Eq. 5. Radial deformation effects contribution to the PSF FWHM in the astrophysical condition. Black dot-dashed line shows the contribution of the radial deformation, black dashed line is the constant contribution due to the crystal mosaicity, black solid line shows the overall effect on the PSF. Blue points, which are the same of Fig. 7 but conveniently scaled using Eq. 3, 4 and 6 represent the measured PSF FWHM if the crystals would have been used in astrophysical conditions. Red points, obtained from Monte Carlo simulations, confirm the overall behaviour even if some discrepancy to the analytic model are evident.

of independent factors contribute separately to the process result (amount of adhesive per crystal, adhesive polymerization shrinkage, environmental temperature variation, mechanical uncertainty during the crystal positioning phase), therefore it is reasonable to suppose that for a large number of crystals both the uncertainties follow a Gaussian distribution. We estimated the mean value of both positioning error as the average of the measured misalignment angles. We obtained:

$$\langle \theta \rangle = 11" \pm 2" \qquad \langle \phi \rangle = 4" \pm 1" \qquad (2)$$

Since the limited number of crystals, instead of using the variance measured from the data, we estimated a confidence interval for the value of the Gaussian variance, σ_θ and σ_ϕ, of both misalignment distributions. To estimate this interval, we took in account the fact that the standard deviation of a set of data follows a χ^2 distribution, with a number of degree of freedom equal to the number of data. We evaluated the three intervals for σ_θ and σ_ϕ at 90%, 95% and 99% confidence level and the results are presented in Tab. 2. For the discussion given in Sect. 4.7 we have adopted the 95% confidence level which is the most commonly used level, nevertheless, for a more conservative approach, the upper limits for both the intervals have been used to estimate the cumulative PSF FWHM.

17

Table 2: Confidence intervals for σ_θ and σ_ϕ.

Confidence level	interval for σ_θ [arcsec]	interval for σ_ϕ [arcsec]
90%	4.7 ¡ σ ¡ 9.8	7.5 ¡ σ ¡ 15.7
95%	4.5 ¡ σ ¡ 10.7	7.1 ¡ σ ¡ 17.2
99%	4.0 ¡ σ ¡ 12.9	6.5 ¡ σ ¡ 20.8

4.5 Crystal curvature deformation

For no curvature distortions, the diffracted signal is focused in one region whose extension in the focusing direction depends on the mosaic defocusing, which is proportional to the crystal mosaicity. We call this enlargement, with a *quasi* gaussian shape, FWHM$_\beta$. For geometrical considerations it can be demonstrated that this contribution is given by:

$$FWHM_\beta = 2 \; \beta \; F + \delta_w \; F \qquad (3)$$

where δ_w is the Darwin width of a crystal, β is its mosaicity and F is the focal length of the Laue lens. Nevertheless, the FWHM$_\beta$ of the PSF depends slightly on other crystal parameters (microblock thickness, thickness of the crystal, diffracted energy), therefore Eq. 3 is valid only on first order approximation. On the other hand, a further defocusing effect occurs when the curvature radius of the crystals differs from R$_N$. The deviation of the crystals curvature radii with respect to the nominal value enlarges the PSF at the lens nominal focal point. From the geometric relation F = R/2, where F is the focal length and R is the radius of curvature of the crystals, it results that a variation of the radius ΔR from its nominal value corresponds to a variation of ΔF = ΔR/2 of the focal length. In fact, in the cases R ¿ R$_N$ or R ¡ R$_N$, if the detector is placed at the nominal focal distance F$_N$ = R$_N$/2, the FWHM will be enlarged according to the expression already presented in [25]:

$$FWHM_R = \alpha \; |F_N - F| = \frac{d_0}{F} \; |F_N - F| = \frac{d_0}{R} \; |R_N - R| \; , \qquad (4)$$

where α is the angle subtended the crystal length d$_0$, which is the dimension along the curvature direction, at the focal distance F. If the defocusing given by the radial distortion is smaller than the one due to the mosaic defocusing, the latter effect dominates the PSF enlargement. On the opposite case, the radial deformation prevails on the mosaic defocusing. The FWHM expression can be therefore written as follows:

$$FWHM = Max \left\{ FWHM_\beta, \; FWHM_{\Delta R} \right\} . \qquad (5)$$

It is worth noting that the above discussion is valid in the astrophysical case (i.e. when the source impinges the crystal as parallel beam from infinite distance). For on-ground experiments, the crystal curvature radius R combines

with the divergence of the source, therefore its focal distance is reduced [25]. Nevertheless, it can be demonstrate that the same focal distance can be equivalently obtained if an infinitely distant source impinges on a crystal with an equivalent curvature radius R* given by:

$$R^* = \frac{2 \ S_d \ R}{R + 2 \ S_d} \ , \tag{6}$$

where S_d is the source-target distance. With this assumption the condition of infinitely far source is restored and Eq. 5 is still valid. Figure 7 describes and confirms the previous explanation. Blue points represents experimental measurements of the PSF FWHM for the full sample of GaAs crystals in the specific LARIX set-up (source-target distance = 26.5 m). Due to a not perfect uniformity of the diffracted image (especially for some crystal tile), the PSF FWHM for each crystal has been estimated by averaging the value along the non focusing direction.

The results excellently agree with the analytic curve given by Eq. 4 if the equivalent radius R*, calculated for each crystal, is used instead of the curvature radius R. Moreover, the flat portion of the data, that corresponds to a minimum value of the PSF FWHM of 1.43±0.02 mm, can be fitted with the model given by Eq. 3, whose free parameter is β = 12.9 arcsec. Such value represents an estimate of the average mosaicity for the full sample[1].

The estimated mosaicity is an intrinsic parameter of the sample, independent of the crystal curvature radius, deformation or source distance, therefore it has been used to evaluate the PSF FWHM in astrophysical conditions that resulted to be $\sim$ 2.55 mm (determined through Eq. 3). As can be observed in Fig. 7(right), the intersection between the dashed and the dot-dashed lines define the limits of the deformation radius as $R_{min} \sim$ 36.8 m and $R_{max} \sim$ 43.7 m which correspond to a tolerance for the crystal radius of +8% – -9.2% around the nominal curvature radius of 40 m. Radial deformations within such limits will provide worsening effects on the PSF that are hidden by the mosaic defocusing, while crystals with curvature radius outside of this interval display a PSF FWHM dominated by the radial discrepancy with respect to the desired curvature radius therefore must be discarded. Nevertheless, a conservative approach suggest to shrink this interval to a tolerance of ± 5%. The experimental results (blue points), extrapolated from the measured data as if they were acquired with the detector placed at the nominal focal distance of 20 m and impinged from an infinitely far source, agree with the analytic expression. The Laue Lens Library estimations (red points) qualitatively confirm through Monte Carlo simulations the previous result even if there is some discrepancy between analytic model and Monte Carlo simulations particularly at the interception between the two curves given by Eq. 4 and 3. For both experimental data and Monte Carlo simulations, the PSF FWHM of the diffracted signals from each crystal have been estimated using the following flat-top generalized normal distribution function:

$$t(x) = A \ e^{-\left(\frac{|x-x_0|}{\alpha}\right)^\gamma} \ , \tag{7}$$

---

[1]being the crystals belonging to a single ingot of material it is likely to suppose that they present the same mosaicity, except for statistical fluctuations of that parameter along the ingot.
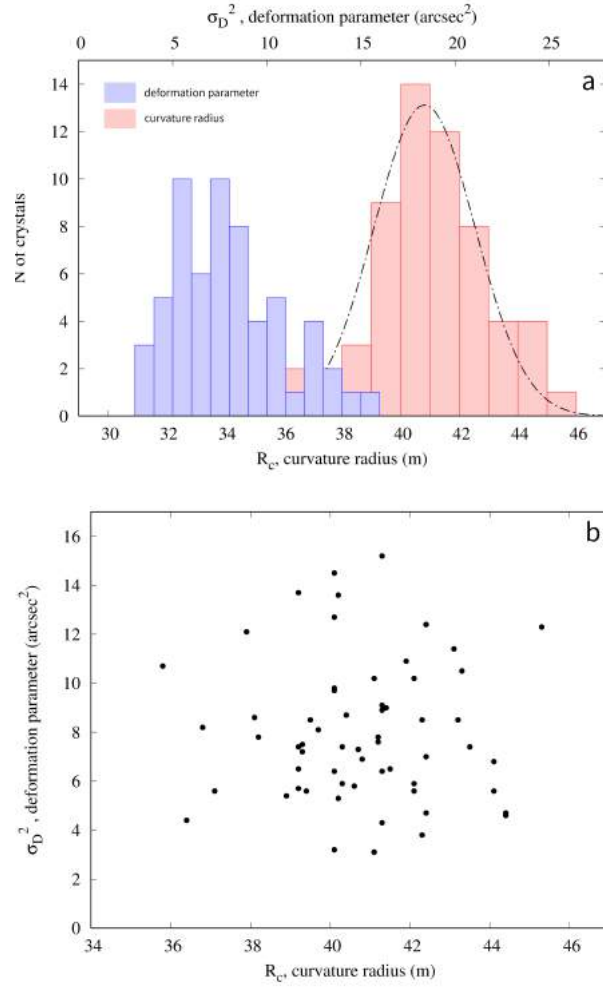
Figure 8: $a)$: Distribution of the curvature radii for the full sample of 60 GaAs crystals provided by IMEM-CNR/Parma (red histogram) available for building the Laue lens prototype. The value of the curvature radius is supposed to be distributed with a Gaussian profile and the best fit gives the values of $R_c = 40.4$ m with a FWHM$_R = 4.93$ m. In the same plot is also shown the distribution of deformation parameter (blue histogram) whose average vale is 7.9 arcsec^2 (see text for the definition of deformation parameter). $b)$: Plot of the deformation parameter D as a function of the crystal curvature radius. There is not evidence of correlation between the two parameters, i.e. the bending process is not the responsible of the dis-uniformity but, more likely, each crystal exhibit a degree of deformation already present at the growing phase.

where A is a normalization factor, x$_0$ is the centroid of the function, γ is a real positive number ($\gamma = 2$ corresponds to the normal distribution while the more γ increases, the flatter results the top of the function) and α is related to the FWHM through the relation:

20

$$FWHM = 2 \ \alpha \ \sqrt[\eta]{-ln(1/2)} \ . \tag{8}$$

4.6   Twisted focalization

Even if a crystal own the nominal curvature radius, other aspects, related to its intrinsic uniformity, influence the Laue lens PSF. One of them is exemplified with the sketch shown in Fig. 9.
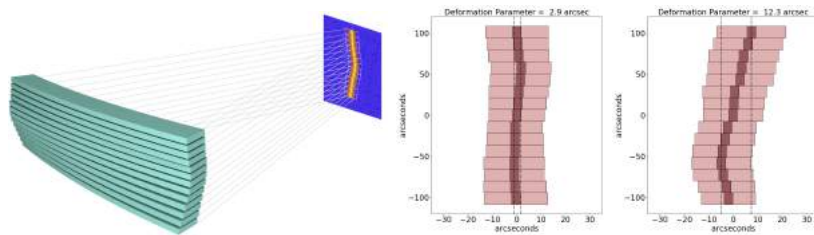

Figure 9: *Left*: Illustration of the distortion effect in bent crystals that is ideally divided into multiple thin slices. Each slice focus the radiation in a region slightly shifted with respect to each other. *Right*: diffracted images discretized in 15 layers. The profile 1 is quite close to the straight line also confirmed by the value of the deformation parameter which is under the detector pixel size (200 μm $\sim$ 3.6 arcsec.). This accuracy is allowed by the gaussian fit that is performed on each layer to determine the mean value. On the other side, for the profile 2 is evidently deformed with respect to the ideal vertical shape and the parameter shows a very large value. In both the images are also shown the minimum and the maximum values for the deviation, whose difference is the deformation parameter (vertical black dot-dashed line).

Some crystal tile exhibit a twisted diffracted image that contributes to the overall Laue lens PSF worsening. Such effect can be easily explained if each crystal is though made of a large number of thin layers. Each crystal layer is supposed to be slightly tilted around the vertical axis therefore is mis-oriented with respect to the other layers. With this exemplified picture, although each layer diffract the radiation at the proper focal distance and with the expected diffracted width, each diffracted slice is slightly shifted on the focal plane detector with respect to the ideal position. Such effect can occur if the overall crystal does not have a perfect cylindrical curvature due to a torsion effect that can be originated from the growing process, or, more likely, from the mechanical process used to bend the crystal. It is worth stressing that, in this simplified picture, the curvature radius is correctly impressed to each imaginary layer of the crystal. The level of deformation due to the above process has been quantified for each crystal by splitting each diffracted image in 15 layers. Each layer has been fitted with a flat-top generalized Gaussian function (as seen in Eq. 7). The difference between the minimum and maximum values among the peaks (named *deformation parameter D*) was taken as reference value of PSF deformation. The number of layers is a trade off between a sufficient number of collected diffracted photons for each layer (i.e. good count statistics) and the width of the layer itself. It is clear that the more the D parameter is close to zero, the

21

more the measured PSF overlaps with the ideal performances. In Fig. 9, are also two examples of discretized diffracted images. The pink rectangle represents the FWHM of the PSF while the red area represents the detector pixel in which the signal shows the maximum intensity for each given layer. As can be observed one of them shows a deformation parameter of 2.9 arcsec while for the second crystal its value is 26.4 arcseconds.

Both the distribution of the curvature radii deviation and the deformation parameter have been analyzed for the whole sample of 60 crystals and the results are reported in Fig. 8. A Gaussian function has been used to fit the curvature radii distribution data with a reduced χ_r^2 of 0.6. The best fit parameters give an average radius of 40.4 ± 0.3 m and a standard deviation $\sigma = 2.1 \pm 0.2$ m that corresponds to a FWHM of $\pm 6.1\%$ of the average curvature radius. Although this value exceeds the acceptance limit of $\pm 5\%$ established in Sect. 4.5, it is still below the critical limit of $40^{+8.0\%}_{-9.2\%}$ previously discussed. These value indicate that the supplier institute hold a sufficient accuracy in the manufacturing processes of bending the crystals, even if some improvement are desirable.
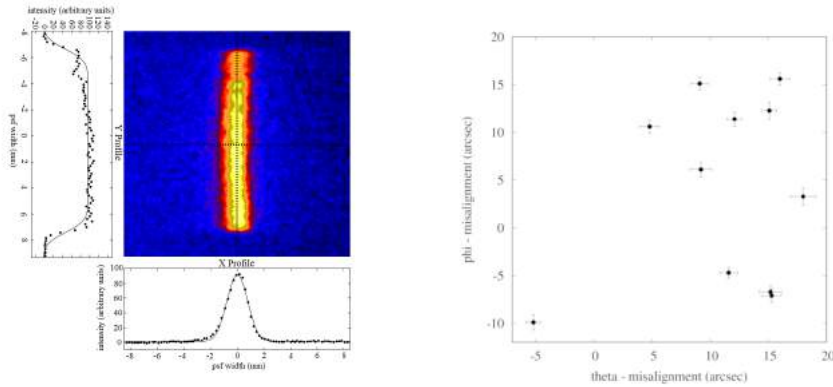

Figure 10: Diffracted image from a bent GaAs crystal (centroid energy pass-band ∼140 keV) measured at the nominal focal distance. The x and y profiles with the best fit functions (see text for details) are also shown.

Figure 11: Distribution of the θ_i and ϕ_i misalignment angles with respect to the ideal positioning for the 11 GaAs (220) bent mosaic crystals aligned and set over the common frame. No correlation has been found between the two misalignment angles.

Specific discussion must be done for the crystal deformation. Such effect further contributes to worsen the PSF of the full Laue lens. For the measured sample, its distribution is shown in the blue histogram of Fig. 8a. As can be observed, the deformation parameter is distributed over a wide range of values around the average of 5.4 arcsec. The deformation parameter can be used as quality factor for the crystal production. In order to discern between crystals with undue deformation (to be discarded) and crystals sufficiently not-deformed, a limit on this deformation parameter must be set. This limit can be defined on the crystal shape itself as well as on the basis of the overall Laue lens PSF which is the sum of thousands of diffracted images. The second approach requires Monte Carlo simulations in order to generate a large number of crystal with increasing deformation parameter. The value that makes the PSF

HPD larger than a given value (defined *a priori*) is the allowed limit for the deformation parameter. Such feature is not available yet in our Laue lens library software and will be implemented in the next version of the code. The former approach instead is based on the comparison between the effects caused by this deformation, with the comparable image deterioration associated with the crystal alignment capability. Indeed, it is reasonable to suppose the deformation of the same order of magnitude of the positioning accuracy on θ of the diffracted image as presented in Sect. 4.4. The value of 95% is reasonably acceptable and the value of 10 arcsec has been chosen as limit. As can be observed in Fig. 8b, no correlation has been found between curvature radius and deformation parameter indicating that either the crystal warp is already present before the bending process, or the surface lapping induces the crystal deformation depending on some hidden parameter that has been not yet identified.

As previously mentioned, another second order worsening effect on the PSF, which has been observed in some crystals, can be associated with a significant non-uniformity in the value of the mosaicity. Indeed, in an ideal mosaic crystal, the mosaicity is supposed to be uniform all over the volume of the crystal. On the contrary, in real crystal its value can be uneven and vary from point to point. Since the width of the PSF linearly depends on the mosaicity (Eq. 3), if a slice of the crystal shows a punctual mosaicity different from the average mosaicity, its diffracted image produced by this slice will be stretched or compressed with respect to that given by the non deformed part of the crystal. Such condition is also visible in the diffracted profile of Fig. 9 where each pink rectangle corresponds to the FWHM of the respective diffracted image. Further investigations are needed to confirm such hypothesis and to ascribe this behaviour exclusively to the not uniform mosaic crystal structure or, instead, to involve other parameters (e.g. the bending process). Additional information are also needed to quantify the degree of inhomogeneity of the mosaicity within the crystal volume.

4.7 Nominal PSF and uncertainties affected PSF of a full Laue lens

It is reasonable to suppose that for the realization of an entire Laue lens made of thousands of crystals, the discussed parameters will have a comparable distribution in terms of deviation from the nominal curvature radius and mounting uncertainty as those discussed previously. Therefore, we have used the previous results as input for the Laue Lens Library and evaluate the performances of a Laue lens affected from the previously mentioned issues. A Laue lens made of 16719 bent GaAs crystals with size $30 \times 10 \times 2$ mm, arranged in 39 concentric rings has been simulated working in the energy pass-band 90-700 keV with 20 m focal length. Concerning the deviation with respect the nominal curvature radius, the average value of 40.4 m has been used in the simulations, supposing that their curvature radius follow a Gaussian distribution with $\sigma = 2.1$ m. Concerning the angular deviation, the results presented in Sect. 4.4 have been used as input in the Monte Carlo code. We have considered for θ and ϕ the mean values $\langle\theta\rangle = 11$" and $\langle\phi\rangle = 4$", respectively. A Gaussian distribution around the mean value have been considered for both the angles and the worst case corresponding to the 95% confidence level among those presented in Tab. 2 has been chosen ($\sigma_\theta = 10.7$" and $\sigma_\phi = 17.2$").

First, the case of nominal Laue lens PSF has been simulated. In this instance, all the crystals have been generated with the same mosaicity $\beta = 12.9$ arcsec whose value was obtained from the discussion given in Sect. 4.3. Furthermore, all the crystals have been simulated with the proper curvature radius of 40 m and without taking into account any alignment uncertainty with respect to the respective nominal position and orientation. The nominal PSF for the full Laue lens obtained in these conditions is shown in Fig. 4.7 a. For comparison, if the radial mismatch and the crystals positioning uncertainties are introduced with the values previously estimated, the PSF broadens as in Fig. 4.7 b. Also in this second case the mosaicity for all the crystals was set to the nominal value of 12.9 arcsec. The radial profiles for both the mentioned cases are shown in Fig. 4.7 c from which are evident the differences in terms of collected photons in the central part of the image. We have evaluated the FWHM of the overall PSF in the two distinct set of data. In the nominal case (black filled circles) the PSF FWHM have been obtained fitting the whole set of data with a generalized Gaussian and it results to be 3.8 mm, while it reduces to ~ 3.2 mm if the fit interval is restricted to the range [-0.5 cm; +0.5 cm]. If a box function is summed to the generalized Gaussian function the fit further improves and the FWHM reduces to ~ 3.1 mm. A flat top Gaussian was used to fit the set of data obtained by introducing the uncertainties, and the value for the PSF FWHM resulted to be 11.2 mm, which is around 3.6 mm times broader than that obtained in the nominal conditions. It is evident that the most limiting factor on the PSF are the mean values imposed for both θ and ϕ, which behave as systematic errors. It is also confirmed that if the curvature radius suffer from an uncertainty which is within the minimum and maximum limits determined in Sect. 4.5 the effects on the PSF are negligible.
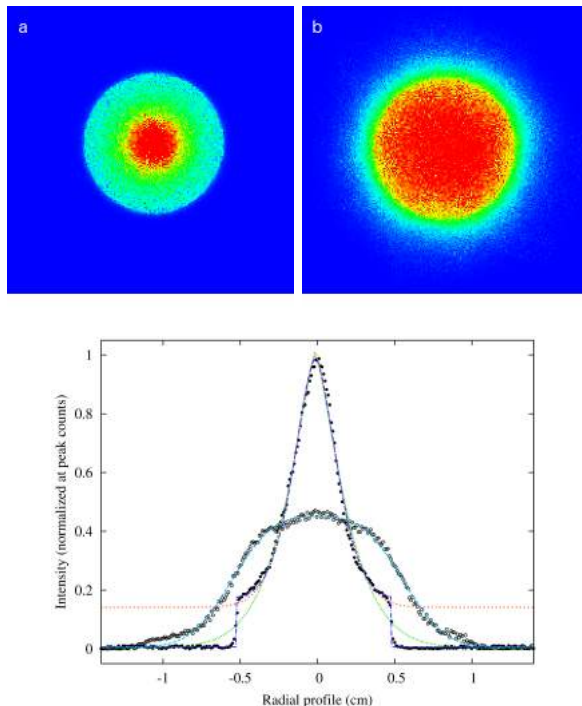
Figure 12: Simulated PSFs obtained for a full Laue lens sensitive to the broad energy band 90-700 keV made with 16719 bent GaAs crystals with size 30 × 10 × 2 mm, arranged in 39 concentric rings. *a*) Nominal case with crystals perfectly bent with 40 m curvature radius and nominally arranged/aligned. (*b*): simulated PSF obtained taking into account the worsening factors discussed discussed in the text: Gaussian distribution of the curvature radii of the crystals, with average value of 40.4 m and standard deviation equal to 2.1 m. 2; Gaussian distribution of the misalignment angle θ, with an average value of 11 arcsec and standard deviation of 10.7 arcsec; Gaussian distribution of the misalignment angle ϕ, with an average value of 4 arcsec and standard deviation of 17.2 arcsec. Both the images have been obtained by generating 10^6 incident photons distributed uniformly in the energy pass-band of the Lens and impinging evenly on the Laue lens surface. (*c*): Radial profile for the nominal case (black filled points) and for the case that includes the discussed uncertainties (open circles). The former data set has been fitted with three functions: a single generalized Gaussian used to fit the whole set of data (green curve), a generalized Gaussian plus constant that fit only the interval [-0.5 cm; 0.5 cm] (orange curve) and a sum of a box function with the generalized Gaussian (blue curve). The three best fit gives a value for the PSF FWHM equal to 3.8 mm, 3.2 mm, 3.1 mm, respectively. The latter data set has been fitted with a generalized Gaussian (PSF FWHM = 11.2 mm).

4.8   Discussion and conclusions

In this paper we have discussed the most relevant aspects that influence the Laue lens PSF shape and width. For what concerns the PSF FWHM we have compared analytic expressions with experimental results and Monte Carlo simu-

25

lations. Through experimental characterization, we have investigated the effect of the crystal curvature radius deviation from the nominal value on the distribution of the photons on the focal plane detector for a Laue lens made with bent crystals. In particular, we have focused our discussion on bent mosaic crystals made of GaAs(220) with 30×10 mm^2 cross section and 2 mm thick, that are available at the LARIX facility of the University of Ferrara (Italy).

The crystal bending radius and its deviation from the requested crystal curvature are crucial factors that largely influences the photons distribution on the focal plane. While the bending process induces a focusing effect that shrinks the signal provided by a single crystal tile under the crystal cross section itself, the mosaic structure generates the so called mosaic defocusing that acts broadening the PSF with respect to that of a perfect crystal. On the other side, if the curvature radius suffers from a mismatch with respect to the nominal value the resulting effect is a defocused image. In a sense, the two effect play a comparable role of broadening the crystal PSF and their effects are of the same order of magnitude.

From an analytic treatise, supported also by Monte Carlo simulations and experimental evaluation we have found a method to determine the average value of the mosaicity $\beta = 12.9$ arcsec of a sample of crystals. If the crystals belong to the same ingot as in the case presented in this paper, it is reasonable to suppose that such value is a good estimate of the mosaicity of each single crystal tile. For such value of the mosaicity and for a nominal curvature radius of 40 m the mosaic defocusing effects hide the PSF broadening due to the inaccurate curvature radius if the bending process is accurate within 8-9% of the nominal curvature radius. This condition release the constraint of providing crystals with exact curvature radius. On the other side, the smaller is the size of the crystals, the more strict is the constraints on the bending process.

Another aspect that have been considered is the presence of twisted branches in the PSF of each single crystal with respect to the conjectured straight pattern. Experimental characterization have confirmed that a significant fraction of the full sample suffers from this sort of defects. Such deformation represents a further source of PSF broadening for the Laue lens PSF. The deformation has been estimated for each crystal that is imagined made of a number of thin slices slightly tilted one from another, due to some kind of induced strain. The amount of the deformation has been determined by introducing the so called *deformation parameter D* which is given by the difference between the maximum and the minimum values obtained by fitting each slice of the diffracted signal with a generalized Gaussian profile. No correlation has been found between the deformation parameter and the curvature radius induced to the crystals. This lack of correlation suggests that either a hidden parameter controls such behaviour, or the deformation exist independently from the induced curvature and is due to some effect that is connected to the crystal growing phase. The average value of 7.9 arcsec^2 for the deformation parameter of the full bunch of available crystals is above the acceptable limit imposed by the goal of the projects therefore further investigation must be done in order to find the reasons that produces such defects with the goal of reducing this imperfection and minimize the number of crystal tiles that must be rejected due to these shortcomings.

Experimental tests have been made to quantify the assembly accuracy of the crystal sample. Eleven crystals have been used to realize a test model by

setting each of them at their nominal position to the substrate in the best operative conditions obtained so far in our LARIX facility. Based on the measured positioning capability, Monte Carlo simulations have been made by including as input parameters the obtained angular uncertainties for a Laue lens made with 16719 bent mosaic crystals distributed in 38 concentric rings and working in the 50 - 700 keV energy pass-band. A realistic distribution of the photons on the focal plane detector have been obtained for a full Laue lens and compared with the same distribution in case of no uncertainties.

The main reason that led the assembly of a limited number of crystals over a dedicated substrate is the commonly accepted advantages given by the modular approach to the technology realization, as demonstrated by other already tested or planned mission like NuSTAR ([14]) or Athena ([19, 18]). Indeed, the modular philosophy is favorably accepted for optical systems that can be subdivided into many equal components, allowing both the realization in small size laboratories, and the qualification test of each separated unit instead of a monolithic device. Furthermore the modular philosophy benefits from a high Technology Readiness Level (TRL) and is highly amenable for mass production, which is necessary to achieve a large collecting area as the Laue lens presented in this work. Recently, supported by the agreement ASI/INAF a project have been approved with the goal of improving the TRL for the Laue lens methodology. In this view, a Laue lens is made of petals and each petal is made of Laue lens modules (LLM). Each LLM consists of a reasonable number of crystals (few tens). A number of LLM are being realized and qualified through environmental stresses such as vibration tests and temperature/humidity cycles. Finally, the LLM need to be co-aligned to the focal point through a set of three actuators installed on each module.

5 Wide Field Monitor study

5.1 Introduction

Gamma-Ray Bursts (GRBs) are one of the most challenging phenomena in modern space sciences. These phenomena are characterized by both huge luminosities up to more than 1000 erg/s and very wide redshift distribution extending from very low z (0.01) up to z ¿ 9, and are associated with peculiar core-collapse supernovae and with neutron star/black-hole mergers. Therefore, their study is of very high interest for several fields of astrophysics. These include, e.g., the physics of matter in extreme conditions and plasma physics, black hole physics, core-collapse SNe, cosmology and fundamental physics as the production of gravitational wave signals. Despite the huge observational advances occurred in the last twenty years, several open issues still affect our comprehension of these phenomena, and their exploitation for the solution of fundamental physics and cosmological problems. [1–3] Among the most relevant aspects are all those connected with the so-called "prompt" emission. A better knowledge of both the emission processes and the source geometry is required, to clarify the origin of the "central engine" and its connection with the progenitors, and, furthermore, to assess the real energy budget involved in different classes of GRBs to use the GRBs observations for fundamental physics and cosmology studies. To address these fundamental issues, time resolved spectroscopy and possibly polarimetry of the GRB prompt emission over a broad energy range from few keV to up to

several MeVs are mandatory requirements for next generation of hard X and soft gamma-ray space instruments. In this perspective, the ASTENA mission concept [4] under study in the framework of the H2020 AHEAD project includes a wide field monitor and spectrometer (WFM/S), mainly dedicated to GRB science. The instrument is sensitive in the range 1 keV – 20 MeV and is composed of several independent detection units, having a total isotropic detection (i.e. exposed) area up to 3.0 m2 over a FOV larger than 1 sr. The WFM/S will allow the detection and both spectroscopic and polarimetric characterization of all classes of GRBs and other high-energy transients. Each module is a coded mask telescope that will allow the source localization within few arcmin up to above 50 keV. The detector core is based on the coupling of low-noise, solid-state Silicon Drift Detectors (SDDs) with CsI(Tl) scintillator bars, and low energy and high-energy photons are discriminated using the on-board electronics.

5.2 The WFM/S instruments

The heritage of the ASTENA WFM/S instruments belong to a design studied in the framework of the THESEUS ESA M5 proposal.
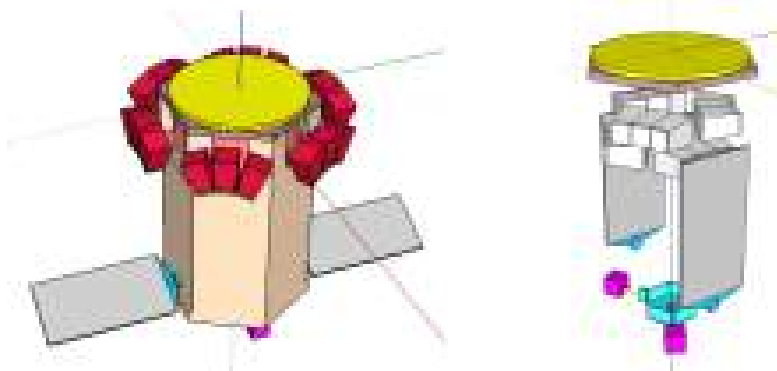

Figure 13: The WFM/S instrument (red volumes) on board the ASTENA satellite in deployed configuration; (b) The WFM/S instrument in launch configuration.

5.2.1 WFM/S Main Characteristics

The WFM/S comprises six blocks of three identical coded mask telescope units, called modules. In each block, the modules are pointed at offset directions in such a way that their FOVs partially overlap. Each module has imaging capabilities in the low energy band (2 to 50 keV) thanks to the presence of a coded mask placed above a position-sensitive detector. In the baseline configuration, the footprint of each WFM/S module is 50 x 50 x 85 cm^3, with a total mass of about 37 kg, requiring a power budget of about 30 W. Because of their configuration (Tab. 15), inside this energy band each module has an angular resolution of few arcmin over a partially coded field of view (FWHM) of 0.5 sr. A passive shield around the mechanical structure between the mask and the detector plane, as well as limiting the cosmic ray diffuse background in the low-energy band, will determine the FOV of each module for X-rays up to about 150 keV.

Above this energy and up to 20 MeV the WFM/S module has almost isotropic detection capabilities. WFM/S modules and the other instrument on-board ASTENA, the Laue-lens based telescope NFT, are partially coaxial, in order to guarantees that the NFT field of view is centred in the overall WFM/S FOV. Furthermore, ASTENA WFM/S can operate also as a scattering polarimeter, due to 3D imaging capability of the module detector planes.

5.2.2 WFM/S GRB's sensitivity

Using a reference background in a LEO orbit, Figure 14 shows the expected sensitivity of the ASTENA WFM/S in different energy bands as function of the GRB duration in seconds. This preliminary evaluation shows a sensitivity already at least an order of magnitude better with respect to currently proposed instrumentation (e.g. THESEUS) dedicated to GRB science.
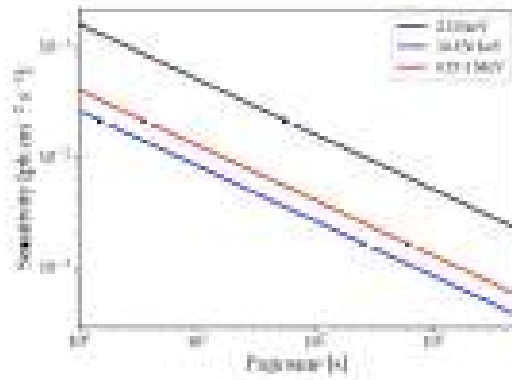

Figure 14: The ASTENA WFM/S evaluated 3 sigma sensitivity to GRB's as function of the measure time (exposure) in different energy band.

5.3 THE WFM/S SUBSYSTEMs

As stated before, the ASTENA WFM/S module is a heritage the THESEUS mission study. In the following sections, we provide a short description of both the main characteristic of each ASTENA WFM/S subsystems.

5.3.1 WFM/S Single coded mask telescope

The basic module of the WFM/S is a coded mask telescope that can provide imaging up to 50 keV in the current design inherited by the ESA M5 THE-SEUS proposal. In the ASTENA mission study, we will verify the opportunity and feasibility to extend this imaging capability up to 100 keV, minimizing the impact in the system complexity and resources requirements. The masks of each telescope will be designed individually, to minimize direction reconstruction ambiguities, and will be built with self-supporting random patterns to be optimized by using Monte Carlo simulations. Each WFM/S coded mask telescope have a passive shield (hopper) connecting the mask to the detector plane, made by graded layers of different materials to optimize the opacity up to 150

keV, limiting the cosmic X-ray background contribution on the detector. Furthermore, the hopper, limiting the telescope FOV up to 150 keV, would allow a rough location capability (several degrees) by comparing the detected counts over all the mask telescope units (see following subsections).

Mask Pattern	Random self-supporting
Element size	5×5 mm^2
Open fraction	30-50%
Dimension	50 cm × 50 cm
Mask-Detector Dist.	70 cm
Mask Material	Steel
Mask Thickness	0.5-1 mm
Hopper Material	W/Cu/Mo
Hopper thickness	1-1.5 mm

Figure 15: Main baseline characteristics of the ASTENA WFM/S coded mask telescope module.

5.3.2 WFM/S Block Unit

In the current ASTENA configuration shown in Fig. 13, the coded mask telescope modules are arranged in block units, placed around the NFT Laue lens instrument. Three coded mask telescope modules make each WFM/S block unit. The optical axis of the coded mask modules in the block unit are not coaxial, but the relative inclination (offset) between the optical axis of each coded mask module is optimized to maximize total FOV of the WFM/S, taking into account also the satellite bus constraints.
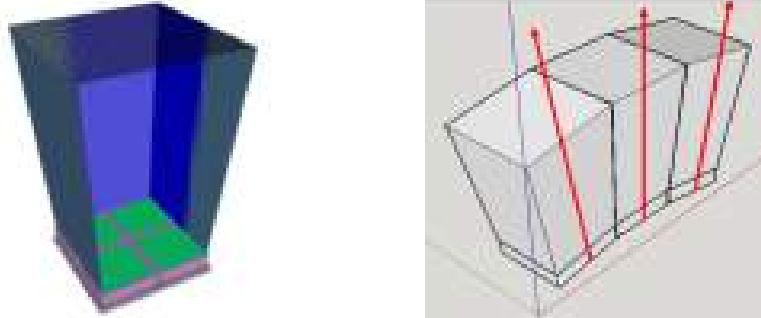

Figure 16: (a) The coded mask telescope module scheme that is the basic element of the ASTENA WFM/S in which are clearly visible the random mask on the top, the detection plane in the form of a 2 x 2 mosaic of CsI/SDD sensitive element arrays, and in between the hopper shield. (b) The schematic drawn of the block unit made by three coded mask modules. The red arrows show the optical axis of each module with their non-parallel directions.

5.3.3 WFM/S Block Field of View

Assuming ±20 degrees as the reciprocal offset of the optical axis of each module in the block unit, the WFM/S Block unit FOV at 100 has been analytically evaluated and it is shown in Fig. 17. The contour plot, left, shows the FOV as function of the exposed detector area percentage, while the plot on the right reports the angular profile of the response of each module hopper. The overall angular response of the block unit is the convolution of the single module response profile and is given by the superimposed red thick line. Since the current ASTENA implementation foresees 6-block unit distributed along the perimeter of a hexagonally shaped service module (one for each hexagon side), the overall FOV of the WFM/S is obtained by the superimposition of the single block FOV with each major axis rotated by 60 degrees. The total FOV (FWHM) is 1.35 sr, with a total exposed area of 3000 cm^2.
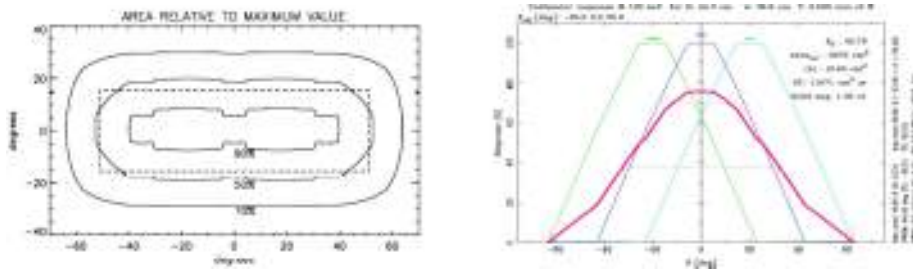

Figure 17: (a) The shape and the angular dimension of the ASTENA WFM/S block unit at 100 keV. Each contour line represent the FOV for corresponding to a given sensitive area exposure. (b) The profile of the hopper (or collimator) response versus the seeing angle of each coded mask module in a block unit. In red the overall angular profile response of the single WFM/S block unit.

5.3.4 WFM/S Mask Telescope Detector

A 2 x 2 mosaic of segmented detector modules constitutes the coded mask detector plane. Each detector module is an array of CsI(Tl) bars, each read out by two Silicon Drift Detectors (SDD) cells, placed at the two bar ends Fig. 18a. In turn, each array consists of basic sensitive units composed by 2 x 2 CsI(Tl)+SDD elements. The current design foresees the use of SDD cells with a sensitive area of 5 x 5 mm2 optically coupled with CsI(Tl) bars with the same cross-section and a length between 3 to 5 cm. Aiming at designing a compact instrument with a very wide sensitivity band, the detector module is based on the so-called siswich concept, exploiting the optical coupling of Silicon detectors with inorganic scintillator bars. As shown by the schematic in Figure 5b, the topmost SDD array acts as a low energy detector (LED), while the scintillator bar detector operates as a high energy detector (HED) with 3D spatial resolution capabilities. In this concept, the top SDD play the double role of read-out devices for the signal from the scintillator and of an independent low energy solid state X-ray detector. The two types of events are distinguished by techniques based on pulse shape discrimination, through the different rise times of the corresponding preamplifier signal. In the case of low energy X-ray events interacting in the SDD, the rise time is dominated by the anode collection time

31

(100 ns). For higher energy photons, interacting in the CsI(Tl) scintillator, the signal rises following the convolution of the characteristic CsI(Tl) scintillation de-excitation time constants and different light paths, amounting to an effective rise time of a few μs.
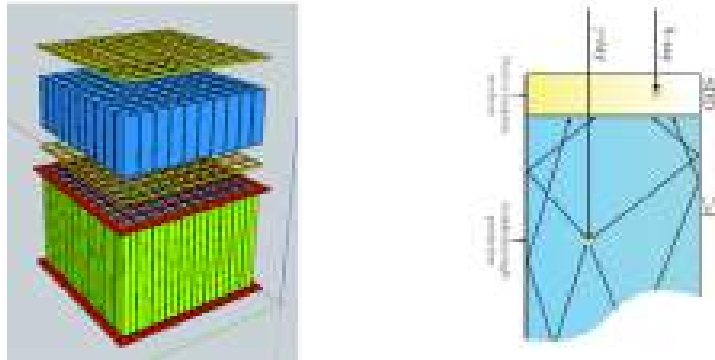

Figure 18: (a) The exploded view of the detector module: the yellow grids represent the support of the SDD that are optically coupled to the extremes of the CsI bars (blue array), the segmented green volume represent the associated front-end electronics. (b) The siswich read-out concept. Low energy X-ray (¡50 keV) are detected in the top SDD, while the hard X/soft gamma-rays (20 keV to 20 MeV) interact with higher probability inside the CsI bar generating optical photons that are readout by the two SDD coupled at each extreme.

Energy band	2 keV – 20 MeV
Module mosaic	2×2
Pixels/module	32×32
Sensitive area	256 cm^2
Pixel size/shape	5 mm/Square or Hexagonal
LED (2-50 keV)	SDD 450 μm thick
HED (20 keV-20 MeV)	CsI(Tl) 3 to 5 cm thick

Figure 19: The detector module main characteristics.

5.4   THE WFM/S DETECTOR PERFORMANCE

In order to demonstrate the validity of the proposed instrument architecture for the detector plane, a prototype is under development and it is currently in its characterization phase. The obtained experimental results have confirmed the feasibility and the expected performance of the proposed detector concept. In the following sections, we will give a summary of the achieved results.

5.4.1   Spectroscopic response of the Silicon Drift Detector units

The SDD are used for both soft X-ray detector and as CsI(Tl)-scintillator read-out. This capability is well evident from Figure 6, where two simultaneous spectra acquired by the top SDD with two radioactive sources are reported. Event generated by the 241Am source emission is directly detected by the SDD
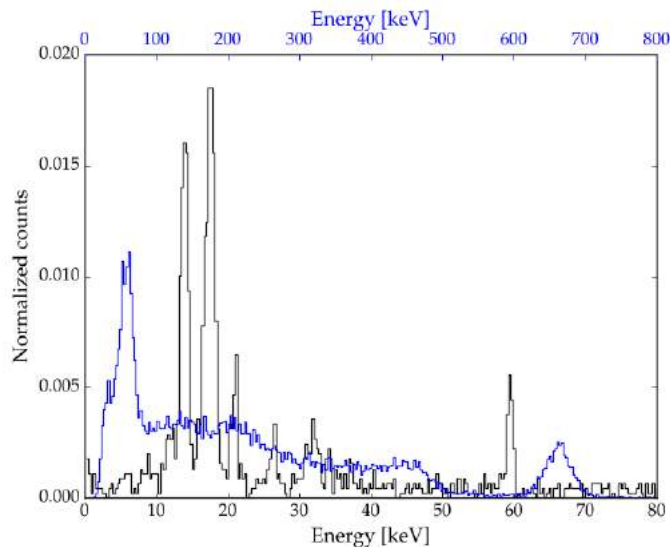
Figure 20: Simultaneous acquisition of a 137Cs plus a 241Am source by SDD. The black curve (lower x-axis) is the spectrum of 241Am photon detected by the SDD, while the blue one (upper x-axis) is the spectrum of 137Cs events detected in the CsI bar unit and readout by the top SDD through the generated scintillation photons.

(black line), while the higher-energy 137Cs spectrum is the results of the SDD readout of the scintillating photons generated inside the CsI(Tl) bar unit (blue line). Both types of events were acquired at the preamplifier output simultaneously by a fast digitizer (60 MS/s) and then distinguished with algorithms for pulse shape discrimination on the rising edge, and finally optimized digital filters were applied separately for the two categories of events.

The good performance of the digital signal processing methods are thus demonstrated, showing a comparable result with respect to a more traditional acquisition chain composed by an analogue shaping amplifier coupled to a commercial multichannel analyser. The setup shows a very good spectral resolution of 5% (FWHM) at 662 keV for scintillation events, and a ∼300 eV (rms) resolution at 6 keV for X-ray events at temperature of -30 ^{0}C.

5.4.2 Spatial resolution response of the CsI sensitive elements.

Each CsI(Tl) sensitive element has the lateral surfaces wrapped by a highly diffusive material able to provide an exponential decay with the distance of the scintillation cloud generation point along the of the major axis. This method was implemented for the first time in early 80's in the NaI detection plane ZEBRA balloon borne coded mask telescope [8] and in more recent years on the mini-calorimeter of the AGILE satellite payload [9]. The scintillation light that reach the SDD devices at the two extreme of the CsI(Tl) bar is then described by:

$$N_A = N_0 \; e^{-\alpha(L/2-x)}; \qquad\qquad N_B = N_0 \; e^{-\beta(L/2+x)}$$
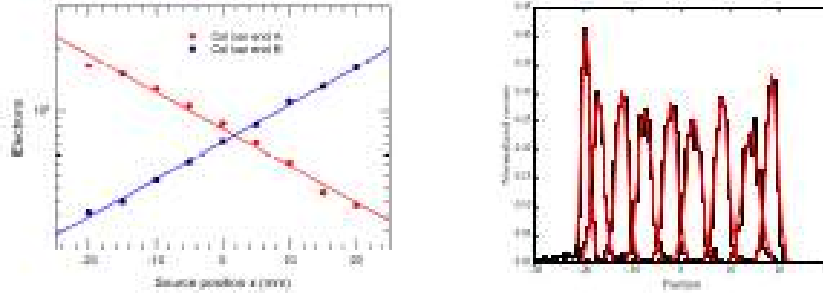
33

Figure 21: (a) Measurements of the signal readout by SDD device at the two CsI bar ends showing the linear attenuation of the signal logarithm with the source location along the bar major axis. The circle are the measured signal intensities in electrons, while the solid lines represents the linear best fits. (b) The reconstructed position along the CsI bar major axis. The resolution (FWHM) is 2 mm over 50 mm.

where N_0 is the number of the scintillation photons generated at the interaction point along the CsI(Tl) bar (x), N_A and N_B represent the number of the scintillation photons reaching the left and the right, respectively, end of each CsI(Tl) bar, L is the CsI(Tl) bar length. The parameter N0 depends on the energy deposited in the CsI(Tl) elements. Finally, α and β are the measured attenuation coefficients in the two opposite scintillation light travelling directions as the result of the CsI(Tl) diffusive wrapping. In the equation (1), the origin of the major axis is set at x=L/2. Using the knowledge of the attenuation coefficient and the signals collected at the two ends given by equation (1) is then possible to reconstruct the photon interaction position along the CsI(Tl) element major axis by means of the following relation:

$$\langle x \rangle = \frac{ln(N_B/N_A) - L/2(\beta - \alpha)}{\alpha + \beta} \qquad (9)$$

where x is the estimated position along the CsI bar major axis. Figure 7a gives an example of the signal amplitude readout by the SSD device at each end of a CsI(Tl) bar with a length of 50 mm using the 662 keV photons from a ^{137}Cs source. From these measurements, it is possible to evaluate for each CsI(Tl) sensitive elements the characteristic attenuation coefficient α and β. The solid lines are the linear best fits of the measured signals as function of the source position along the CsI(Tl) bar major axis. These best fits give for the scintillation light attenuation coefficients α and β the values (in mm^{-1}) of 0.0248 ± 0.0004 and 0.0245 ± 0.0010, respectively. Figure 7b show the reconstructed position of 662 keV photons from a collimated ^{137}Cs source. The average FWHM of the reconstructed position is 3 mm. Considering the source spot size in these measurements (2 mm), the derived intrinsic resolution in position for the gamma-ray interaction is around 2.2 mm (FWHM).

5.4.3   CsI response model for spectral resolution

The energy of each photons interacting inside the CsI(Tl) sensitive elements can be evaluated by the product of the signals readout by the SDD device at the
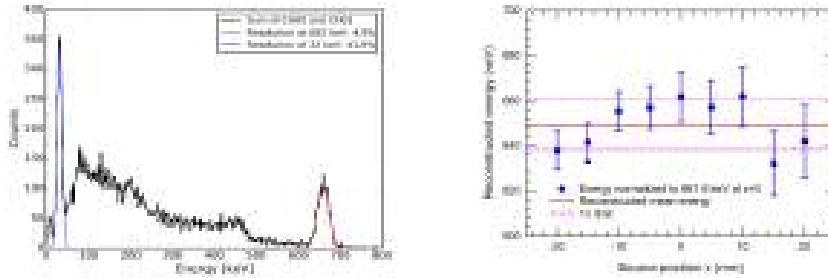
Figure 22: (a) A spectrum obtained with the ^{137}Cs source at the bar centre is shown. The measured resolution at 662 keV is 4.9%, with a lower threshold of 20 keV, thus confirming the expected results and the good performance of the overall system. (b) The normalized reconstructed energy along the major CsI bar axis obtained using the attenuation coefficient evaluated by data reported in Fig. 21 a. The short dashed pink lines give the $\pm 1\sigma$ spread.

two opposite ends. Using the expression in Eq. 5.4.2 for the two signals, we can easily derive the relation to calculate the energy deposited in a given position along the CsI(Tl) bar major axis:

$$E_\gamma = kN_0 = k\sqrt{N_A \ N_B} \ e^{L/4(\alpha+\beta)} \ e^{x/2(\alpha-\beta)} \tag{10}$$

Eq. 10 show that the reconstructed energy, corresponding to the same deposited energy, is not constant along the CsI(Tl) bar major axis. This dependence is the results of the non-symmetrical behaviour of the scintillation light attenuation across the CsI(Tl) element toward the two opposite ends: i.e. the attenuation coefficients α and β are slightly different. In fact, this demonstrates the importance of minimizing this difference by optimizing both the diffusion wrapping process on the individual CsI(Tl) elements and their optical coupling with the SDD reading devices. Figure 22 a shows the spectrum obtained with a collimated ^{137}Cs source at the bar centre. The measured resolution at 662 keV is 4.9% (FWHM), with a lower threshold of about 20 keV, thus confirming the expected results and the good performance of the system. Figure 22 b plots the reconstructed energy of the 662 keV peak of same radioactive source along the CsI(Tl) bar major axis. The two pink short dashed lines give the $\pm 1\sigma$ region, that is $\sim$20 keV wide. A results that is again compatible with the with the low energy threshold of the CsI(Tl)/SDD system.

5.4.4   WFM/S GEANT 4 Simulation Results

In order to evaluate the scientific performance of the ASTENA WFM/S in detecting and positioning GRB events, a Monte Carlo model has been developed using the Geant-4 framework to aid the feasibility study of the THESEUS XGIS detector. The mass model and the simulator are now being updated to fit the design foreseen for the ASTENA mission.

As an example of the results, the reconstructed spatial distribution of CsI(Tl) events obtained with a WFM/S module is shown in 23. In this particular case, the reconstructed events in each CsI(Tl) bar is discretized along the main axis in 10 segments 5 mm wide (i.e., twice the measured 1 σ spatial resolution).
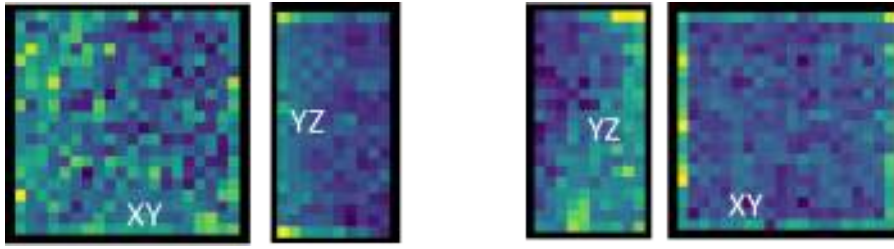
Figure 23: False colour maps of the counts detected by a CsI coded mask module illuminated by a parallel flux at 1 MeV with two different incoming directions, both external to Mask FOV: (a) $(\theta,\phi)=(40^0, 0^0)$ (b) $(\theta,\phi)=(70^0, 210^0)$, where θ is the zenithal angle and ϕ the azimuthal angle of the impinging flux.

Therefore, the coded mask module CsI(Tl) detector is equivalent to a 3D detector with voxels of 5 x 5 x 5 mm^3. This characteristic is particularly interesting, because it opens the possibility to use the detector also as a Compton detector, and in particular as a Compton scattering polarimeter. From the distribution of the detected counts and the capability to reconstruct the photon incoming direction by Compton cinematics over all WFM/S modules is possible to infer the GRB incoming direction within an angular precision that depends on its fluency, energetic and position.

5.5   Conclusions

A sensitive and broad-band X and gamma-ray instrument is needed to fulfill the ASTENA main scientific objectives that is to reliably identify and accurately positioning (at better than one arcmin) GRBs to allow fast high energy follow up measurement with the high sensitivity broadband Laue lens telescope (NFT). The proposed ASTENA WFM/S monitor design will allow also measuring high-energy transients on short timescales with contemporary good spectroscopic and polarimetric capabilities, allowing detailed investigation of the energetic and temporal evolution of these sources. Of course, several trade-offs and improvements on the basic design outlined in this paper can be foreseen. The field of view of a single unit, the coded mask open fraction (and its impact on efficiency and sensitivity), but also the choice of scintillator thickness, geometry and type (and its impact on efficiency and spectral resolution), besides the detailed triggering logic, should be optimized in a future assessment phase in order to maximize the ASTENA missions scientific returns.

From this report 2 proceedings SPIE have been presented at SPIE (Austin - Texas, June 2018) and 2 papers for Experimental Astronomy are being submitted.

References

[1] N. M Barrière, M. Ackermann, C. Wade, S. E. Boggs, L. Hanlon, J. Tomsick, and P. von Ballmoos. New prospects for Laue lenses made of self-focusing Si Laue Components (SiLCs). In *AAS/High Energy Astrophysics Division*, volume 14 of *AAS/High Energy Astrophysics Division*, page 116.04, August 2014.

[2] N. M. Barrière, L. Natalucci, N. Abrosimov, P. von Ballmoos, P. Bastie, P. Courtois, M. Jentschel, J. Knödlseder, J. Rousselle, and P. Ubertini, III. Soft gamma-ray optics: new Laue lens design and performance estimates. In *Society of Photo-Optical Instrumentation Engineers (SPIE) Conference Series*, volume 7437 of *Society of Photo-Optical Instrumentation Engineers (SPIE) Conference Series*, page 0, August 2009.

[3] V. Bellucci, R. Camattari, V. Guidi, I. Neri, and N. Barrière. Self-standing bent silicon crystals for very high efficiency Laue lens. *Experimental Astronomy*, 31:45–58, August 2011.

[4] C. Budtz-Jørgensen and I. Kuvvetli. New Position Algorithms for the 3-D CZT Drift Detector. *IEEE Transactions on Nuclear Science*, 64:1611–1618, June 2017.

[5] E. Buffagni, E. Bonnini, C. Ferrari, E. Virgilli, and F. Frontera. X-ray characterization of curved crystals for hard x-ray astronomy. In *Society of Photo-Optical Instrumentation Engineers (SPIE) Conference Series*, volume 9510 of *Society of Photo-Optical Instrumentation Engineers (SPIE) Conference Series*, page 6, May 2015.

[6] E. Buffagni, E. Bonnini, A. Zappettini, G. M. Guadalupi, F. Rossi, and C. Ferrari. Crystal bending by surface damaging in mosaic GaAs crystals for the LAUE project. In *Optics for EUV, X-Ray, and Gamma-Ray Astronomy VI*, volume 8861 of *SPIE proceeding*, page 88610E, September 2013.

[7] D. De Salvador, S. Carturan, A. Mazzolari, E. Bagli, L. Bandiera, C. Durighello, G. Germogli, V. Guidi, P. Klag, W. Lauth, G. Maggioni, M. Romagnoni, and A. Sytov. Innovative remotely-controlled bending device for thin silicon and germanium crystals. *Journal of Instrumentation*, 13:C04006, April 2018.

[8] C. Ferrari, E. Buffagni, L. Marchini, and A. Zappettini. High-resolution x-ray characterization of mosaic crystals for hard x-ray astronomy. *Optical Engineering*, 51(4):046502, April 2012.

[9] F. Frontera, E. Costa, D. dal Fiume, M. Feroci, L. Nicastro, M. Orlandini, E. Palazzi, and G. Zavattini. PDS experiment on board the BeppoSAX satellite: design and in-flight performance results. In O. H. Siegmund and M. A. Gummin, editors, *EUV, X-Ray, and Gamma-Ray Instrumentation for Astronomy VIII*, volume 3114 of *Society of Photo-Optical Instrumentation Engineers (SPIE) Conference Series*, pages 206–215, October 1997.

[10] F. Frontera, G. Loffredo, A. Pisa, L. Milani, F. Nobili, N. Auricchio, V. Carassiti, F. Evangelisti, L. Landi, S. Squerzanti, K. H. Andersen, P. Courtois, L. Amati, E. Caroli, G. Landini, S. Silvestri, J. B. Stephen, J. M. Poulsen, B. Negri, and G. Pareschi. Development status of a Laue lens project for gamma-ray astronomy. In *Proceedings of the SPIE*, volume 6688, September 2007.

[11] F. Frontera, E. Virgilli, V. Valsan, V. Liccardo, V. Carassiti, E. Caroli, F. Cassese, C. Ferrari, V. Guidi, S. Mottini, M. Pecora, B. Negri, L. Recanatesi, L. Amati, N. Auricchio, L. Bassani, R. Campana, R. Farinelli, C. Guidorzi, C. Labanti, R. Landi, A. Malizia, M. Orlandini, P. Rosati, V. Sguera, J. Stephen, and L. Titarchuk. Scientific prospects in soft gamma-ray astronomy enabled by the LAUE project. In *Proceedings of the SPIE*, volume 8861, id. 886106 17 pp., 2013.

[12] M. Galloway, A. Zoglauer, S. E. Boggs, and M. Amman. A combined Compton and coded-aperture telescope for medium-energy gamma-ray astrophysics. *Astronomy and Astrophysics*, 614:A93, June 2018.

[13] H. Halloin, P. von Ballmoos, J. Evrard, G. K. Skinner, J. M. Alvarez, M. Hernanz, N. Abrosimov, P. Bastie, B. Hamelin, P. Jean, J. Knödlseder, R. K. Smither, and G. Vedrenne. Gamma-Ray Astronomy Starts to see CLAIRE: First Light for a Crystal Diffraction Telescope. In V. Schoenfelder, G. Lichti, and C. Winkler, editors, *5th INTEGRAL Workshop on the INTEGRAL Universe*, volume 552 of *ESA Special Publication*, page 739, October 2004.

[14] F. A. Harrison, W. W. Craig, F. E. Christensen, C. J. Hailey, W. W. Zhang, and et al. The Nuclear Spectroscopic Telescope Array (NuSTAR) high-energy X-ray mission. *The Astrophysical Journal*, 2013.

[15] M. Khalil, F. Frontera, E. Caroli, E. Virgilli, and V. Valsan. A simulation study on the focal plane detector of the LAUE project. *Nuclear Instruments and Methods in Physics Research A*, 786:59–70, June 2015.

[16] I. Kuvvetli, C. Budtz-Jørgensen, A. Zappettini, N. Zambelli, G. Benassi, E. Kalemci, E. Caroli, J. B. Stephen, and N. Auricchio. A 3D CZT high resolution detector for x- and gamma-ray astronomy. In *High Energy, Optical, and Infrared Detectors for Astronomy VI*, volume 9154, page 91540X, July 2014.

[17] N. Lund. An "ESA-Affordable" Laue-lens. *Experimental Astronomy*, 20:211–217, December 2005.

[18] K. Nandra. Athena: Exploring the Hot and Energetic Universe. In *AAS/High Energy Astrophysics Division #14*, volume 14 of *AAS/High Energy Astrophysics Division*, page 301.01, August 2014.

[19] K. Nandra, D. Barret, X. Barcons, A. Fabian, J.-W. den Herder, L. Piro, M. Watson, C. Adami, J. Aird, J. M. Afonso, and et al. The Hot and Energetic Universe: A White Paper presenting the science theme motivating the Athena+ mission. *ArXiv e-prints*, June 2013.

[20] L. Piro, L. Natalucci, and Ahead Consortium. AHEAD: Integrated Activities in the High Energy Astrophysics Domain. In M. Ehle, editor, *Exploring the Hot and Energetic Universe: The first scientific conference dedicated to the Athena X-ray observatory*, page 74, September 2015.

[21] R. K. Smither, K. A. Saleem, D. E. Roa, M. A. Beno, P. von Ballmoos, and G. K. Skinner. High diffraction efficiency, broadband, diffraction crystals for use in crystal diffraction lenses. *Experimental Astronomy*, 20:201–210, December 2005.

[22] P. Ubertini, F. Lebrun, G. Di Cocco, A. Bazzano, A. J. Bird, K. Broenstad, A. Goldwurm, G. La Rosa, C. Labanti, P. Laurent, I. F. Mirabel, E. M. Quadrini, B. Ramsey, V. Reglero, L. Sabau, B. Sacco, R. Staubert, L. Vigroux, M. C. Weisskopf, and A. A. Zdziarski. IBIS: The Imager on-board INTEGRAL. *AA*, 411:L131–L139, November 2003.

[23] E. Virgilli, F. Frontera, V. Valsan, V. Liccardo, V. Carassiti, F. Evangelisti, and S. Squerzanti. Laue lenses for hard x-/soft γ-rays: new prototype results. In *Proceedings of the SPIE*, volume 8147, id. 81471B 9 pp., 2011.

[24] E. Virgilli, F. Frontera, V. Valsan, V. Liccardo, V. Carassiti, S. Squerzanti, M. Statera, M. Parise, S. Chiozzi, F. Evangelisti, E. Caroli, J. Stephen, N. Auricchio, S. Silvestri, A. Basili, F. Cassese, L. Recanatesi, V. Guidi, V. Bellucci, R. Camattari, C. Ferrari, A. Zappettini, E. Buffagni, E. Bonnini, M. Pecora, S. Mottini, and B. Negri. The LAUE project and its main results. In *Proceedings of the SPIE*, volume 8861, id. 886106 17 pp., 2013.

[25] E. Virgilli, V. Valsan, F. Frontera, E. Caroli, V. Liccardo, and J. B. Stephen. Expected performances of a Laue lens made with bent crystals. *ArXiv e-prints*, November 2017.

[26] P. von Ballmoos, H. Halloin, J. Evrard, G. Skinner, N. Abrosimov, J. Alvarez, P. Bastie, B. Hamelin, M. Hernanz, P. Jean, J. Knödlseder, and B. Smither. CLAIRE: First light for a gamma-ray lens. *Experimental Astronomy*, 20:253–267, December 2005.

[27] W. H. Zachariasen. *Theory of X-ray Diffraction in Crystals*. Wiley, 1945.

[28] A. Zoglauer, R. Andritschke, S. E. Boggs, F. Schopper, G. Weidenspointner, and C. B. Wunderer. MEGAlib: simulation and data analysis for low-to-medium-energy gamma-ray telescopes. In *Space Telescopes and Instrumentation 2008: Ultraviolet to Gamma Ray*, volume 7011 of *222*, page 70113F, July 2008.